



# New strategies in metal oxide nanowire based gas sensors

Feng Shao

**ADVERTIMENT.** La consulta d'aquesta tesi queda condicionada a l'acceptació de les següents condicions d'ús: La difusió d'aquesta tesi per mitjà del servei TDX ([www.tdx.cat](http://www.tdx.cat)) i a través del Dipòsit Digital de la UB ([diposit.ub.edu](http://diposit.ub.edu)) ha estat autoritzada pels titulars dels drets de propietat intel·lectual únicament per a usos privats emmarcats en activitats d'investigació i docència. No s'autoritza la seva reproducció amb finalitats de lucre ni la seva difusió i posada a disposició des d'un lloc aliè al servei TDX ni al Dipòsit Digital de la UB. No s'autoritza la presentació del seu contingut en una finestra o marc aliè a TDX o al Dipòsit Digital de la UB (framing). Aquesta reserva de drets afecta tant al resum de presentació de la tesi com als seus continguts. En la utilització o cita de parts de la tesi és obligat indicar el nom de la persona autora.

**ADVERTENCIA.** La consulta de esta tesis queda condicionada a la aceptación de las siguientes condiciones de uso: La difusión de esta tesis por medio del servicio TDR ([www.tdx.cat](http://www.tdx.cat)) y a través del Repositorio Digital de la UB ([diposit.ub.edu](http://diposit.ub.edu)) ha sido autorizada por los titulares de los derechos de propiedad intelectual únicamente para usos privados enmarcados en actividades de investigación y docencia. No se autoriza su reproducción con finalidades de lucro ni su difusión y puesta a disposición desde un sitio ajeno al servicio TDR o al Repositorio Digital de la UB. No se autoriza la presentación de su contenido en una ventana o marco ajeno a TDR o al Repositorio Digital de la UB (framing). Esta reserva de derechos afecta tanto al resumen de presentación de la tesis como a sus contenidos. En la utilización o cita de partes de la tesis es obligado indicar el nombre de la persona autora.

**WARNING.** On having consulted this thesis you're accepting the following use conditions: Spreading this thesis by the TDX ([www.tdx.cat](http://www.tdx.cat)) service and by the UB Digital Repository ([diposit.ub.edu](http://diposit.ub.edu)) has been authorized by the titular of the intellectual property rights only for private uses placed in investigation and teaching activities. Reproduction with lucrative aims is not authorized nor its spreading and availability from a site foreign to the TDX service or to the UB Digital Repository. Introducing its content in a window or frame foreign to the TDX service or to the UB Digital Repository is not authorized (framing). Those rights affect to the presentation summary of the thesis as well as to its contents. In the using or citation of parts of the thesis it's obliged to indicate the name of the author.

# **New strategies in metal oxide nanowire based gas sensors**

Feng Shao

Programa de Doctorat en Enginyeria i Tecnologies Avançades

# **New strategies in metal oxide nanowire based gas sensors**

Tesi que presenta Feng Shao  
per optar al títol de Doctor per la Universitat de Barcelona

Directors de la tesi:

**Dr. Francisco Hernández Ramírez**

Responsable del Servei de Gestió de la Recerca,  
Institut de Recerca en Energia de Catalunya (IREC)  
Investigador, Institut de Recerca en Energia de Catalunya (IREC)  
Professor Associat, Universitat de Barcelona

**Dr. Núria López**

Institut Català d'Investigació Química (ICIQ)

Tutor:

**Dr. Albert Cornet Calveras**

Professor, Universitat de Barcelona

Barcelona, Novembre 2013

Departament d'Electrònica



Àrea de Materials Avançats per a l'Energia





# Acknowledgements

First and the greatest gratitude should be given to my supervisors Dr. Francisco Hernández Ramírez and Dr. Nuria Lopez, for your marvelous guidance and teaching in these years and saving me from troubles.

It would be impossible without you. I am very grateful for the IREC PhD fellowship and Prof. Joan Ramon Morante for having me in the research group, supplying brain storming ideas and monitoring the main outcome of this work.

Special thanks should go to my ex-supervisor Dr. Joan Daniel Prades and those senior lab mates: Dr. Teresa Andreu, Dr. Cristian Fàbrega and Dr. Román Jiménez Díaz, thank you for helping me in the lab, the details are always most important.

I owe big thanks to the people of the S3 consortium, especially Irina Giebelhaus who prepared the nanowires at Prof. Sanjay Mathur's group in cologne. Reza Zamini for making the microscope characterization. Dr. Martin W. G. Hoffmann and Dr. Alaa Eldin Gad for bringing the interesting topics. And Dr. Angelika Hackner on the surface ionization devices.

I would like to thank Martin Gumbau Gonzalez from ICIQ and Yolanda Atienza Garcia of the scientific park of Barcelona for helping me with the super computer and FIB system, respectively. And Prof. Andreu Cabot for accessing into his lab.

Also I would like to express my appreciation to the staff of IREC's management team who helped in many ways.

And finally, the friends in the lab, Fan, WenHua, Marta, Andrés, Marcel, ZhiShan, HaiBin, Cristina, Erdem and many others. It's great to have you there.

To those who I know during the past four years but not mentioned here — Gracias a todos.

*To my parents*

至我的父母



## Resum en català

Després de dècades de recerca, els sensors resistius basats en òxids metàl·lics (MOX) actualment representen una alternativa tecnològica capaç de detectar gasos amb alta sensibilitat, i amb una mida reduïda i baix cost. Permeten controlar de forma senzilla baixes concentracions de gasos procedents de combustibles fòssils i altres contaminants d'interès a la indústria. No obstant, encara hi ha limitacions pràctiques pel que fa a la seva selectivitat, sensibilitat, estabilitat i consum energètic a causa de la naturalesa intrínseca del procés de detecció de les molècules tèrmicament activat que hi té lloc a la seva superfície.

Amb l'objectiu últim de millorar els sensors MOXs, aquesta tesi doctoral se n'ocupa de diferents aspectes que van des de la preparació dels dispositius, la seva caracterització estructural, la modelització de la seva resposta sota diferents condicions experimentals així com la implementació d'estratègies per a millorar-los a curt, mig i llarg termini. Aquest treball ha permès doncs comprendre els mecanismes de detecció que hi tenen lloc a la seva superfície dels MOXs així com aconseguir sensors millorats basats en nanofils individuals i amb d'altres morfologies complexes.

Fent servir el sistema  $\text{SnO}_2\text{-NH}_3$ , els càlculs teòrics amb DFT (Density Functional Theory) han permès analitzar i parametritzar les interaccions d'un gas típic amb la superfície d'un òxid metàl·lic tipus n de referència en el camp dels sensors. El model teòric resultant ha estat validat experimentalment a posteriori amb èxit. Per altra banda, s'ha explorat la utilització de nous òxids metàl·lics per a la detecció de gasos com el CuO, un material tipus p, i heterostructures formades per nanofils d'òxid de coure decorats per partícules d'òxid d'estany ( $\text{CuO@SnO}_2$ ). Finalment, la integració d'òxids metàl·lics amb forma nanoestructurada (nanofils) en "micro hotplates" ( $\mu\text{HP}$ )

ha permès obtenir sensors que treballen en un mode tèrmic polsat, fet que té avantatges clares: augment de l'estabilitat i sensitivitat. El procés de fabricació d'aquests dispositius s'ha completat de forma satisfactòria fent servir tècniques de “self-assembly” (dielectroforesi, DEF).

Aquest treball de tesi s'estructura de la forma següent:

**Capítol 1.** Introducció als sensors de gasos basats en òxids metàl·lics. Es repassa de forma breu l'estat actual d'aquesta tecnologia, els mètodes de preparació dels dispositius, els mecanismes de detecció així com la utilització de nanomaterials per millorar els sensors tradicionals basats en capes semiconductores. A més a més, es fa una introducció a la química computacional.

**Capítol 2.** Aquesta segona part se centra en els fonaments de la teoria que hi ha darrera de les simulacions i càlculs DFT (Density Functional Theory). Es revisen en detall els teoremes així com les eines metodològiques que ens permeten resoldre l'equació de Schrödinger de sistemes complexos i modelitzar el seu comportament experimental. A més, s'hi presenta una cerca de la literatura existent sobre la utilització de DFT en la modelització dels mecanismes de detecció de gasos amb òxids metàl·lics.

**Capítol 3.** En aquesta part s'hi descriuen tant les eines teòriques com pràctiques que s'han fet servir en per desenvolupar la tesi doctoral: (i) la preparació i síntesi de nanomaterials, (ii) la metodologia per accedir elèctricament a nanofils individuals mitjançant, (iii) les tècniques d'auto assemblatge per alinear molts nanofils en un únic dispositiu, (iv) la metodologia emprada per mesurar la resposta a gasos i (v) els càlculs teòrics realitzats amb el paquet de simulació *ab-initio* (VASP).

**Capítol 4.** En aquest capítol, els mecanismes de sensat d'amoníac i aigua fent servir nanofils de SnO<sub>2</sub> són estudiats fent servir una aproximació que combina resultats experimentals i teòrics. La

utilització de nanofil·ls monocristal·lins amb superfícies ben definides ha permès comparar els càlculs DFT amb respostes reals de forma directa i inequívoca. L'estudi ha validat que la reacció de l'amoniac sobre SnO<sub>2</sub> s'explica per la pèrdua progressiva d'hidrògens de la molècula i amb la consegüent formació d'aigua i nitrogen gasos com a principals productes de la reacció associada. Aquest procés queda regulat des d'un punt de vista energètic per la presència d'oxigen adsorbit a la superfície, O<sub>ads</sub> i és intrínsecament competitiu amb l'adsorció de l'aigua a l'òxid metàl·lic. La metodologia de treball que s'ha fet servir i que combina dades experimentals i simulacions teòriques és potencialment extensible a altres casos d'interès.

**Capítol 5.** Aquí es fa un anàlisi dels mecanismes de detecció del sulfur d'hidrogen en nanofil·ls d'òxid d'estany decorats amb nanopartícules d'òxid de coure fent servir dispositius reals fabricats amb nanolitografia FIB. Aquestes heteroestructures exhibeixen una molt més alta sensibilitat a aquest gas que no pas els nanofil·ls simples, fet que es deriva de la particularitat del procés de detecció que hi té lloc; la modulació de la unió p-n entre el CuO i SnO<sub>2</sub> en presència o no d'aquest gas així com els canvis en l'amplada del canal de conducció dins el nanofil·l d'òxid d'estany. Tot plegat, els resultats que s'hi presenten són un exemple interessant de com la utilització de heteroestructures basades en nanomaterials han de permetre a curt i mig termini una millora dels dispositius que fins ara només integraven nanofil·ls simples.

**Capítol 6.** En aquest capítol s'explora la possibilitat de fer servir nanofil·ls de CuO per a detectar gasos d'interès (NH<sub>3</sub>, H<sub>2</sub>S, NO<sub>2</sub>). El treball experimental demostra una bona potencialitat d'aquest semiconductor tipus p especialment en el cas de l'amoniac, on s'aconsegueixen respostes millors que les obtingudes amb nanofil·ls d'òxid d'estany. D'aquest treball particular se'n conclou que l'oxigen adsorbit a la superfície de l'òxid esdevé clau per poder modelitzar la

resposta dels sensors. No obstant, cal remarcar que els resultats són preliminars i no permeten anar més enllà en l'avaluació de l'òxid de coure com un potencial substituït de l'òxid d'estany.

**Capítol 7.** Aquí es presenta l'ús de dielectroforesi (DEP) per dipositar de forma controlada nanofils a la superfície de  $\mu$ HPs. Els sensors resultants, fabricats d'una forma molt més senzilla que l'alternativa FIB utilitzada en capítols anteriors, han estat avaluats en la detecció de  $\text{NH}_3$  i CO. Fent servir el mode d'operació conegut com polsat de temperatura, on aquest paràmetre és modula a freqüències elevades, s'ha pogut millorar la sensibilitat d'aquests dispositius. Aquest fet és el resultat de l'alteració de la reactivitat de la superfície a causa de les sobtades transicions de temperatura.

**Capítol 8.** En aquest capítol es resumeix tots els resultats anteriors i s'identifiquen noves línies de treball de cara a futurs treballs doctorals.

# Abstract

This dissertation presents the results of applying new strategies to understand the sensing mechanism of metal oxide (MOX) nanowire based gas sensors, and explores their final performance. To that end, density functional theory (DFT) calculations were used; new materials were integrated in novel devices; and sensors working on temperature-pulsed operation mode were tested. Here, the studied MOX nanowires ranged from SnO<sub>2</sub> nanowires, SnO<sub>2</sub> nanowires decorated with CuO particles and bare CuO or ZnO nanowires, either in bundles or isolated form.

Firstly, using SnO<sub>2</sub>-NH<sub>3</sub> as a model system, DFT calculations were made to draw the picture of a surface-gas interaction of interest for the industry. Combining the theoretical results with experimental tests in individual nanowires allowed determining the sensing mechanism of ammonia by tin oxide. In short, the surface reaction routine involves non lattice oxygens and it is responsible for the response. As a typical interfering substance to NH<sub>3</sub> sensing, H<sub>2</sub>O was also taken into account in this study. Secondly, SnO<sub>2</sub> nanowires decorated by CuO nanoparticles (CuO@SnO<sub>2</sub>) showed enhanced sensitivity to H<sub>2</sub>S with high selectivity towards other gases, e.g., CO and NH<sub>3</sub>. *Ex-situ* analysis showed that sulfurization and desulfurization reactions happen on CuO nanoparticles and as a result the charge transport in the nanowires changes by modification of the depletion layer in the MOX surface. This result was an example of how complex heterostructures can be used to improve MOX sensors. Thirdly, a p-type MOX, CuO, was evaluated as a gas sensor. NH<sub>3</sub>, H<sub>2</sub>S and NO<sub>2</sub> responses showed a key role of surface adsorbed oxygen species in the final performance of these devices. The use of p-type MOX paves the way to new devices. Finally, ZnO nanowires were assembled onto micro hot plate ( $\mu$ HP) substrates

by dielectrophoretic (DEP) alignment. The resulting devices exhibited good response to  $\text{NH}_3$ . When operated in temperature-pulsed mode, the sensitivity to this gas was observed to increase. The modulation of the response was ascribed to the fast regulation of oxygen and other surface species in this mode.

Overall, this dissertation explores new strategies and materials to improve our control and knowledge of the gas sensing mechanisms in MOX with the final objective of developing better devices in the future.

# Table of Contents

Acknowledgements.....	v
Resum en català .....	viii
Abstract.....	xii
Table of Contents.....	I
1. Introduction .....	1
1.1 MOX gas sensors .....	1
1.2 Gas sensing mechanisms in MOX gas sensors .....	4
1.3 MOX nanomaterials as the sensing material.....	7
1.4 Computational chemistry .....	10
1.5 Scope of this work.....	10
References .....	13
2. Introduction to density functional theory .....	17
2.1 The fundamentals of DFT .....	18
2.2 Use of DFT for modeling MOX gas sensor.....	26
References .....	29
3. Methods .....	31
3.1 Preparation of nanowires.....	31
3.2 Fabrication of electrical contacts to nanowires .....	32

3.2.1	Individual nanowires.....	32
3.2.2	Dielectrophoretic assembly of ZnO nanowires onto $\mu$ HP substrates .....	34
3.3	Electrical measurements and gas sensing.....	36
3.4	DFT calculations .....	38
	References .....	41
4.	NH <sub>3</sub> sensing with SnO <sub>2</sub> nanowire and the influence of H <sub>2</sub> O.....	43
4.1	Introduction .....	43
4.1.1	SnO <sub>2</sub> as the NH <sub>3</sub> sensor.....	43
4.1.2	Standard formulation of NH <sub>3</sub> sensing with n-type MOX .....	47
4.1.3	Surface interaction of O <sub>2</sub> and NH <sub>3</sub> on SnO <sub>2</sub> (110).....	49
4.2	NH <sub>3</sub> sensing using individual SnO <sub>2</sub> nanowires .....	51
4.2.1	NH <sub>3</sub> sensing in dry SA .....	51
4.2.2	Response to NH <sub>3</sub> in humidified SA .....	57
4.3	DFT modeling of NH <sub>3</sub> interaction with SnO <sub>2</sub> (110) surface .....	59
4.3.1	Adsorption of NH <sub>3</sub> on stoichiometric and reduced surface .....	59
4.3.2	NH <sub>3</sub> dissociation and H <sub>2</sub> O formation with the bridging O <sub>2c</sub> .....	61
4.3.3	NH <sub>3</sub> dissociation and H <sub>2</sub> O formation with the pre-adsorbed O <sub>ads</sub> .....	64
4.3.4	H <sub>2</sub> O adsorption and its influence on NH <sub>3</sub> sensing.....	68
4.4	Conclusions .....	70
	References .....	71



5.	H <sub>2</sub> S sensing with SnO <sub>2</sub> nanowires and CuO@SnO <sub>2</sub> nanoheterostructure.....	76
5.1	Introduction .....	76
5.2	Materials.....	78
5.3	Results and discussions .....	78
5.3.1	H <sub>2</sub> S sensing with bare SnO <sub>2</sub> nanowire.....	78
5.3.2	H <sub>2</sub> S sensing with CuO decorated SnO <sub>2</sub> nanowires .....	80
5.3.3	Qualitatively modeling of H <sub>2</sub> S sensing mechanisms by CuO decorated SnO <sub>2</sub> and SnO <sub>2</sub> nanowires .....	82
5.4	Conclusions .....	86
	References .....	87
6.	Preparation and characterization of individual CuO nanowire sensors for gas sensing.....	89
6.1	Introduction .....	89
6.2	Results and discussion.....	90
6.2.1	Morphology and crystalline structure .....	90
6.2.2	Electrical measurements .....	94
6.2.3	Gas sensing and discussion.....	95
6.3	Conclusions .....	102
	References .....	103
7.	ZnO nanowire sensors based on micro hot plates and the NH <sub>3</sub> response in temperature-pulsed mode .....	106

7.1	Introduction .....	106
7.2	Results and discussion.....	108
7.2.1	Self-assembly of nanowires onto $\mu$ HPs .....	108
7.2.2	Gas sensing response of ZnO $\mu$ HP sensors.....	112
7.3	Conclusions .....	120
	References .....	122
8.	Conclusions and future work.....	126
8.1	Conclusions .....	126
8.2	Future work .....	128
	Short CV .....	130

# 1. Introduction

A sensor is a device that detects physical stimuli and converts them into measurable signals. In the particular case of gas sensors, these stimuli are derived from the gas molecules' interactions with the device, and the output signal mainly depends on the type of sensor used, e.g., resistive, electrochemical, etc. [1].

Typical applications of gas sensors are i) monitoring of toxic and flammable gas leakage in industry and civilian establishments; ii) control of combustion efficiency and exhaust gases in automobiles [2, 3]. Moreover, new applications are continuously developed; for instance in the medical field, monitoring a patients' respiratory system requires CO<sub>2</sub> and O<sub>2</sub> sensors [4]. Beyond the current state-of-the-art of gas sensor applications, an unexplored future [5, 6] has been drawn by scientists with potential applications in intelligent buildings, clean energy vehicles and as part of advanced wireless sensor networks. According to a recent market research [7], the global gas sensor market is expected to reach a value of 2.32 billion USD by 2018.

## 1.1 MOX gas sensors

Gas sensing can be realized by different working principles. Besides resistive type MOX gas sensor, which make up the core part of this dissertation, there are also other types of sensors such as electrochemical, infrared and photo-ionization ones. Previous works in the literature [1, 8] are available for extended reading.

Resistive MOX gas sensors were first commercialized by N. Taguchi in 1968 [9, 10], but the idea of using semiconductors to detect gases was explored in 1952 when Germanium was found to offer such possibility in the Bell Laboratory [11]. After several decades of evolution, resistive MOX gas sensors feature high sensitivity, compact size and low cost [12], and are considered one of the best options for monitoring low concentrations of combustion gases [13]. For the sake of simplicity, they will be termed as MOX gas sensors in the rest of the dissertation.

MOX gas sensors are generally fabricated by depositing a layer of MOX, typically SnO<sub>2</sub> or In<sub>2</sub>O<sub>3</sub>, onto a substrate with electrodes and an integrated heater. Two common methods to deposit this layer are screen printing and sputtering. By screen printing, the paste of MOX particles (or materials in other shapes) is printed onto the substrate through a mesh. After an annealing, the deposited film appears as a layer of interconnected MOX materials with thickness between several micro meters and adjustable porosity. On the other hand, a more precise control over the deposited layer can be achieved by sputtering (e.g., thickness of only several tens of nanometers but in compact form). When combined with standard microelectronic processing technology, the sensing layer can also be made into sub-micron size in the lateral direction to allow the further minimization of the sensor [14]. Depicted in figure.1.1 are three typical layouts of MOX gas sensors; Sketch (a) corresponds to the conventional Taguchi gas sensors, having the heater (metal wire) passing through a ceramic tube with the sensing material painted on its surface. The MOX is connected to two Au electrodes allowing the measurement of the resistance changes. Sketch (b) represents a planar ceramic sensor with typical size from mm to cm. They have inter-digital electrodes and on their top the sensing layer is deposited. For heating, a heater (usually Pt) is also integrated in the structure. Finally, sketch (c) is the so-called micro hotplate-based gas sensor with big advantages in terms of size reduction and power consumption. The

fabrication relies on the use of standard microelectronic processing. More details are provided in Chapter 7. The typical enclosures for MOX gas sensors, at least at lab level, are metal can

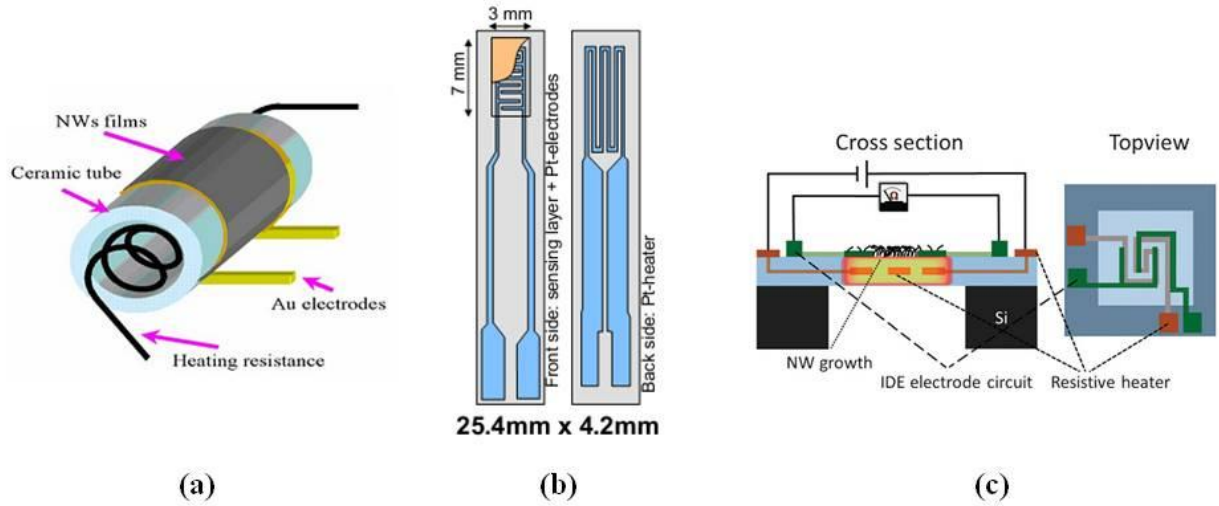


**Figure 1.1** Schematics showing different metal oxide gas sensor designs. (a) Taguchi gas sensor [15]. (b) Planar ceramic gas sensor [16] and (c)  $\mu$ HP sensor [17].

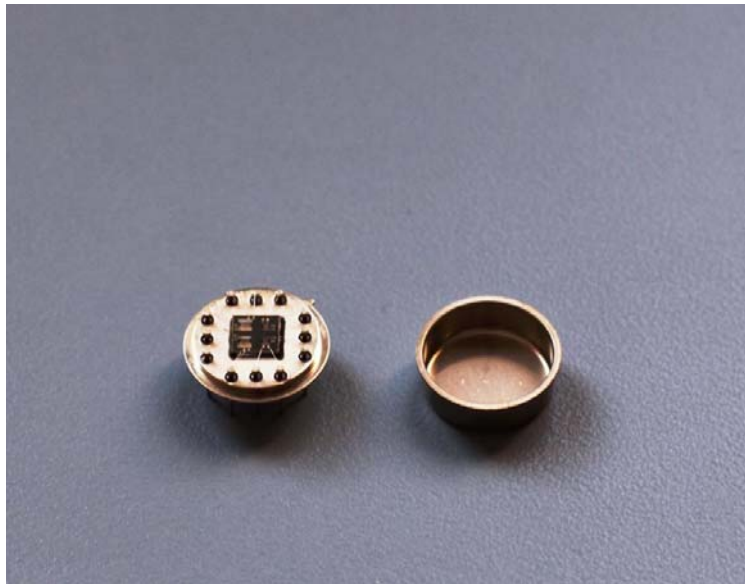


**Figure 1.2**  $\mu$ HP sensor integrated into a TO package.

transistor outlines (TOs) as that one shown in figure 1.2. In these structures, electrical connections to the sensors are made by welding for the Taguchi gas sensors or standard wire bonding for the other two types. Access to the ambient air happens through the metal mesh lid, which also protect the sensing layer from dust.

## **1.2 Gas sensing mechanisms in MOX gas sensors**

The working principle of MOX gas sensors is generally described as the interaction of the target gas with both the material surface and the pre-adsorbed oxygen species. On the one hand, the resistance of n-type MOXs typically increases when oxidizing gases adsorb at the surface. This generates a surface depletion region (figure 1.3) by extracting electrons from the semiconductor. On the contrary, reducing gases consume adsorbed oxygen species and release electrons back to the MOX. As a result, this diminishes the resistance. The abovementioned mechanisms are thermally activated (figure 1.4a). This is the main reason why the maximum response of MOX sensors is usually found at intermediate temperatures (between 100°C and 350°C) [14].

Despite this simplified description of the sensing mechanism in MOX, the reality is far more complex [13]. The gas sensing phenomena is the result of a series of chemical and physical processes involving the gas molecules, the surface and the bulk of the MOX. Thus, the study of the sensing mechanisms focuses on two complementary directions: unveiling details of the surface chemical reactions and later modeling the surface/bulk charge transport processes.

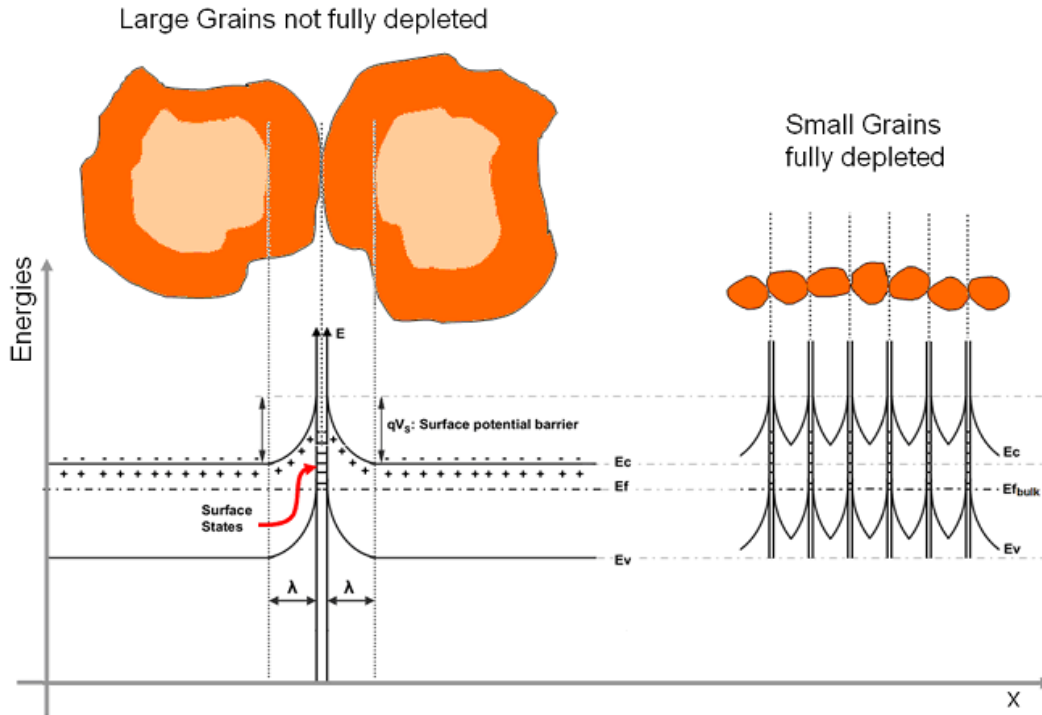


**Figure 1.3** Band diagrams showing depletion regions in MOX nanoparticles [18]. (Left) For large particles the electronic properties in the inner volume of the particle are unaffected and the electrical conduction is fully affected by the grain boundary effects. (Right) The depletion layer in small particles is larger than their size, inducing a full depletion of the particle and affecting the whole volume. For a detail review of the conduction mechanisms in MOX nanoparticles as function of the dimensions, see [18].

Adsorption of gas molecules on solid surfaces can be classified into physisorption or chemisorption [19]. The former is induced by weak van der Waals forces and can be transferred (with subsequent bond activation) into the latter one, which involves a chemical bonding with the atoms at the surface. Adsorbed molecules can undergo a dissociation process to form smaller molecular or atomic fragments on the surface. As a result, the system evolves to a state for lowering the total energy.

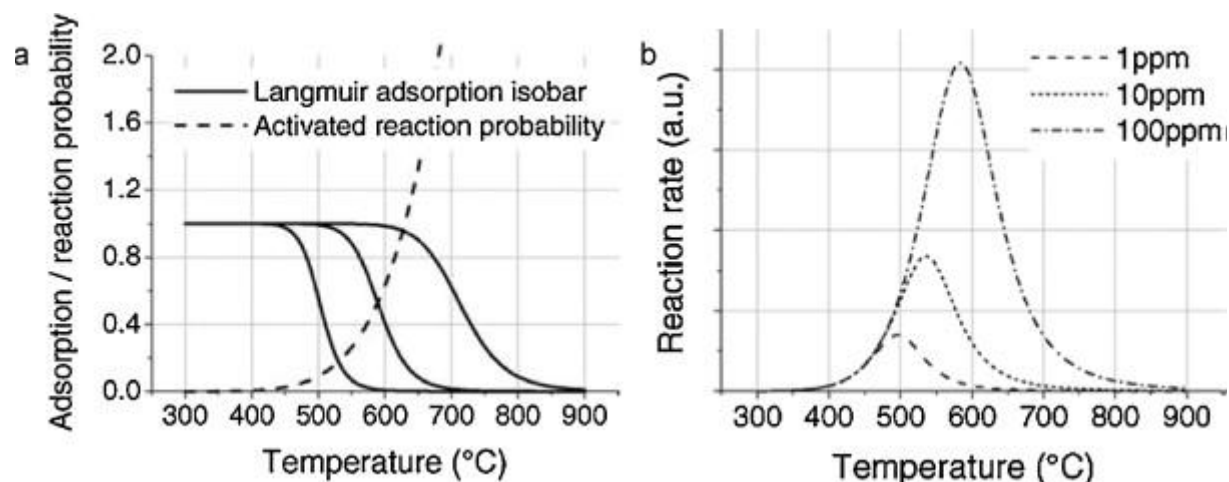
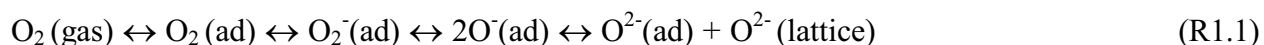


**Figure 1.4** (a) Adsorption (solid line) and reaction (dashed line) probability of gas molecules at the MOX surface (higher gas pressures make the adsorption line to shift to higher temperature values). (b) Typical bell-shaped sensitivity vs. temperature relation of a MOX gas sensor as induced by the adsorption and reaction probabilities (here the reaction rate is proportional to sensitivity) [14].

Analytical techniques like X-ray Photon emission Spectroscopy (XPS), Temperature Programmed Desorption (TPD), Fourier Transform Infrared Spectroscopy (FTIR) are the common tools to evaluate the interactions of gas molecules at the solid surface. For instance, Electron Spin Resonance (ESR) and TPD measurements [20] have been extremely valuable to describe oxygen adsorption onto  $\text{SnO}_2$  and the formation of anion species with increasing temperature according the processes below,



TPD studies have also shown that these adsorbed oxygen species are crucial to describe the reactivity of other gases, e.g., CO [20].



Nevertheless, having a clear picture of how the gas molecules interact with the MOX surface is not enough to quantitatively explain the change of electrical properties in the solids. Resistance, the most important parameter in the MOX gas sensors, is determined by the materials' intrinsic electrical properties, morphology, temperature, gas environment, etc. For a typical gas sensor made of compact thin film or granular porous thick film, the theory of bulk electrical conductivity does not apply and the morphology becomes a decisive factor. That is because the depletion of charge carriers at the solid surface causes complicate scenario for the determination of resistance. Therefore, the performance of MOXs as gas sensors is a complex issue that has attracted many efforts in the last years [14, 21].

### **1.3 MOX nanomaterials as the sensing material**

MOX gas sensors have been utilized for low-cost detection of combustible and toxic gases for decades but unsolved issues with sensitivity, selectivity and stability remain as the weak points that prevent this technology from a wider use. Moreover, the high power consumption necessary to activate the thermally activated sensing process has limited their use in large scale wireless sensor networks [6].

Recent advances in nanotechnology provided the opportunity to improve the performance of MOX gas sensors [22]. The large surface to bulk ratio of nanomaterials is considered an advantage to obtain higher responses to those obtained with their micro counterparts [23, 24]. Therefore, gas sensors based on one dimensional (1D) nanostructures such as nanowires [25], nanotubes [26] and nanorods [27] have been deeply studied in the last years.

There are two main approaches to obtain nanomaterials: top down and bottom up. By the top down one, they are obtained by removing materials from solids in a controlled way, while the bottom up approach constructs the nanomaterial from atomic or molecular precursors. Example of the top down approach is the fabrication of large scale integrated circuits on Si. There are also chemical top down methods [28], e.g., metal assisted etching of Si wafer into Si nanowires [29] and anodic oxidation of Ti foil to produce TiO<sub>2</sub> nanotubes [30]. Because of many limitations with the top down approach, majority of 1D MOX nanostructures are fabricated by several bottom up techniques. According to the physical environment applied, these methods can be divided into two groups: growth from vapor phase or from liquid phase. Chemical Vapor Deposition (CVD) [31] and vapor transport growth [32] are two typical vapor phase methods. Whereas template-assisted deposition [33] and hydrothermal synthesis [34] are typical liquid based methods. Complementary reviews of the different synthesis methodologies and their fundamentals can be found in refs.[35-37].

1D nanostructure can be integrated in gas sensor in bundles or at individual level (figure 1.5). It is relative easier to prepare device with bundles of 1D nanostructures lying in between two electrodes for gas sensing. For instance, this can be done by printing the nanowire paste onto the electrodes [38] or reverse the sequence, depositing the metal electrodes on top of nanowires [39]. Alternatively, electrospinning is another attractive technique to deposit the nanofibers directly onto the electrodes [40]. Moreover, methods have been developed to grow nanowires directly on the sensing substrates [17, 32, 41, 42].

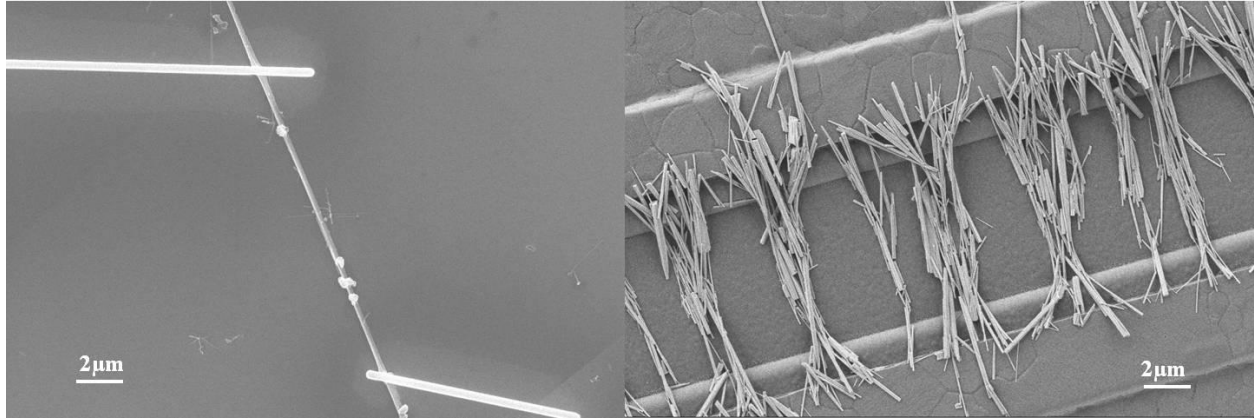


**Figure 1.4** (a) Individual nanowire contacted by FIB lithography. (b) Bundles of nanowires lying between electrodes.

On the other hand, the preparation of individual 1D nanostructure devices demands a more advanced control of nanostructures at the nanoscale. As a result, complex fabrication technologies become necessary. Electron beam lithography [43] and focused ion/electron beam (FIB/EB) deposition [44] are two common examples of these technologies. E-beam lithography replaces the light source of traditional photo lithography [45] by electrons to pattern the resists and achieve the subsequent metal deposition with nanoscale precision [46]. FIB/EB dual beam systems use an ion beam or electron beam to induce the decomposition of metal organic precursors to achieve the localized deposition of metals in a predefined shape. Although being widely used for scientific purposes, afore mentioned methods both suffer from the major setbacks of high cost and low throughput. To solve this major drawback, attempts have been made to generate electrical contacts to individual nanowires by manipulating them with Dielectrophoresis (DEP) [47], which demonstrated a higher yield following a simpler process.

## 1.4 Computational chemistry

Theoretical chemistry aims to describe chemical processes by using mathematical formalisms [48]. The Schrödinger equation provides the mathematical formulation that can be employed to describe the ground state of a given system and by extension the description of all the chemical processes. Different ways to solve the Schrödinger equation, in particular Density Functional Theory (DFT) have provided a robust computational tool that can be efficiently implemented into the computer as a program to solve chemical problems [49].

Computational chemistry is extremely valuable for understanding or predicting the physical properties and interaction behavior of molecules and solids. The information that can be acquired from the calculation includes the atomic structure, electronic properties, solid-gas interacting details, etc., being complementary to experimental approaches. Therefore, computational chemistry combined with the experiments generates useful synergies in understanding the physics of materials as we will see in this dissertation.

## 1.5 Scope of this work

This dissertation puts together the efforts to understand the gas sensing mechanisms of MOX nanowire gas sensors. With this purpose, real gas sensing tests using individual nanowires were confronted to theoretical calculations. *Ex-situ* characterization and empirical modeling were performed. Based on that, novel device structure was explored to enhance the sensing performance.

The current dissertation is organized as follows:

**Chapter 1** introduces the general background of MOX gas sensors and the basic idea of computational chemistry.

**Chapter 2** gives a brief introduction to the fundamentals of density functional theory.

**Chapter 3** describes the experimental and theoretical procedures used to perform this work.

**Chapter 4** deals with the NH<sub>3</sub>/H<sub>2</sub>O sensing mechanisms using SnO<sub>2</sub> nanowires. Experimental results and DFT calculations were put together to get a general view of the sensing phenomena involving these two gases and the n-type MOX of reference. DFT calculations depicted the interactions between NH<sub>3</sub>-SnO<sub>2</sub> and H<sub>2</sub>O-SnO<sub>2</sub>, which unveiled the interfering mechanism of H<sub>2</sub>O in real experiments.

**Chapter 5** focuses on the H<sub>2</sub>S sensing response using SnO<sub>2</sub> nanowires decorated with CuO nanoparticles (heterostructure). By *ex-situ* analysis and empirical modeling, the significantly enhanced H<sub>2</sub>S sensitivity was found to be resulting from the p-n junction change induced by the sulphurisation of CuO by H<sub>2</sub>S.

**Chapter 6** explores the NH<sub>3</sub>, H<sub>2</sub>S and NO<sub>2</sub> sensing properties of individual CuO nanowires. The study revealed the promising alternative for gas sensing of a p-type semiconductor with fully comparable performance of those obtained with SnO<sub>2</sub>.

**Chapter 7** presents a self-assembly technique (DEP alignment) to deposit MOX nanowires onto the  $\mu$ HP sensing substrate. Moreover, NH<sub>3</sub> sensing using ZnO nanowires operated in temperature-pulsed mode allowed to improve the response of the sensors. Here, the reasons behind this behavior are presented and discussed.

**Chapter 8** summarizes this dissertation, highlights the main achievements and envisages new research lines for future works.

## References

- [1] S.K. Pandey, K.-H. Kim, K.-T. Tang, A Review of Sensor-Based Methods for Monitoring Hydrogen Sulfide, *TrAC, Trends Anal. Chem.*, 32 (2012) 87–99.
- [2] N. Docquier, S. Candel, Combustion control and sensors: a review, *Progress in Energy and Combustion Science*, 28 (2002) 107-150.
- [3] R. Moos, A Brief Overview on Automotive Exhaust Gas Sensors Based on Electroceramics, *Int. J. Appl. Ceram. Technol.*, 2 (2005) 401- 413.
- [4] M. Folke, L. Cernerud, M. Ekstrom, B. Hok, Critical review of non-invasive respiratory monitoring in medical care, *Med. Bio. Eng. Comput.*, 41 (2003) 377-383.
- [5] *Solid State Gas Sensors - Industrial Application*, M. Fleischer, M. Lehmann (Eds.), Springer, Berlin Heidelberg, 2012.
- [6] R.A. Potyrailo, C. Surman, N. Nagraj, A. Burns, Materials and Transducers Toward Selective Wireless Gas Sensing, *Chemical Reviews*, 111 (2011) 7315-7354.
- [7] *TransparencyMarketResearch, Gas Sensors Market - Global Industry Size, Share, Trends, Analysis And Forecast, 2012 -2018, 2013.*
- [8] J. Chou, *Hazardous Gas Monitors - A Practical Guide to Selection, Operation and Applications*, McGraw-Hill and SciTech Publishing, 1999.
- [9] N. Taguchi, GAS DETECTING ELEMENT AND METHOD OF MAKING IT, in: U.S. Patent (Ed.), 3 644 795, 1970.
- [10] N. Taguchi, in: J. Patent (Ed.), 45-38200, 1962.
- [11] W.H. Brattain, J. Bardeen, Surface properties of germanium, *Bell. Syst. Tech. J.*, 32 (1952) 1.
- [12] I. Simon, N. Bârsan, M. Bauer, U. Weimar, Micromachined metal oxide gas sensors: opportunities to improve sensor performance, *Sensors and Actuators B: Chemical*, 73 (2001) 1-26.
- [13] N. Yamazoe, Toward innovations of gas sensor technology, *Sensors and Actuators B: Chemical*, 108 (2005) 2-14.
- [14] S. Ahlers, G. Müller, T. Doll, A rate equation approach to the gas sensitivity of thin film metal oxide materials, *Sensors and Actuators B: Chemical*, 107 (2005) 587-599.
- [15] J. Huang, Q. Wan, Gas Sensors Based on Semiconducting Metal Oxide One-dimensional Nanostructures, *Sensors*, 9 (2009) 9903–9924.

- [16] R. Moos, K. Sahner, M. Fleischer, U. Guth, N. Barsan, U. Weimar, Solid State Gas Sensor Research in Germany – a Status Report, *sensors*, 9 (2009) 4323-4365.
- [17] S. Barth, R. Jimenez-Diaz, J. Sama, J. Daniel Prades, I. Gracia, J. Santander, C. Cane, A. Romano-Rodriguez, Localized growth and in situ integration of nanowires for device applications, *Chemical Communications*, 48 (2012) 4734-4736.
- [18] R.J. Díaz, Fabrication Technology and Characterisation of Advanced Single nanowire-based Metal Oxide Gas Sensors on Microhotplates, in: *Departament d'Electrònica, Universitat de Barcelona*, 2012.
- [19] H. Lüth, *Solid Surfaces, Interfaces and Thin Films*, Springer, 2010.
- [20] M. Batzill, U. Diebold, The Surface and Materials Science of Tin Oxide, *Prog. Surf. Sci.*, 79 (2005) 47-154.
- [21] N. Barsan, U. Weimar, Conduction Model of Metal Oxide Gas Sensors, *J. Electroceram.*, 7 (2001) 143-167.
- [22] N. Yamazoe, New approaches for improving semiconductor gas sensors, *Sensors and Actuators B: Chemical*, 5 (1991) 7-19.
- [23] S.G. Ansari, P. Boroojerdian, S.R. Sainkar, R.N. Karekar, R.C. Aiyer, S.K. Kulkarni, Grain size effects on H<sub>2</sub> gas sensitivity of thick film resistor using SnO<sub>2</sub> nanoparticles, *Thin Solid Films*, 295 (1997) 271-276.
- [24] G. Korotcenkov, The role of morphology and crystallographic structure of metal oxides in response of conductometric-type gas sensors, *Materials Science and Engineering: R: Reports*, 61 (2008) 1-39.
- [25] Q. Kuang, C. Lao, Z.L. Wang, Z. Xie, L. Zheng, High-sensitivity humidity sensor based on a single SnO<sub>2</sub> nanowire, *J. Am. Chem. Soc.*, 129 (2007) 6070-6071.
- [26] J. Kong, N.R. Franklin, C. Zhou, M.G. Chapline, S. Peng, K. Cho, H. Dai, Nanotube Molecular Wires as Chemical Sensors, *Science*, 287 (2000) 622-625.
- [27] C.C. Li, Z.F. Du, L.M. Li, H.C. Yu, Q. Wan, T.H. Wang, Surface-depletion controlled gas sensing of ZnO nanorods grown at room temperature, *Applied Physics Letters*, 91 (2007) 032101-032103.
- [28] H.-D. Yu, M.D. Regulacio, E. Ye, M.-Y. Han, Chemical routes to top-down nanofabrication, *Chemical Society Reviews*, (2013).
- [29] Z. Huang, N. Geyer, P. Werner, J. de Boor, U. Gösele, Metal-Assisted Chemical Etching of Silicon: A Review, *Advanced Materials*, 23 (2011) 285-308.
- [30] F. Cristian, H.-R. Francisco, P. Joan Daniel, J.-D. Román, A. Teresa, M. Joan Ramon, On the photoconduction properties of low resistivity TiO<sub>2</sub> nanotubes, *Nanotechnology*, 21 (2010) 445703.
- [31] S. Mathur, S. Barth, H. Shen, J.-C. Pyun, U. Werner, Size-dependent Photoconductance in SnO<sub>2</sub> Nanowires, *small*, 1 (2005) 713-717.



- [32] L. Lei, D.S. Brian, L. Liwei, Local vapor transport synthesis of zinc oxide nanowires for ultraviolet-enhanced gas sensing, *Nanotechnology*, 21 (2010) 495502.
- [33] X. Li, Y. Wang, Y. Lei, Z. Gu, Highly sensitive H<sub>2</sub>S sensor based on template-synthesized CuO nanowires, *RSC Advances*, 2 (2012) 2302-2307.
- [34] J. Fan, Y. Hao, A. Cabot, E.M.J. Johansson, G. Boschloo, A. Hagfeldt, Cobalt(II/III) Redox Electrolyte in ZnO Nanowire-Based Dye-Sensitized Solar Cells, *ACS Applied Materials & Interfaces*, 5 (2013) 1902-1906.
- [35] M. Law, J. Goldberger, P. Yang, Semiconductor nanowires and nanotubes, *Annu. Rev. Mater. Res.*, 34 (2004) 83- 122.
- [36] S. Barth, F. Hernandez-Ramirez, J.D. Holmes, A. Romano-Rodriguez, Synthesis and applications of one-dimensional semiconductors, *Prog. Mater. Sci.*, 55 (2010) 563–627.
- [37] E. Comini, C. Baratto, G. Faglia, M. Ferroni, A. Vomiero, G. Sberveglieri, Quasi-one Dimensional Metal Oxide Semiconductors: Preparation, Characterization and Application as Chemical Sensors, *Prog. Mater. Sci.*, 54 (2009) 1–7.
- [38] J. Kim, K. Yong, Mechanism Study of ZnO Nanorod-Bundle Sensors for H<sub>2</sub>S Gas Sensing, *J. Phys. Chem. C*, 115 (2011) 7218-7224.
- [39] Y.C. Lee, H. Huang, O.K. Tan, M.S. Tse, Semiconductor gas sensor based on Pd-doped SnO<sub>2</sub> nanorod thin films, *Sensors and Actuators B: Chemical*, 132 (2008) 239-242.
- [40] Y. Zhao, X. He, J. Li, X. Gao, J. Jia, Porous CuO/SnO<sub>2</sub> composite nanofibers fabricated by electrospinning and their H<sub>2</sub>S sensing properties, *Sensors and Actuators B: Chemical*, 165 (2012) 82-87.
- [41] S. Semancik, R.E. Cavicchi, M.C. Wheeler, J.E. Tiffany, G.E. Poirier, R.M. Walton, J.S. Suehle, B. Panchapakesan, D.L. DeVoe, Microhotplate platforms for chemical sensor research, *Sensors and Actuators B: Chemical*, 77 (2001) 579-591.
- [42] S. Sumita, Z.A. Syed, K.G. Prasanta, Z. Guofang, R. John, A.C. James, I.M. William, W.G. Julian, U. Florin, Post-CMOS wafer level growth of carbon nanotubes for low-cost microsensors—a proof of concept, *Nanotechnology*, 21 (2010) 485301.
- [43] A.N. Broers, W.W. Molzen, J.J. Cuomo, N.D. Wittels, Electron-beam fabrication of 80Å metal structures, *Applied Physics Letters*, 29 (1976) 596-598.
- [44] R. Steve, P. Robert, A review of focused ion beam applications in microsystem technology, *Journal of Micromechanics and Microengineering*, 11 (2001) 287.
- [45] A. Pimpin, W. Srituravanich, Review on Micro- and Nanolithography Techniques and Their Applications, 2011.
- [46] J. Goldberger, D.J. Sirbully, M. Law, P. Yang, ZnO Nanowire Transistors, *The Journal of Physical Chemistry B*, 109 (2004) 9-14.

[47] E.M. Freer, O. Grachev, X. Duan, S. Martin, D.P. Stumbo, High-yield self-limiting single-nanowire assembly with dielectrophoresis, *Nat Nano*, 5 (2010) 525-530.

[48] D.C. Young, *Computational Chemistry: A Practical Guide for Applying Techniques to Real-World Problems*, John Wiley & Sons, 2001.

[49] M.C. Payne, M.P. Teter, D.C. Allan, T.A. Arias, J.D. Joannopoulos, Iterative minimization techniques for *ab initio* total-energy calculations: molecular dynamics and conjugate gradients, *Reviews of Modern Physics*, 64 (1992) 1045-1097.

## 2. Introduction to density functional theory

Quantum mechanics is the theoretical background necessary to describe the behavior of electrons [1]. In principle, it can be used to model the properties of individual atoms, molecules or bulky materials. But in practice, the Schrödinger equations can only be solved exactly for one electron systems (e.g., H atom). Therefore, simplifications and approximations have to be made if more complex systems are studied [2].

Unlike the well-known wave-function based Hartree-Fock method [3], Density Functional Theory (DFT) turns the Schrödinger equation of  $4N$  variables (three spatial and one spin with  $N$  the number of electrons) into the problem of solving equations of the density functional, which has 3 variables. This significantly reduces the cost of scaling up the calculation with a good trade-off in terms of the results accuracy.

DFT has become a powerful tool in chemistry, physics, material science and other disciplines. The implementation of the method into different computer codes has further eased the prerequisites of running calculations. Nowadays, DFT is no more limited to a small group of theoretical scientists but is available for a large collective with different backgrounds [2]. However, the correct use of DFT can be only achieved with a good comprehension of the fundamentals of the system to be studied.

In this chapter, a brief introduction is given about the basics of DFT. Besides, to know what has been done with it to deal with the problems of MOX gas sensing, a survey of related literature has been made.

## 2.1 The fundamentals of DFT

### *The Schrödinger equation*

Matter at microscopic scale, e.g., atom, electron, is governed by quantum mechanics, whose core is the Schrödinger equation. The form of this equation depends on the physical system to be described. The general time-independent Schrödinger equation usually appears as

$$\hat{H}\Psi = E\Psi \quad (2.1)$$

Where  $\hat{H}$  is the Hamiltonian operator, a differential operator representing the total energy of the system,  $\Psi$  is the wave function of the quantum system and  $E$  is the energy of the state. The solution to the Schrödinger equation is called the wave function. Theoretically, the wave function gives a complete description of any system of interest.

The complete time-independent Schrödinger equation for  $n$  electrons and  $N$  ions can be written in terms of the electronic coordinates  $r_1, \dots, r_n$  and the ionic coordinates  $R_1, \dots, R_N$  as [4]

$$\left[ -\sum_{i=1}^n \frac{\hbar^2}{2m} \nabla_i^2 - \sum_{k=1}^N \frac{\hbar^2}{2M_k} \nabla_k^2 + \frac{1}{2} \sum_{i,j=1}^n \frac{e^2}{r_{ij}} + V_{ii}(\mathbf{R}_1, \dots, \mathbf{R}_N) + V_{ei}(\mathbf{r}_1, \dots, \mathbf{r}_n; \mathbf{R}_1, \dots, \mathbf{R}_N) \right] \Psi = E\Psi \quad (2.2)$$

Where  $\nabla^2$  is the Laplace operator, i.e.,  $\frac{\partial^2}{\partial x^2} + \frac{\partial^2}{\partial y^2} + \frac{\partial^2}{\partial z^2}$ ,  $r_{ij}$  is the distance between electrons  $i$  and  $j$  while  $i \neq j$ .

The first term on the left hand side corresponds to the kinetic energy of the electrons, the second one is the kinetic energy of the ions, the third one is the electron-electron interaction potential,

the fourth one is the ion-ion interaction potential and the last is the electron-ion interaction potential.

The Schrödinger equation, however, can only be solved for the hydrogen atom, or a system made up with a particle inside a “box”. For more complex systems, approximations are needed.

### ***Born-Oppenheimer approximation***

The electron mass  $m$  is much smaller than ion mass  $M_k$ , and the electron motion is also much faster [4]. Therefore, the Born-Oppenheimer approximation assumes that ions remain fixed while electrons move. Thus, the second term of equation (2.2), the kinetic energy of ions, can be discarded while the electrostatic repulsion between the ions keeps constant. The above equation of electrons and ions can thus be simplified into equation of electrons:

$$\left[ -\sum_{i=1}^n \frac{\hbar^2}{2m} \nabla_i^2 + \frac{1}{2} \sum_{i,j=1}^n \frac{e^2}{r_{ij}} + V_{ei}(\mathbf{r}_1, \dots, \mathbf{r}_n; \mathbf{R}_1, \dots, \mathbf{R}_N) \right] \psi(\mathbf{r}_1, \dots, \mathbf{r}_n; \mathbf{R}_1, \dots, \mathbf{R}_N) = E_e(\mathbf{R}_1, \dots, \mathbf{R}_N) \psi(\mathbf{r}_1, \dots, \mathbf{r}_n; \mathbf{R}_1, \dots, \mathbf{R}_N) \quad (2.3)$$

Where  $\psi(\mathbf{r}_1, \dots, \mathbf{r}_n; \mathbf{R}_1, \dots, \mathbf{R}_N)$  is the electronic wave function,  $E_e(\mathbf{R}_1, \dots, \mathbf{R}_N)$  is the electron energy,  $\mathbf{R}_1, \dots, \mathbf{R}_N$  are fixed ionic coordinates,  $\nabla^2$  is the Laplace operator, and the Hamiltonian operator in the equation is abbreviated as  $\hat{H}_e = \hat{T} + \hat{V}_{ee} + \hat{V}_{ext}$ , where  $\hat{T}$  is the kinetic energy of the electrons,  $\hat{V}_{ee}$  is the electron-electron interaction potential and  $\hat{V}_{ext}$  is the electron-ion interaction potential  $V_{ei}(\mathbf{r}_1, \dots, \mathbf{r}_n; \mathbf{R}_1, \dots, \mathbf{R}_N)$ .

Even with the Born-Oppenheimer approximation, solving equation (2.3) remains a formidable task since the difficulty of solving the Schrödinger equation rapidly increases with the number of electrons.

## ***Hohenberg-Kohn theorems***

DFT formalism rests on two fundamental theorems formulated by Kohn and Hohenberg and the derivation of a set of equations developed by Kohn and Sham in the mid 1960s [3].

The first Hohenberg-Kohn theorem states that “*the external potential  $\hat{V}_{ext}$ , and hence the ground-state total energy, is a unique functional of the electron density  $\rho(\mathbf{r})$* ”. A functional is defined as a function of another function, in this case, the electron density. The theorem can thus be represented by the ground state electron density  $\rho_0$ :

$$E_0[\rho_0] = T[\rho_0] + E_{ee}[\rho_0] + E_{ei}[\rho_0] \quad (2.4)$$

Where  $E_0$  is the complete ground state energy,  $T$  is the kinetic energy,  $E_{ee}$  is the electron-electron interaction energy and  $E_{ei}$  is the electron-ion interaction energy.

The summation of the first two energy functions in equation (2.4) is defined as Hohenberg-Kohn functional  $F_{HK}[\rho_0]$ , which represents the major challenge in DFT as the explicit expressions for  $T[\rho]$  and the non-classic parts of  $E_{ee}[\rho]$  is unknown.

The second Hohenberg-Kohn theorem states that “ *$F_{HK}[\rho]$ , the functional that delivers the ground state energy of the system, delivers the lowest energy if and only if the input density is the true ground state density  $\rho_0$* ”:

$$E_0 \leq E_0[\tilde{\rho}] = T[\tilde{\rho}] + E_{ee}[\tilde{\rho}] + E_{ei}[\tilde{\rho}] \quad (2.5)$$

Where  $\tilde{\rho}$  is a trial density  $\tilde{\rho}(\mathbf{r})$ . As the result, the problem of finding the ground state energy with respect to the wave function of  $4N$  variables ( $N$  is the number of electrons) in traditional computational chemistry is replaced by finding a density  $\tilde{\rho}(\mathbf{r})$  that only depends on the three

space dimensions. Moreover,  $\tilde{\rho}(\mathbf{r})$  corresponds to a physical observable magnitude that can be directly compared to experimental data.

### *The Kohn-Sham approach*

Working with the Hohenberg-Kohn theorems requires further simplifications, and a practical approach was introduced by Kohn and Sham. The  $N$  interacting electrons system is replaced by a fictitious non-interacting  $N$  electron system, where electrons move in the so-called effective Kohn-Sham single particle potential  $V_S(\mathbf{r})$ . The main statement used to establish this approach is that for any interacting system, there exists a local single particle potential  $V_S(\mathbf{r})$  such that the exact ground state density of the interacting system  $\rho_0(\mathbf{r})$  equals the ground state density of the non-interacting system  $\rho_S(\mathbf{r})$ , i.e.,

$$\rho_0(\mathbf{r}) = \rho_S(\mathbf{r}) = \sum_{i=1}^N |\varphi_i(\mathbf{r})|^2 \quad (2.6)$$

In this system, the exact wave functions of non-interacting fermions are given by Slater determinants:

$$\Psi_{\text{KS}} = \frac{1}{\sqrt{N!}} \det[\varphi_1(\mathbf{r}_1) \varphi_2(\mathbf{r}_2) \dots \varphi_N(\mathbf{r}_N)] \quad (2.7)$$

Where the spin orbitals  $\varphi_i$  are determined by

$$\hat{f}^{\text{KS}} \varphi_i = \varepsilon_i \varphi_i \quad (2.8)$$

With the one-electron operator defined as  $\hat{f}^{\text{KS}} = -\frac{1}{2} \nabla^2 + V_S(\mathbf{r})$ ,

And for this type of wave functions, the kinetic energy is expressed as

$$T_S = -\frac{1}{2} \sum_i^N \langle \varphi_i | \nabla^2 | \varphi_i \rangle \quad (2.9)$$

Knowing  $T_S$ , the Hohenberg-Kohn functional  $F_{HK}[\rho]$  is rewritten into

$$F[\rho(\mathbf{r})] = T_S[\rho(\mathbf{r})] + J[\rho(\mathbf{r})] + E_{XC}[\rho(\mathbf{r})] \quad (2.10)$$

In which  $J[\rho(\mathbf{r})]$  represents the classical Coulomb energy of electron-electron interaction.  $E_{XC}[\rho(\mathbf{r})]$  is the so-called exchange-correlation energy, which can be expressed as  $E_{XC}[\rho] = (T[\rho] - T_S[\rho]) + (E_{ee}[\rho] - J[\rho])$ . We see that  $E_{XC}[\rho]$  is actually the summation of two parts: the difference between the kinetic energy of non-interacting electrons and the true kinetic energy of the interacting electrons, plus the non-classical electrostatic contributions. Indeed,  $E_{XC}[\rho]$  is the functional that contains the unknown elements of the system and it is generally estimated.

Finally, the local single particle potential  $V_S(\mathbf{r}_1)$  that produces orbitals  $\{\varphi_i\}$ , that minimize the system energy is given as

$$\begin{aligned} V_S(\mathbf{r}_1) &= V_{eff}(\mathbf{r}_1) = V_H(\mathbf{r}_1) + V_{XC}(\mathbf{r}_1) + V_{ext}(\mathbf{r}_1) \\ &= \int \frac{\rho(\mathbf{r}_2)}{r_{12}} d\mathbf{r}_2 + V_{XC}(\mathbf{r}_1) - \sum_A^M \frac{Z_A}{r_{1A}} \end{aligned} \quad (2.11)$$

The derivation of this equation can be found in ref.[3].  $V_H(\mathbf{r})$  is the Hartree potential,  $V_{XC} = \frac{\delta E_{XC}}{\delta \rho}$  is the potential due to the  $E_{XC}$  and  $V_{ext}$  is the external potential acting on the interacting system.

Using the above correlated expressions, the Kohn-Sham equations can be iteratively solved and the total energy of the interacting system can be obtained (as given by equation (2.12)). In figure 2.1, a flow chart of the iteration process is given.

$$E[\rho] = T_S[\rho] + J[\rho] + E_{XC}[\rho] + E_{ei}[\rho] =$$



$$-\frac{1}{2}\sum_i^N \langle \varphi_i | \nabla^2 | \varphi_i \rangle + \frac{1}{2}\sum_i^N \sum_j^N \iint |\varphi_i(\mathbf{r}_1)|^2 \frac{1}{r_{12}} |\varphi_j(\mathbf{r}_2)|^2 d\mathbf{r}_1 d\mathbf{r}_2 + E_{xc}[\rho(\mathbf{r})] - \sum_i^N \int \sum_A^M \frac{Z_A}{r_{1A}} |\varphi_i(\mathbf{r}_1)|^2 d\mathbf{r}_1 \quad (2.12)$$

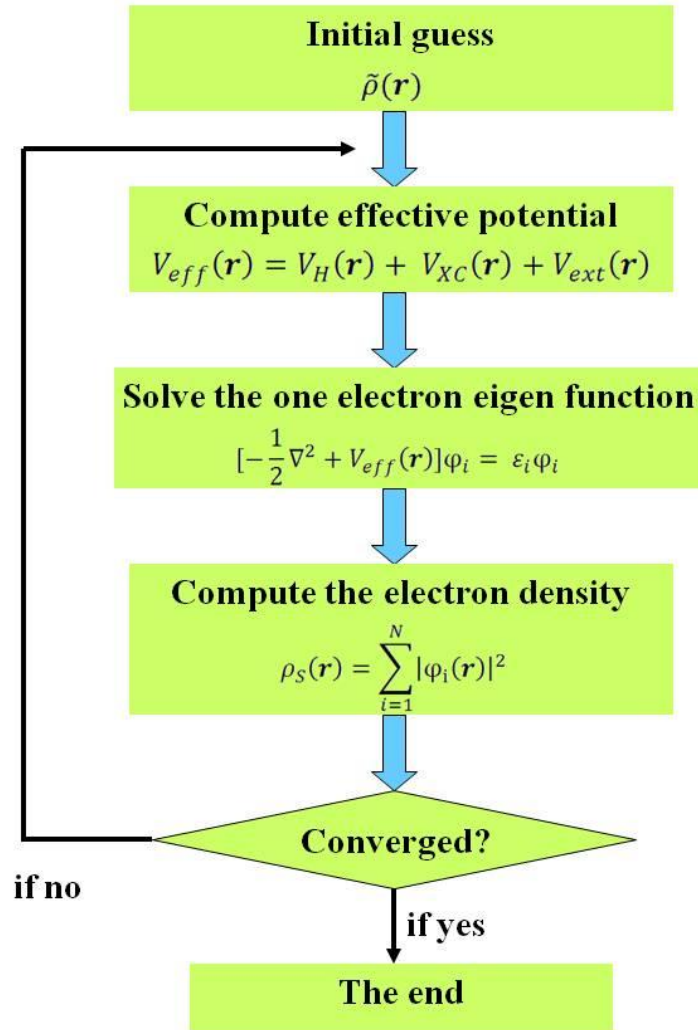


**Figure 2.1** Schematic representation of the iteration process to solve the Kohn-Sham equation.

### *Exchange-Correlation (XC) functionals*

The Kohn-Sham approach would have produced an exact solution of the Schrödinger equation if the explicit form of the exchange-correlation energy,  $E_{XC}$ , and the corresponding potential,  $V_{XC}$ , were known. Unfortunately, this is not the case. Indeed, the central goal of modern DFT is to find better approximations to these two functional forms.

Uniform electron gas is the only system for which the form of the exchange and correlation energy functional is known. In this system, electrons move on a positive background and the total charge of the system remains neutral. Physically, such a system resembles the model of an idealized metal consisting of a perfect crystal of valence electrons and positive cores where the cores are smeared out. The local density approximation (LDA) based on this model approximates the XC functional as a simple function of the electron density at any position  $\mathbf{r}$ . The value of this function is the exchange-correlation energy per electron in a uniform homogeneous gas of density  $\rho(\mathbf{r})$ :

$$E_{XC}^{LDA}[\rho] = \int \rho(\mathbf{r}) \varepsilon_{XC}(\rho(\mathbf{r})) d\mathbf{r} \quad (2.13)$$

Here  $\varepsilon_{XC}(\rho(\mathbf{r}))$  is the exchange-correlation energy per particle of a uniform electron gas of density  $\rho(\mathbf{r})$ . The energy per particle is weighted with the probability  $\rho(\mathbf{r})$ .

$\varepsilon_{XC}(\rho(\mathbf{r}))$  can be further split into an exchange and a correlation contribution:

$$\varepsilon_{XC}(\rho(\mathbf{r})) = \varepsilon_X(\rho(\mathbf{r})) + \varepsilon_C(\rho(\mathbf{r})) = -\frac{3}{4} \sqrt{\frac{3\rho(\mathbf{r})}{\pi}} + \varepsilon_C(\rho(\mathbf{r})) \quad (2.14)$$

Where  $\varepsilon_X(\rho(\mathbf{r}))$  represents the exchange energy of an electron in a uniform electron gas of a particular density. For the correlation part  $\varepsilon_C(\rho(\mathbf{r}))$ , it is generally given by analytical methods as no such explicit expression is known.

The LDA show moderate accuracy in term of the obtained results which is usually sufficient for solid state physics but not for chemistry studies [3].

On the other hand, the Generalized Gradient Approximation (GGA) functionals which take into account the gradients of the charge density and hole constraints offer the higher accuracy. GGA functionals can be written as

$$E_{XC}^{GGA}[\rho_\alpha, \rho_\beta] = \int f(\rho_\alpha, \rho_\beta, \nabla\rho_\alpha, \nabla\rho_\beta) d\mathbf{r} \quad (2.15)$$

Where  $\rho_\alpha, \rho_\beta$  are two separated spin densities,  $\nabla$  is the differential operator and  $\nabla\rho$  is the gradient of density.  $E_{XC}^{GGA}[\rho_\alpha, \rho_\beta]$  is also composed by two parts, the exchange and correlation contributions, i.e.,

$$E_{XC}^{GGA}[\rho_\alpha, \rho_\beta] = E_X^{GGA} + E_C^{GGA} \quad (2.16)$$

Several different GGA functionals have been developed. They generally offer improved accuracy for calculating properties such as bond dissociation. The one used in the work in Chapter 4 is the revised Perdew-Burke-Ernzerhof (RPBE) functional from Nørskov et al.[5]. Its description to molecule and atoms' adsorption on solid surface is improved comparing to the original PBE functional [6].

## 2.2 Use of DFT for modeling MOX gas sensor

Surface science is a research area [7-10] where the experimental results are usually combined with theoretical calculations. In part, this is due to the fact that several of the experimental techniques do not provide completely self-explanatory observations. Surface science experiments, e.g., XPS, TPD and FTIR are supported by theoretical calculations, and vice versa. The interaction of different MOX surfaces with gas molecules is a subject of high interest due to its importance to both fundamental understanding of matters and practical value in real applications such as heterogeneous catalysis [11], gas sensing, etc. Of course, not every experimentalist can have their work immediately compared to the corresponding theoretical work and similarly it happens to the computational groups. This problem is often covered by those review papers that overview the results from both perspectives in order to find the most reliable statement about the question of interest. The examples of such reviews on MOX and gas interactions are refs.[12-14].

From a practical point of view, DFT calculation generates a huge amount of information related to the different aspects of gas-surface interactions, such as the adsorption structures, binding energy values and estimation of the vibration frequencies. Most of them can be correlated to the results from real experiments. DFT also goes beyond the experiments by predicting the complete network of surface reactions, which are difficult to draw even with very advanced surface science techniques [15]. Therefore, DFT calculations are also often used to complete the experimental results. In table 2.1, a list of properties that can be calculated by DFT and the corresponding experimental technique is given.

We can see that most properties in table 2.1 can be related to the gas sensing character of a MOX gas sensor. And there are indeed many works have explored the capability of DFT in explaining the gas sensing phenomena. Majority of these works [16-21] have predefined one or more surface facets and then determined the binding geometry and binding energy using DFT, on that basis, the change in band structure and charge transfer could be calculated to make a direct connection between the adsorption of gas molecules and the resistance change of the sensor. And simply comparing the molecular adsorption energy can lead to the prediction of competitive sensing of different gases by the same MOX [20]. In addition, by computing the oxygen vacancy formation energy, which is seen as an indicator of the adsorbed surface oxygen density, the enhanced sensitivity of Cu doped SnO<sub>2</sub> gas sensor could was explained [22].

**Table 2.1** Parameters that can be experimentally explored and estimated by DFT calculation

<b>Physical/chemical properties</b>	<b>Experimental techniques</b>	<b>DFT calculations</b>
predominant surface plane	XPS, STM, AFM	surface energy calculation
binding geometry	XPS, STM	structure relaxation
binding energy	TPD	adsorption energy calculation
vibration frequency	FTIR	vibration frequency calculation
band structure	UPS	band structure calculation
charge transfer	Resistance	charge difference analysis
surface reaction path	STM	relative energy calculation

However, above static view of gas-surface interaction has apparently neglected any chemical reactions among the gas molecules, the surface adsorbed oxygen ( $O_2^-$ ,  $O^-$ ,  $O^{2-}$ ) and the surface itself. It is sufficient under two conditions: i) the sensing material works in the low temperature, e.g., room temperature, that only  $O_2^-$  exists on the surface and the thermally activated reaction does not take out; ii) the gas of interest is chemically inert, e.g.,  $N_2$ , it weakly adsorbs on the surface but not participate in any surface reaction. However, such scenario is contradictory to the classic view of reducing/oxidizing gas sensing by MOX as the electron trapping effect of surface oxygen species ( $O_2^-$ ,  $O^-$ ,  $O^{2-}$ ) and their reactions with reducing/oxidizing gases have been considered to play a major role in gas sensing where neutral oxygen species, such as physical adsorbed  $O_2$ , and lattice ions,  $O^{2-}$  are assumed to be not involved.

DFT calculations on the other hand routinely predicts the minima energy path of chemical reactions and has been successfully applied to model the surface reactions in heterogeneous catalysis [11, 23]. It was adopted by Ducéré et al. [24] to obtain the energetic and charge data for the kinetic modeling of MOX gas sensing. There, the characteristic response of the gas sensor was attributed to the evolution of the concentrations of various species present at the surface, and the corresponding charge transfers.

After all, DFT modeling of MOX gas sensing in a reactive environment has been rarely explored. It is therefore one of the guiding concepts of the DFT calculations in this work.

## References

- [1] D.A. McQuarrie, J.D. Simon, *Physical Chemistry: A Molecular Approach*, University Science Books, 1997.
- [2] D.C. Young, *Computational Chemistry: A Practical Guide for Applying Techniques to Real-World Problems*, John Wiley & Sons, 2001.
- [3] W. Koch, M.C. Holthausen, *A Chemist's Guide to Density Functional Theory*, WILEY-VCH, 2001.
- [4] M. Balkanski, R.F. Wallis, *Semiconductor Physics and Applications* Oxford University Press, 2000.
- [5] B. Hammer, L.B. Hansen, J.K. Nørskov, Improved adsorption energetics within density-functional theory using revised Perdew-Burke-Ernzerhof functionals, *Physical Review B*, 59 (1999) 7413-7421.
- [6] J.P. Perdew, K. Burke, M. Ernzerhof, Generalized Gradient Approximation Made Simple, *Physical Review Letters*, 77 (1996) 3865-3868.
- [7] L. Mino, A.M. Ferrari, V. Lacivita, G. Spoto, S. Bordiga, A. Zecchina, CO Adsorption on Anatase Nanocrystals: A Combined Experimental and Periodic DFT Study, *The Journal of Physical Chemistry C*, 115 (2011) 7694-7700.
- [8] V. Hornebecq, C. Knöfel, P. Boulet, B. Kuchta, P.L. Llewellyn, Adsorption of Carbon Dioxide on Mesoporous Zirconia: Microcalorimetric Measurements, Adsorption Isotherm Modeling, and Density Functional Theory Calculations, *The Journal of Physical Chemistry C*, 115 (2011) 10097-10103.
- [9] Y.X. Pan, D. Mei, C.J. Liu, Q. Ge, Hydrogen Adsorption on Ga<sub>2</sub>O<sub>3</sub> Surface: A Combined Experimental and Computational Study, *The Journal of Physical Chemistry C*, 115 (2011) 10140-10146.
- [10] M. Habgood, N. Harrison, An *ab initio* study of oxygen adsorption on tin dioxide, *Surface science*, 602 (2008) 1072–1079.
- [11] K. Honkala, A. Hellman, I.N. Remediakis, A. Logadottir, A. Carlsson, S. Dahl, C.H. Christensen, J.K. Nørskov, Ammonia Synthesis from First-Principles Calculations, *Science*, 307 (2005) 555-558.
- [12] J.M. Vohs, Site Requirements for the Adsorption and Reaction of Oxygenates on Metal Oxide Surfaces, *Chemical Reviews*, (2012).
- [13] M. Batzill, U. Diebold, The Surface and Materials Science of Tin Oxide, *Prog. Surf. Sci.* , 79 (2005) 47–154.
- [14] U. Diebold, The surface science of titanium dioxide, *Surface Science Reports*, 48 (2003) 53-229.
- [15] S.-C. Li, L.-N. Chu, X.-Q. Gong, U. Diebold, Hydrogen Bonding Controls the Dynamics of Catechol Adsorbed on a TiO<sub>2</sub>(110) Surface, *Science*, 328 (2010) 882-884.

- [16] Q.Z. Yuan, Y.P. Zhao, L.M. Li, T.H. Wang, *Ab Initio* Study of ZnO Based Gas Sensing Mechanisms: Surface Reconstruction and Charge Transfer, *J. Phys. Chem. C*, (2009) 6107–6113.
- [17] A. Maiti, J.A. Rodriguez, M. Law, P. Kung, J.R. McKinney, P.D. Yang, SnO<sub>2</sub> Nanoribbons as NO<sub>2</sub> Sensors: Insights from First Principles Calculations, *Nano Lett.*, 3 (2003) 1025–1028.
- [18] M. Hu, J. Zhang, W.D. Wang, Y.X. Qing, *Ab-initio* Density Functional Theory Study of WO<sub>3</sub> NH<sub>3</sub>-sensing Mechanism, *Chin. Phys. B*, 20 (2011) 0821011–0821018.
- [19] B. Wang, J. Nisar, R. Ahuja, Molecular Simulation for Gas Adsorption at NiO (100) Surface, *ACS Applied Materials & Interfaces*, 4 (2012) 5691-5697.
- [20] J.D. Prades, A. Cirera, J.R. Morante, J.M. Pruneda, P. Ordejón, *Ab initio* study of NO<sub>x</sub> compounds adsorption on SnO<sub>2</sub> surface, *Sensors and Actuators B: Chemical*, 126 (2007) 62-67.
- [21] J.D. Prades, A. Cirera, J.R. Morante, *Ab initio* calculations of NO<sub>2</sub> and SO<sub>2</sub> chemisorption onto non-polar ZnO surfaces, *Sensors and Actuators B: Chemical*, 142 (2009) 179-184.
- [22] W. Wei, Y. Dai, B.B. Huang, Role of Cu Doping in SnO<sub>2</sub> Sensing Properties Toward H<sub>2</sub>S, *J. Phys. Chem. C*, 115 (2011) 18597–18602.
- [23] R.M. Yuan, G. Fu, X. Xu, H.L. Wan, Mechanisms for Selective Catalytic Oxidation of Ammonia over Vanadium Oxides, *J. Phys. Chem. C*, (2011) 21218–21229.
- [24] J.-M. Ducéré, A. Hemeryck, A. Estève, M.D. Rouhani, G. Landa, P. Ménini, C. Tropis, A. Maisonnat, P. Fau, B. Chaudret, A computational chemist approach to gas sensors: Modeling the response of SnO<sub>2</sub> to CO, O<sub>2</sub>, and H<sub>2</sub>O Gases, *Journal of Computational Chemistry*, 33 (2012) 247-258.



## 3. Methods

Aiming at understanding the fundamental sensing mechanisms for developing better sensors, this PhD work carried out a broad range of activities including material preparation, sensor device fabrication and characterization, DFT modeling and *ex-situ* analysis. The details of these methods are given in this Chapter.

### 3.1 Preparation of nanowires

The vast majority of the nanowires used in this work were prepared by other researchers with different methods. SnO<sub>2</sub> nanowires were produced by Prof. S. Mathur's group at the University of Cologne, using a metal catalyzed CVD process with tin(IV) tert-butoxide (Sn(O*t*Bu)<sub>4</sub>) as the precursor [1]. The decoration of the SnO<sub>2</sub> nanowires with CuO particles to produce CuO@SnO<sub>2</sub> nanowires followed a CVD procedure described in ref.[2].

CuO nanowires were locally produced in our lab with the thermal oxidation method [3-5]. Commercial Cu foils with 0.25 mm thickness (99.9% purity, Alfa Aesar) were used as the raw material. Prior to oxidation, Cu foils were soaked in 1.5 M HCl for 1 min to remove the native oxide, rinsed with de-ionized water and dried in nitrogen. Then, the samples were placed in a muffle furnace pre-heated to 500°C, and kept in the ambient atmosphere for a period of 0.5 to 10h. Black layers were formed on both sides of the foil after thermal oxidation. Crystallographic structure was characterized by X-ray diffraction (XRD) technique using a Bruker D8 Advance diffractometer with Cu K $\alpha$  radiation. Surface and cross sectional morphologies were examined

with a scanning electron microscopy (SEM) (Serie Auriga, Zeiss), which is also equipped with X-ray spectrometer (Oxford) for Selected Area Energy-Dispersive X-ray Spectroscopy (SAEDS) analysis.

ZnO nanowires were produced by Dr. J. D. Fan by a hydrothermal process reported earlier [6]. In brief, an 80 nm thick of ZnO seed layer were first sputtered on indium doped tin oxide (ITO) glass. The ITO glass was then placed in the growth solution that consisted of 0.02 M zinc nitrate, 0.015 M hexamethylenetetramine (HMTA), 0.004 M polyethyleneimine (end-capped, molecular weight 800g/mol) and 0.024 M ammonium hydroxide. The solution was heated to 88°C, and after 3h, ZnO nanowire will grow to about 6µm long and have diameters between 100 to 200nm. The resulting ZnO arrays were rinsed with Mili-Q water and dried with nitrogen flow. More characterization results, e.g., XRD, SEM, can be found in ref. [6]. The solution of ZnO nanowires was obtained by sonicating the ITO substrate in isopropanol.

## **3.2 Fabrication of electrical contacts to nanowires**

### **3.2.1 Individual nanowires**

To make the electrical contacts to individual nanowires, they were first dispersed in an organic solvent (iso-propanol or ethanol) by sonication. Drop casting 10µl of the solution onto a 7×7 mm size SiO<sub>2</sub>-on-Si chip with Ti/Au micro electrodes deposited over the top insulator layer transfers certain amount of nanowires onto the chip. To electrically contact the nanowire with the micro electrodes, the chip was brought to the dual beam system (FEI strata 235) to perform the deposition of Pt strips.

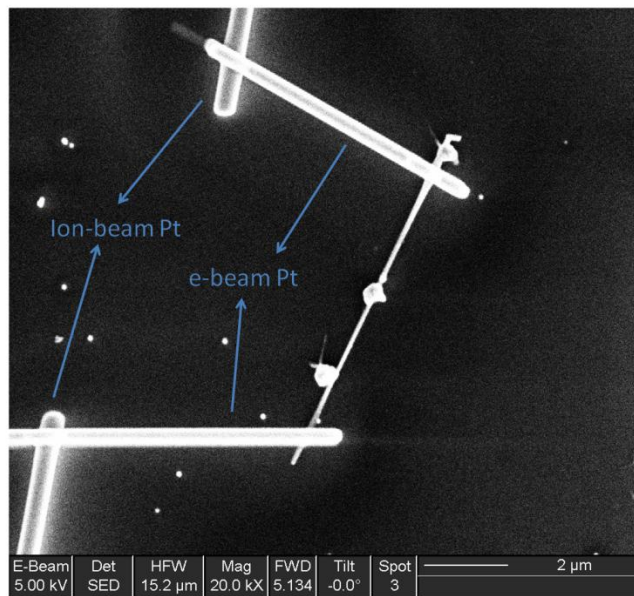


**Figure 3.1** 2-probe contacted CuO@SnO<sub>2</sub> nanowire

The deposition process followed the protocol developed earlier in the group [7]. Electron imaging (SEM mode) was used to locate an individual nanowire with the desired dimension (length > 5 μm). Pt strips that directly contact the nanowire were deposited with electron beam and the Pt strips that extend to micro electrodes were deposited with Ga<sup>+</sup> ion beam (shown and marked in figure 3.1). This approach avoids the milling at the Pt-SnO<sub>2</sub> interface by the ion beam [8, 9] and minimizes the doping of the nanowire sensing surface by the Pt as the electron beam features both zero etching effect and more confined area of deposition. Furthermore, direct imaging of nanowire with ion beam was minimized. The parameters generally used in the deposition process are given in table 3.1. The thickness of Pt strips was proportional to the deposition time, which can be estimated by the machine when a wanted thickness value is typed in, or vice versa, the user can control the deposition time to obtain a required thickness.

To be able to perform the electrical measurement on the device, the chip was glued onto an alumina substrate with macro-size electrodes of Au or Pt. The micro and macro-electrodes were then connected by Au wire using a wire bonder (TPT).

**Table 3.1** Experimental parameters used for the Pt deposition

<b>Beam type</b>	<b>electron</b>	<b>ion</b>
Acceleration voltage	5kV	30kV
Spot size	3	N/A
Current	200 $\mu$ A	30pA
Pt precursor	C <sub>5</sub> H <sub>4</sub> CH <sub>3</sub> Pt(CH <sub>3</sub> ) <sub>3</sub>	
Pt strip dimension (length $\times$ Width)	10 $\times$ 0.2 $\mu$ m	20 $\times$ 0.2 $\mu$ m
Dwell time	10 $\mu$ s	0.2 $\mu$ s
Overlap	90%	0
Sputtering rate	0.032	1
time	10-20min	approx.2min
thickness	hundreds of nm	$\sim$ 1 $\mu$ m

### 3.2.2 Dielectrophoretic assembly of ZnO nanowires onto $\mu$ HP substrates

$\mu$ HPs with different design were obtained from Cambridge CMOS Sensors [10]. The  $\mu$ HPs used in this work is the model HVMS36C, in which the IDEs have a Au top layer over the Al tracks. The Au is more resistive to oxidation and the rough Au surface (produced by electroless plating [10]) also provides better adhesion to the later deposited nanowires. As shown in figure 3.2, there are two identical  $\mu$ HPs on a single chip, each one with several Au bond pads connected to the heater and IDEs. The IDEs cover a circular area of 200 $\mu$ m in diameter and the gap between the IDEs tracks is 10  $\mu$ m. The heating element that made of Si is buried under the IDEs with the

SiO<sub>2</sub> insulation. And the circular SiO<sub>2</sub> insulating membrane around the IDEs/heater has a diameter of about 800μm. The maximum temperature it can reach is about 700°C, while the power consumption is only about 40mW at 450°C.

The chip was glued on a ceramic plate and wire (Au) bonding was made between the bond pads on μHPs and the Pt pads on the ceramic plate which were then electrically connected by the tungsten probes. A micropipette was used to apply 2 drops (~2.5μl each) of ZnO nanowire solution onto the micro hot plate when the AC potential was applied on the IDEs with a function generator (TG2000, TTi). The voltage applied was 15 V<sub>p-p</sub> (peak to peak) in square wave at 5MHz. Once the solvent has evaporated, the AC signal was turned off. The morphology of aligned nanowires on μHPs was examined with the SEM.

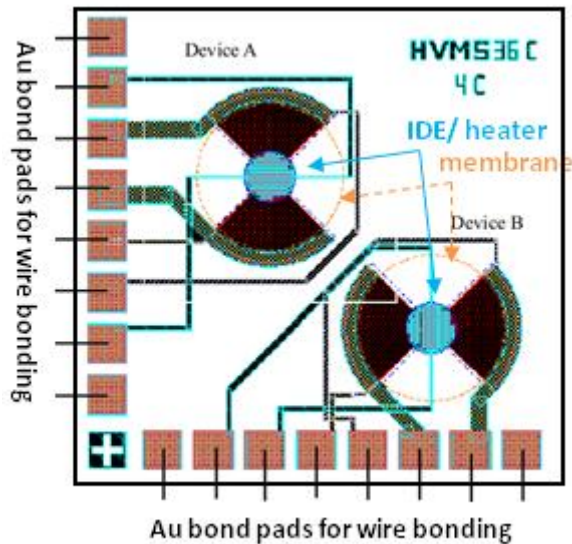


**Figure 3.2** Layout of the μHP substrate (HVMS36C).

### 3.3 Electrical measurements and gas sensing

The devices were placed in an air tight chamber (LTS350, Linkam Scientific) for electrical characterization and gas sensing tests. As shown in figure 3.3, the chamber is equipped with in-built heater to heat the nanowire and maximum of four tungsten probes to contact the macro-electrodes. Electrical measurements were performed with source measurement units (2400, 2602, 2635A, Keithley). To protect the nanowire from damaging by current overloading, tests were generally performed in current sourcing and voltage reading mode. The sourcing currents were usually below 100nA. Only after the resistance of the device under test was known, voltage sourcing and current reading would be performed.

Gas mixture was introduced by a gas mixer (MGP2, Gometrics) with integrated mass flow controller by mixing the synthetic air (SA) with the gas of interest from calibrated gas cylinder (Linde). The total flow rate sending to the chamber was always 200ml/min (sccm/min). By mixing the dry SA with the humidified SA from a gas washer, different RH levels were obtained. A solid state relative humidity (RH) sensor (SHT21, Sensirion) was planted in the inlet gas pipe to monitor the RH simultaneously. From the response curves, the sensitivity was calculated according to  $S = R_{SA}/R_{gas}$  when resistance drops or  $S = R_{gas}/R_{SA}$  when resistance rises. Here  $R_{SA}$  and  $R_{gas}$  are resistances in the SA and test gas, respectively.

In the case that the nanowire was contacted in 2-probe configuration, the resistance of the Pt strips will contribute to the measured resistance of the device. To clarify this problem, the electrical properties of the deposited Pt strips by both methods were determined by measuring their resistance in 4-probe configuration. Figure 3.4 shows the Pt strip (in this case, ion beam deposited) deposited on top of 4 parallel Au/Ti electrodes. It was found that the as deposited Pt

strips have rather different resistance at room temperature (RT) when different beams were used. A resistance of  $800\Omega$  was measured between the inner electrodes ( $5\mu\text{m}$  in length Pt) with 4-probe methods for the ion-beam deposited Pt, whereas that could be up to  $200\text{M}\Omega$  for the e-beam deposited Pt ( $2.5\mu\text{m}$  in length Pt). Annealing at  $300^\circ\text{C}$  had both of them decreased, the ion-beam deposited Pt's resistance decreased to  $150\Omega$  in average and e-beam deposited Pt to  $500\Omega$ . Once after the annealing, further adjustments in temperature had no effect on the resistance value. These results indicate that good conductivity can be obtained directly from the as deposited ion-beam deposited Pt, while the conductivity of the e-beam deposited Pt has to be activated by removing C contents with high temperature [11, 12]. As will be shown in the following chapters, the resistances of the Pt strips are usually several orders of magnitudes smaller than that of nanowires, and as a result, it will not affect the electrical measurements.

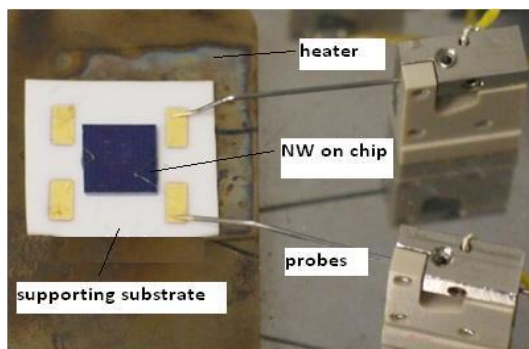


**Figure 3.3** The single nanowire device sitting on the heater and connected by tungsten probes inside the test chamber.

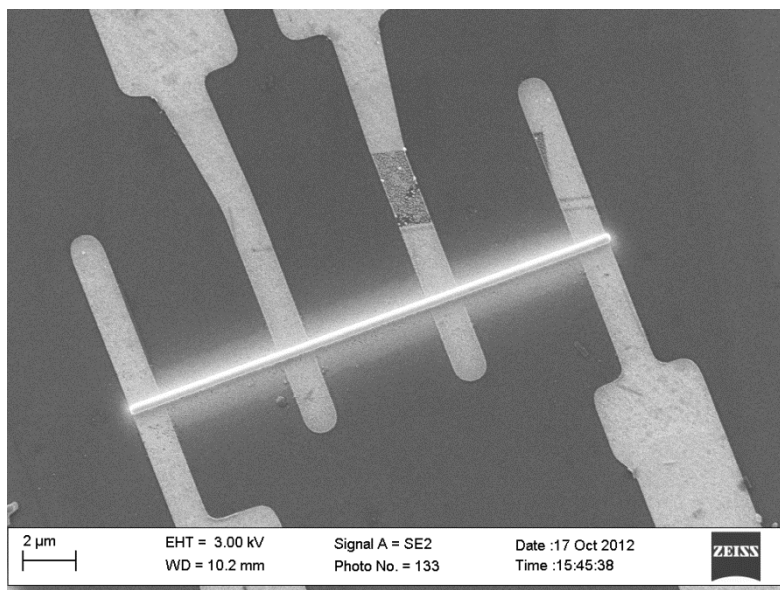


**Figure 3.4** Ion-beam deposited Pt strip ready to be measured in 4-probe configuration.

### 3.4 DFT calculations

DFT calculations were performed with the Vienna *ab-initio* simulation Package (VASP) [13, 14]. Core electrons were represented by the projector-augmented wave [15] (PAW) potentials while plane waves were used to represent valence electrons. A cut off energy of 400eV for the kinetic energy of these plane waves was applied and the Revised-Perdew-Burke-Ernzerhof (RPBE) [16] functional was chosen to treat the exchange correlation. The surface slab used to perform the calculations contained five SnO<sub>2</sub> (110) atomic layers with a (2×1) super cell configuration (figure 3.5). 10Å of vacuum space was placed between the slabs to simulate the surface. K-point sampling was set to 4×4×1 for the surface slab and 1×1×1 for the molecules in vacuum adopting the Monkhorst-Pack grids. The three top trilayers together with the adsorbates were allowed to relax during structure optimization. Geometry relaxation was performed until



the energy change of electronic step goes under  $1 \times 10^{-5}$  eV and ionic step below  $1 \times 10^{-4}$  eV. Spin polarization was enabled when needed. The transition state search for the dissociation and formation of species was performed with the nudged elastic band (NEB) [17] method implemented in VASP. Vibrational frequencies were calculated by diagonalization of the numerically calculated Hessians (step 0.02 Å) to verify the nature of the transition states. The accuracy of this model was verified in a previous work [18].

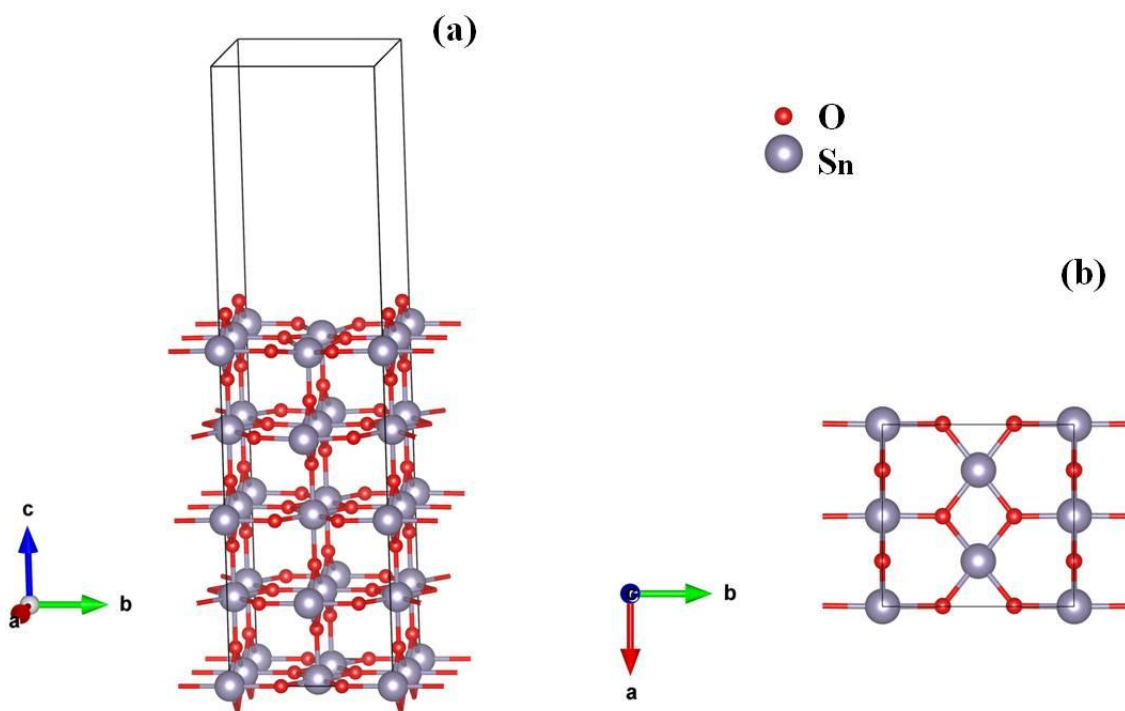


**Figure 3.5** (a) The surface slab. (b) Top view of the (2×1) SnO<sub>2</sub> (110) surface.

The adsorption energy of gas molecules was given by the following equation:

$$E_{ads} = E_{tot} - E_{sur} - E_{mol} \quad (3.1)$$

Where  $E_{tot}$  is the ground state energy of the surface with the adsorbed molecule,  $E_{sur}$  is the initial energy of the surface slab and  $E_{mol}$  is that for the molecule in vacuum. A negative value of  $E_{ads}$  indicates an exothermic (favorable) adsorption process.

The energy barrier and reaction energy of a minimum energy path was defined as

$$E_b = E_m - E_i \quad (3.2)$$

$$E_r = E_f - E_i \quad (3.3)$$

Where  $E_b$  is the energy barrier,  $E_m$  is the energy at the maximum energy point with a negative frequency,  $E_i$  is the initial state energy and  $E_f$  is the final state energy.

## References

- [1] S. Mathur, S. Barth, H. Shen, J.-C. Pyun, U. Werner, Size-dependent Photoconductance in SnO<sub>2</sub> Nanowires, *small*, 1 (2005) 713–717.
- [2] I. Giebelhaus, E. Varechkina, T. Fischer, M. Rumyantseva, V. Ivanov, A. Gaskov, J.R. Morante, J. Arbiol, W. Tyrra, S. Mathur, One-dimensional CuO-SnO<sub>2</sub> p-n heterojunctions for enhanced detection of H<sub>2</sub>S, *Journal of Materials Chemistry A*, 1 (2013) 11261-11268.
- [3] X. Jiang, T. Herricks, Y. Xia, CuO Nanowires Can Be Synthesized by Heating Copper Substrates in Air, *Nano Letters*, 2 (2002) 1333-1338.
- [4] G. Filipič, U. Cvelbar, Copper oxide nanowires: a review of growth, *Nanotechnology*, 23 (2012) 194001.
- [5] C.H. Xu, C.H. Woo, S.Q. Shi, Formation of CuO nanowires on Cu foil, *Chemical Physics Letters*, 399 (2004) 62-66.
- [6] J. Fan, Y. Hao, A. Cabot, E.M.J. Johansson, G. Boschloo, A. Hagfeldt, Cobalt(II/III) Redox Electrolyte in ZnO Nanowire-Based Dye-Sensitized Solar Cells, *ACS Applied Materials & Interfaces*, 5 (2013) 1902-1906.
- [7] F.H. Ramirez, A. Tarancon, O. Casals, J. Rodriguez, A. Romano-Rodriguez, J.R. Morante, S. Barth, S. Mathur, Y. Choi T, D. Poulidakos, V. Callegari, P.M. Nellen, Fabrication and Electrical Characterization of Circuits based on Individual Tin Oxide Nanowires, *Nanotechnology*, 17 (2006) 5577–5583.
- [8] J.J. Ke, K.T. Tsai, Y.A. Dai, J.H. He, Contact transport of focused ion beam-deposited Pt to Si nanowires: From measurement to understanding, *Applied Physics Letters*, 100 (2012) 053503-053504.
- [9] D. Tham, C.Y. Nam, J.E. Fischer, Microstructure and Composition of Focused-Ion-Beam-Deposited Pt Contacts to GaN Nanowires, *Advanced Materials*, 18 (2006) 290-294.
- [10] S. Santra, P.K. Guha, S.Z. Ali, P. Hiralal, H.E. Unalan, J.A. Covington, G.A.J. Amaratunga, W.I. Milne, J.W. Gardner, F. Udrea, ZnO nanowires grown on SOI CMOS substrate for ethanol sensing, *Sensors and Actuators B: Chemical*, 146 (2010) 559-565.
- [11] Y. Tsukatani, N. Yamasaki, e. al, Transport Properties of Pt Nanowires Fabricated by Beam-Induced Deposition, *Japanese Journal of Applied Physics*, 44 (2005).
- [12] R.J. Díaz, Fabrication Technology and Characterisation of Advanced Single nanowire-based Metal Oxide Gas Sensors on Microhotplates, in: *Departament d'Electrònica, Universitat de Barcelona*, 2012.
- [13] G. Kresse, J. Hafner, *Ab Initio* Molecular Dynamics for Liquid Metals, *Phys. Rev. B*, 47 (1993) 558–561.

- [14] G. Kresse, J. Furthmüller, Efficient Iterative Schemes for *Ab initio* Total-energy Calculations using a Plane-wave Basis Set, *Phys. Rev. B*, 54 (1996) 11169–11186.
- [15] G. Kresse, D. Joubert, From Ultrasoft Pseudopotentials to the Projector Augmented-wave Method, *Phys. Rev. B*, 59 (1999) 1758–1775.
- [16] B. Hammer, L.B. Hansen, J.K. Nørskov, Improved Adsorption Energetics within Density-functional Theory using Revised Perdew-Burke-Ernzerhof Functionals, *Phys. Rev. B*, 59 (1999) 7413–7421.
- [17] G. Henkelman, B.P. Uberuaga, H. Jonsson, A Climbing Image Nudged Elastic Band Method for Finding Saddle Points and Minimum Energy Paths, *J. Chem. Phys.*, 113 (2000) 9901–9904.
- [18] N. Lopez, J.D. Prades, F.H. Ramirez, J.R. Morante, S. Mathur, Bidimensional versus Tridimensional Oxygen Vacancy Diffusion in  $\text{SnO}_{2-x}$  Under Different Gas Environments, *Phys. Chem. Chem. Phys.*, 12 (2010) 2401–2406.

## **4. NH<sub>3</sub> sensing with SnO<sub>2</sub> nanowire and the influence of H<sub>2</sub>O**

Unlike the sensing of well-known and simpler gas molecules, e.g., CO [1, 2], the detailed sensing mechanism of NH<sub>3</sub> by SnO<sub>2</sub> remained partially unsolved before this dissertation. The most common explanation to describe the NH<sub>3</sub> response was based on the classic conduction model of MOX [3], which describes the sensing mechanisms as the result of gas molecules interacting with surface oxygen species (O<sub>2</sub><sup>-</sup>, O<sup>-</sup>, O<sup>2-</sup>) and the related charge transfer process. The physical and chemical processes of how NH<sub>3</sub> molecule interacts with SnO<sub>2</sub> surface and the oxygen species were unknown and these are where the DFT calculations are helpful in this work. In this chapter, the NH<sub>3</sub> sensing property of individual SnO<sub>2</sub> nanowire was examined and empirically modeled. The interference by water was also evaluated and explained. DFT calculations showed us the surface chemistry between SnO<sub>2</sub>, NH<sub>3</sub> and H<sub>2</sub>O, providing explanations to the experimental data.

### **4.1 Introduction**

#### **4.1.1 SnO<sub>2</sub> as the NH<sub>3</sub> sensor**

NH<sub>3</sub> is a dangerous gas to the environment and humans. It is odorous, toxic, flammable and corrosive. It can cause irritation and fatal airway obstruction to humans. The recommended exposure limit for NH<sub>3</sub> is 25ppm as an 8-h time-weighted average (TWA) or 35ppm as a short term exposure limit [4].

Liquid NH<sub>3</sub> is mass produced as a precursor of N fertilizer (ammonium nitrate), refrigerant and cleaning agent, its extensive use intrigued the needs of sensors for indoor air quality control and leakage detection. The significance of the latter was highlighted by two recent accidents [5, 6] happened in China and US, causing the casualty of hundreds and massive damages.

Meanwhile, a potential use of NH<sub>3</sub> sensors has been found in the combustion exhaust control of power plants [7] and vehicle engines [8]. Where NO<sub>x</sub> (NO and NO<sub>2</sub>) is removed by the selective catalytic reduction (SCR) processes with NH<sub>3</sub> [9]:



If the NH<sub>3</sub> feed in is not well controlled, such a process may leave excessive NH<sub>3</sub> released into the atmosphere and the practical solution is the regulation of NH<sub>3</sub> input by simultaneously monitoring its concentration in the exhaust.

Nanowires have become one of most studied materials by the nanoscience community. MOX nanowire based gas sensors have emerged for NH<sub>3</sub> sensing, either with bundle or individual nanowires. They often possess good sensitivity and faster response time than the porous thick film sensors [7, 10-13] because the gas does not pass through the pores typical of thick film sensors and as a result diffusion effects are minimized. Summarized in table 4.1 is a survey of recently published works on NH<sub>3</sub> sensing with nanostructured resistive type sensors. It can be seen that the common choices of MOX for NH<sub>3</sub> sensing are SnO<sub>2</sub>, WO<sub>3</sub>, or ZnO. In general, SnO<sub>2</sub> based sensors give response from ppm to sub-ppm level. The sensitivity, optimal working temperature, response time and detection limit depend on the method of preparation. Higher sensitivities are often seen with smaller diameters. Sensors made from nanoparticles, thin films,

carbon nanotube and polymer nanowires are also included in table 4.1 for comparison. Shall be noted, sensitivities (S) are given at the optimized working temperature of each device. The response time is dependent on the working temperature and gas flow rate applied, and some of the values listed in the table are based on estimation.

**Table 4.1** A survey of the characteristics of NH<sub>3</sub> sensors based on nanomaterials

Material	Fabrication methodology	Dimensions*	Sensitivity (S=R <sub>SA</sub> /R <sub>gas</sub> or R <sub>gas</sub> /R <sub>SA</sub> )	Response time	Recovery time	Comment on selectivity
Individual SnO <sub>2</sub> nanowire[14]	PVD	d: 100nm, L: ~15μm	S=1.3 for 100ppm (250°C)	~1min	~3min	smaller response to CO
SnO <sub>2</sub> nanowires[15]	PVD	d: 40-85nm, L: 200-900μm	S=9 for 300ppm, S=17 for 1000ppm (200°C)	~seconds	~seconds	LPG, NH <sub>3</sub> sensitivity peak at different temperature
SnO <sub>2</sub> nanorods[16]	PECVD on SiO <sub>2</sub> /Si	d: 5-15nm, L: 160-300nm	S=3 for 100ppm, S=30 for 500ppm (200°C)	~30min	>30min	response to CH <sub>3</sub> OH
SnO <sub>2</sub> nanocluster film/Pd layer[11]	sputtering+thermal oxidation	cluster size: 3-10nm, 1nm Pd film	response to 0.4ppm, S=100 for 50ppm (160°C)	~seconds	~min	S=60 for 100ppmH <sub>2</sub> (80°C)
SnO <sub>2</sub> porous nanofiber[17]	electro spinning	d: 80-150nm, L: ≥10μm	S=3 for 5ppm, S=60 for 500ppm at 280°C, about 25%RH air	~5s	~8s	response to CH <sub>3</sub> COCH <sub>3</sub> , C <sub>2</sub> H <sub>5</sub> OH
SnO <sub>2</sub> :Pd porous film[12]	sol-gel/microdroplet	Particle d:30-100nm	S=5 for 5ppm (280°C)	~15min	~30min	
Sb doped SnO <sub>2</sub> nanoparticle[13]	non aqueous solvothermal	12nm particle, 600μm film	S=9 at 50ppm, S=11 at 100ppm (79°C) 2ppm detectable	~3min	~3min	
SnO <sub>2</sub> nanocrystalline nanotube[18]	AAO template/sol gel	20nm crystalline, 300nm outer diameter, 150nm inner diameter	S=1.2 for 50ppm, S=1.5 for 100ppm ( 200°C)	~10s		better to ethahol
WO <sub>3</sub> : Cr[12]	solgel/micro droplet	crystallite size:~50nm	S=3 for 5ppm (350°C)	~15min	~30min	
WO <sub>3</sub> particle/MoO <sub>3</sub> /Au particle[7]	thermal decomposition/impregnation or evaporation	N/A	S=5 to 6 for 5ppm (5%MoO <sub>3</sub> , 450°C, gas:2%O <sub>2</sub> in N <sub>2</sub> )	~1min	~10min	S=3-7 for 100ppm NO

W <sub>18</sub> O <sub>39</sub> [19]	hydrothermal/droplet/	d:2-5nm, L: $\mu$ m, BET area: 151m <sup>2</sup> /g	S<1.1 for 100ppb or 5ppm (room temp, air or N <sub>2</sub> ) base line drift	~seconds	~200s	
WO <sub>3</sub> nanowire networks[20]	thermal evaporation	40-200nm diameter, 1-10 $\mu$ m total size	S=3 for 30ppm	> 10 min		S = 6 for 50 ppb NO <sub>2</sub> ; sensitive to H <sub>2</sub> S
MoO <sub>3</sub> film/Ti layer[10]	sputtering/sputtering	thickness: 450nm/8 to 90nm	S=20 for 50ppm (200°C)	~20s to 50ppm NH <sub>3</sub>	~80s	S(NH <sub>3</sub> )/S(H <sub>2</sub> )=3, S(NH <sub>3</sub> )/S(CO)=10, 200ppmNH <sub>3</sub> , 1000ppmH <sub>2</sub> , 30ppmCO
ZnO nanowire array/Pt loading[21]	CVD	d: 100nm	S=1.25 for 200ppm (300°C)	>100 seconds		
ZnO nanorods[22]	Hydrothermal on sputtered Zn	L: 1 $\mu$ m, d: 50nm	S=5 for 200ppm (250°C)	~10min	~30min	response to H <sub>2</sub> , CO,
Single ZnO nanowire[23]	CVD	100-200nm diameter, $\mu$ m long	S=1.1 for 100ppm (RT)			more sensitive to H <sub>2</sub>
Hierarchical ZnO nanorods[24]	wet chemical	d: 20nm-80nm thorn on 400nm rod	S=4 for 50ppm; S= 7 for 100ppm ( 200°C)	~10s	~20s	more sensitive to ethanol
TiO <sub>2</sub> thin film[25]	sputtering	crystallite size: 20nm	S=500 for 500ppm (250°C), static system, vacuumed 0.1mbar	~100s	~100s	
single In <sub>2</sub> O <sub>3</sub> nanowire FET[26]	CVD	d: 10nm, L: $\mu$ m	S=15 for 200ppm (UV activation)	~1000s		
TeO <sub>2</sub> nanowire[27]	evaporation	d: 30-200nm, L: several $\mu$ m	S=1.02 for 100ppm (RT)	~10min	~30min	sensitive to NO <sub>2</sub> , H <sub>2</sub> S
single wall Carbon nanotube[28]	arcdischarge	d: 1nm, L: 5-15 $\mu$ m	S=1.15 for 10ppm (80°C)	~100s	~100s	opposite response to CO
Polypyrrole nanowire array[29]	polymerization in AAO	d: 50nm	S=1.23 for 25ppm	>100s		
single polypyrrole nanowire[30]	polymerization in AAO	d: 300nm	S=1.1 for 100ppm (RT)	>10min		
polyaniline nano network[31]	Electro-chemical polymierzation	d: 40-80nm	S=1.6 for 0.5ppm and S=11 for 100 ppm (RT)	~50/100 s	~100s	
single polyaniline/ PEO nanowire[32]	scanning electrospinning	d:100-500nm, L:10 $\mu$ m	0.5ppm sensible, S=14 for 50ppm	~200s	~10s to min	

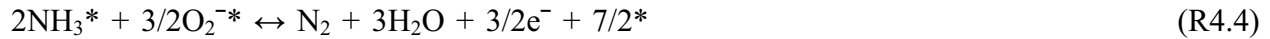
\*d: diameter, L: length



#### 4.1.2 Standard formulation of NH<sub>3</sub> sensing with n-type MOX

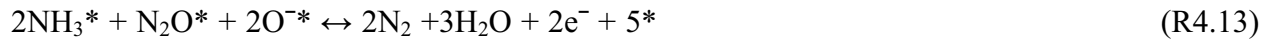
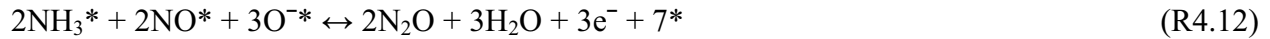
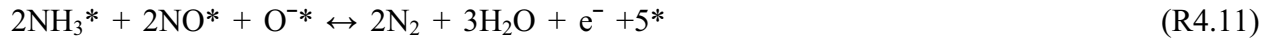
The sensing mechanism of NH<sub>3</sub> with n-type metal oxides (MOX) has been described as the interaction of gas molecules with pre-adsorbed oxygen species including molecular O<sub>2</sub><sup>-</sup> and atomic O<sup>-</sup>, O<sup>2-</sup> at elevated temperatures [33]. These pre-adsorbed oxygen species withdraw electrons from the MOX, creating a depletion layer that acts as a non conductive region at the surface or charge transfer barrier between grains. The resistance of n-type MOX materials thus increases and it decreases for p-type MOXs. When other gas molecules approach the MOX, chemical reactions occur at the surface accompanied with charge transfer toward or from the MOX which triggers the sensitive change of the resistance.

In the case of NH<sub>3</sub>, an n-type MOX sensor generally responds to it by a resistance drop. A series of surface reactions with N<sub>2</sub> and H<sub>2</sub>O as the products have been proposed [34] to describe the process:



Reaction (R4.3) stands for the adsorption of ammonia from the gas phase to an empty center of the surface, which is here represented by \*. Equations (R4.4) to (R4.6) summarize three different routes involving three different types of oxygen species able to strip the H atoms from the ammonia molecules and being eliminated as water from the surface. In all these reactions, electrons are released to the MOX which leads to a decrease of the electrical resistance.

In addition, processes involving the production of NO<sub>x</sub> was proposed to explain i) the slow rising of the resistance after a steep drop due to NH<sub>3</sub> exposure, and ii) the up shifting of the MOX initial resistance value after the purge of NH<sub>3</sub>, which were reported in the past by several researchers for the SnO<sub>2</sub> sensors (not observed with the SnO<sub>2</sub> nanowire-devices studied in this work) [35, 36],



Reactions (R4.7) to (R4.13) take into account the production of NO<sub>x</sub> and their influence on the electrical property. The NO produced in reaction (R4.8) may directly affect the electronic properties of MOX by the chemisorption at the surface and the associated charge transfer. Alternatively, NO<sub>2</sub> produced by the oxidation of NO with oxygen may also chemisorb on the MOX, increasing the resistance by process (R4.10). Those abnormal sensing response of MOX to NH<sub>3</sub> is therefore explained. The N<sub>2</sub>O produced according to reaction (R4.7) and (R4.12) is considered to be a non-active molecule for the surface.

Although above reactions suitably explain the sensing mechanism of  $\text{NH}_3$  by n-type MOX sensors. Only the simple adsorption steps, i.e., (R4.3) and (R4.10) could be experimentally verified. Summarized in next section is what was already known from both experimental and theoretical perspectives.

#### 4.1.3 Surface interaction of $\text{O}_2$ and $\text{NH}_3$ on $\text{SnO}_2$ (110)

$\text{SnO}_2$  (110) is the most stable surface and it is expected to be the main orientation in crystalline nanowires. Stoichiometric  $\text{SnO}_2$  (110) has four kinds of surface atoms (as indicated in figure 4.9a): 5 coordinated Sn ( $\text{Sn}_{5c}$ ), 6 coordinated Sn ( $\text{Sn}_{6c}$ ), bridging O ( $\text{O}_{2c}$ ) and in-plane O ( $\text{O}_{3c}$ ). The  $\text{Sn}_{5c}$  is considered to be a Lewis acid site which is able to withdraw electrons from an electron rich atom, e.g., N, in the case of  $\text{NH}_3$ . According to the literature [37-39], at the standard working temperature of  $\text{SnO}_2$  sensors (473-573K), neither full oxidation toward stoichiometric surface nor complete remove of  $\text{O}_{2c}$  is possible. The surface non-stoichiometry includes the in-plane  $\text{O}_{3c}$  vacancy and bridging  $\text{O}_{2c}$  vacancy. When  $\text{O}_{2c}$  vacancies are fully presented,  $\text{Sn}_{6c}$  will become an unsaturated  $\text{Sn}_{4c}$ .

Due to its fundamental role in MOX surface science, the adsorption and dissociation of  $\text{O}_2$  on MOX, particularly on  $\text{SnO}_2$  surface were studied by many different surface techniques [3, 40-42]. It is well-accepted that oxygen appears in the molecular  $\text{O}_2^-$  form at temperatures below  $150^\circ\text{C}$  and above this temperature, the atomic forms dominate. Experiments combining work function changes and conductivity measurements [43] had led to the conclusion that the charged atomic O species exist at  $400^\circ\text{C}$  but not at  $200^\circ\text{C}$ . In parallel,  $\text{O}_2$  adsorption and dissociation have been intensively studied [44, 45] by *ab-initio* methods, the common results from these

works are as follows: molecular O<sub>2</sub> only adsorbs to the reduced SnO<sub>2</sub> (110) surface and atomic O adsorbates is then produced onto Sn<sub>5c</sub> site following the dissociation of the molecule at the O<sub>2c</sub> vacancy. In a more recent DFT study [46], adsorption energies and spin states were successfully correlated with previous experimental evidences for the different charged oxygen species including atomic O<sup>-</sup>.

Comparing to the much more studied molecules such as O<sub>2</sub>, H<sub>2</sub>O [47-49] and CO [1, 2, 50-52], our knowledge about the surface science of NH<sub>3</sub> on SnO<sub>2</sub> however was still limited before this work. Temperature programmed desorption (TPD) performed on the (110) surface by Abee and Cox [39] found that NH<sub>3</sub> adsorbs on the Sn<sub>5c</sub> site on the stoichiometric surface with the desorption temperature at around 250K, which corresponds to the Redhead estimated desorption energy of 0.64 to 0.75eV (decreasing with higher NH<sub>3</sub> concentration). And it was concluded that Sn<sub>4c</sub> atom is a stronger adsorption site when the bridging oxygen vacancies are presented. Desorption temperature and energy from the Sn<sub>4c</sub> was 470K and 1.29eV, respectively. In addition, no by-product desorption was detected from the surface, which suggests the non-dissociative nature of NH<sub>3</sub> adsorption under ultra-high vacuum conditions. Ultraviolet photoelectron spectroscopy (UPS) experiments revealed charge transfer from the NH<sub>3</sub> molecule to the surface. Nevertheless, TPD performed by Kovalenko et al. [53], on the solution-prepared SnO<sub>2</sub> particles showed two desorption peaks, one at 410K and a second spans 500 to 800K. The former was assigned to the NH<sub>3</sub> bonded with hydroxyl groups left at the SnO<sub>2</sub> surface and the latter was considered as the adsorption of NH<sub>3</sub> on either Sn<sub>4c</sub> or Sn<sub>5c</sub>. Guimon et al. [54] performed an XPS study of SnO<sub>2</sub> with pre-adsorbing NH<sub>3</sub> at 353K. N<sub>1s</sub> binding energy shift was not observed, which indicates NH<sub>3</sub> is the only adsorbate and further heating to 673K had less than half of NH<sub>3</sub> desorbed.

On the side of *ab-initio* calculations, although the surface chemistry of NH<sub>3</sub> on MOX and metal decorated MOX are topics of interest for heterogeneous catalysis [55-57] and DFT has been successfully applied to the study of NH<sub>3</sub> on TiO<sub>2</sub> [58], ZnO [59], and RuO<sub>2</sub> [57], showing the success of this method in solving the questions hard to be clarified by experimental methods. No literature regarding the adsorption or surface reaction of NH<sub>3</sub> on SnO<sub>2</sub> was known until this work.

In next sections, NH<sub>3</sub> sensing results of individual SnO<sub>2</sub> nanowire in dry and humidified SA is given. The details of using DTF to determine the surface chemistry is then presented. By combining these results, a preferred surface reaction routine was proposed. The interference from humidity can also be explained by the atomistic modeling.

## **4.2 NH<sub>3</sub> sensing using individual SnO<sub>2</sub> nanowires**

### **4.2.1 NH<sub>3</sub> sensing in dry SA**

Individual SnO<sub>2</sub> nanowires were contacted by Pt strips in 2-probe configuration. After annealing at 300°C, the measured resistance values usually dropped several folds lying between 5~30MΩ at RT. This is ascribed to the resistance drop in the deposited Pt strips (as discussed in section 3.3) and at the Pt-nanowire contacts. The straight line of IV sweeps (shown in figure 4.1) after annealing indicates the ohmic contact between the nanowire and Pt strips.

The responses of a SnO<sub>2</sub> nanowire sensor to different concentrations (25ppm~200ppm) of NH<sub>3</sub> in dry SA were first measured at several temperatures from 75°C to 300°C. The resistance always decreased after exposure to NH<sub>3</sub>, but the responses at temperatures below 150°C were not

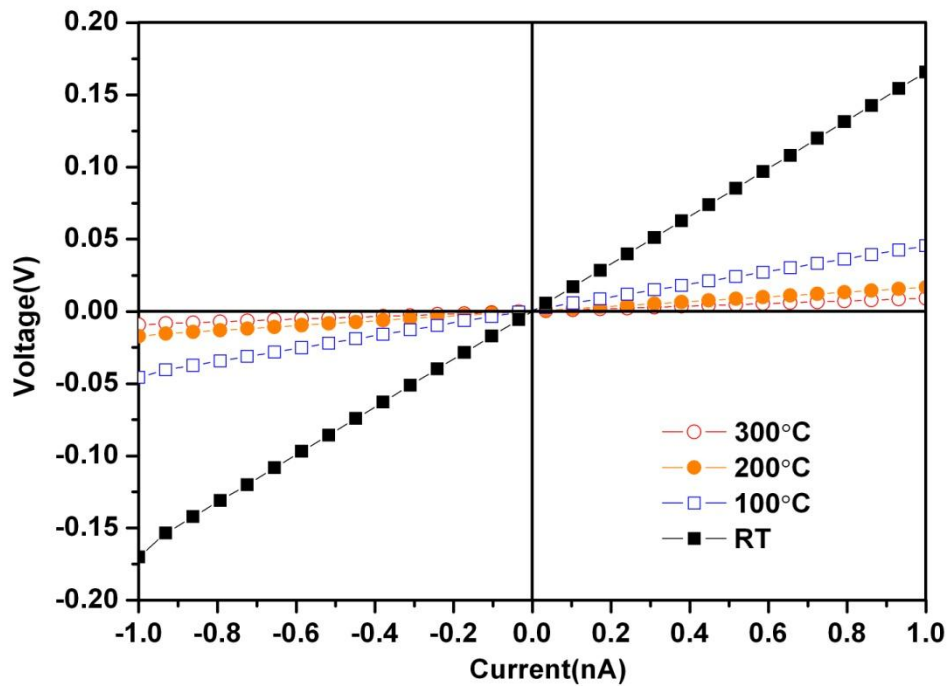


**Figure 4.1** Typical IV curves of a 2-probe contacted SnO<sub>2</sub> nanowire.

only very small but also too slow to be studied further. Figure 4.2 shows the typical real time signal of the sensor resistance to NH<sub>3</sub> at the temperatures between 150°C and 300°C. The temperature dependence of the sensitivity ( $S = R_{SA}/R_{gas}$ ,  $R_{SA}$  and  $R_{gas}$  are the resistance in dry SA and gas mixture, respectively) is shown in figure 4.3. As expected, the sensing mechanism of SnO<sub>2</sub> is a thermally activated process with a maximum response in between 200°C and 250°C. The  $S$  value that ranges from 1.1 to 1.6 is fully comparable to the individual SnO<sub>2</sub> nanowire sensor reported in literature [14]. Temperature also has strong influence on the response ( $t_{res}$ ) and recovery ( $t_{rec}$ ) time (here defined as the time last between the 10 to 90% of  $R$  change). Increasing the temperature has significantly accelerated the resistance modulation. At 150°C, the

resistance was not stabilized at any NH<sub>3</sub> concentrations during 2h's blend interval. At higher temperatures, response to 25ppm NH<sub>3</sub> was still slow, but only a few minutes for higher NH<sub>3</sub> concentrations were needed to reach the stabilization. On the other hand, the recovery time is always much longer than the response time. Even at the quickest 300°C, 18min were needed to recover the resistance baseline from a 50ppm NH<sub>3</sub> pulse.

If we assume  $r$  is the rate of the surface reaction that triggers the resistance change,  $dmol$  represents the infinitesimal molar change of the surface molecules,  $dt$  is the infinitesimal time change,  $dR$  is the infinitesimal resistance change,  $\Delta R$  is the resistance change within the time  $\Delta t$  and  $\Delta t = t_{res}$ , we can write down the following equation:

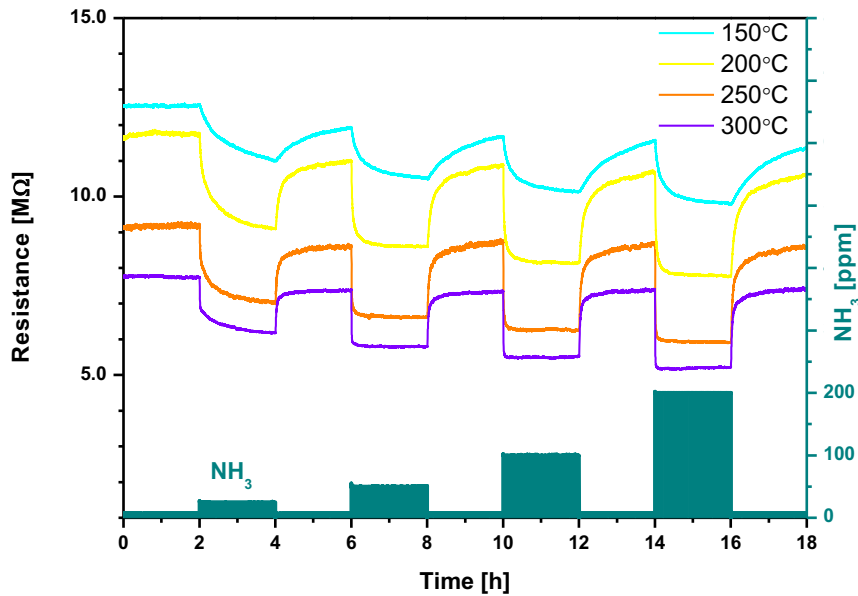


**Figure 4.2** Real time response of a SnO<sub>2</sub> sensor to different NH<sub>3</sub> concentrations.

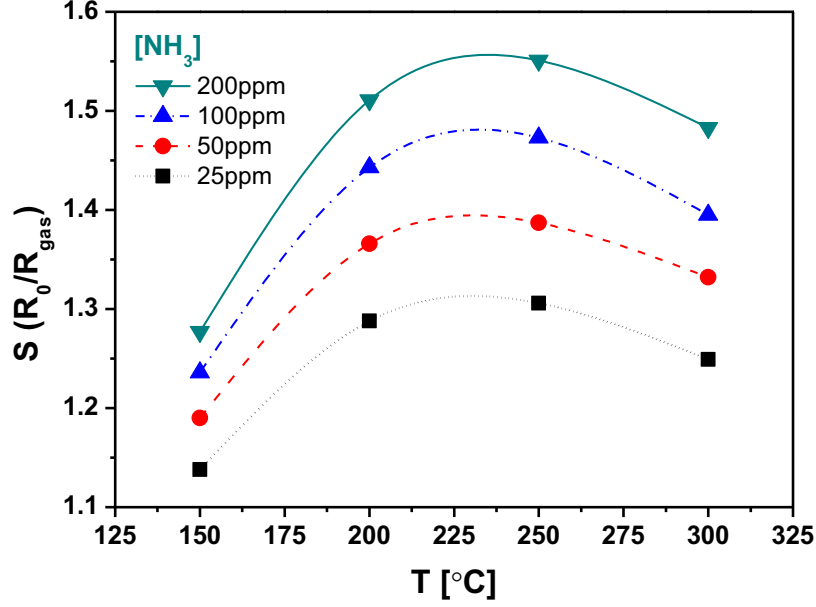


**Figure 4.3** Sensitivity vs. temperature at different concentrations.

$$r = \frac{dmol}{dt} \propto \frac{dR}{dt} \approx \frac{\Delta R}{\Delta t} = \frac{\Delta R}{t_{res}} \quad (4.1)$$

that is,

$$r \propto \frac{\Delta R}{t_{res}} \quad (4.2)$$

and we know that the reaction rate  $r$  is proportional to the rate coefficient  $k$  and the Arrhenius equation gives  $k$  as [60]

$$k = Ae^{-E_a/(k_B T)} \quad (4.3)$$

where  $A$  is a prefactor,  $E_a$  is the activation energy,  $k_B$  is the Boltzmann constant, and  $T$  is the temperature. From equation (4.2) and (4.3), we have



$$t_{res} \propto Ae^{E_a/(k_B T)} \quad (4.4)$$

Fitting the  $t_{res}$  vs.  $1000/T$  data with an exponential function (as shown in figure 4.4), an average  $E_a$  of 0.54eV was obtained. In the next section, this value will help with the interpretation of the results from DFT calculations.

As shown in figure 4.5, the sensing test was extended to lower  $NH_3$  concentrations at 250°C. And the log-log plot of  $S$  vs.  $[NH_3]$  ( $NH_3$  concentration) is given in figure 4.6. The sensitivity of  $SnO_2$  sensor is usually expressed by [61, 62]

$$S \sim \beta * [C]^\alpha \quad (4.5)$$

where  $\beta$  denotes a constant, and  $[C]$  stands for the concentration of the target gas. In practise,  $\alpha$  is a parameter depends on the experimental conditions and the intrinsic properties of the metal oxide, and usually takes values smaller than 1 [63]. Our devices followed the power law reported, with the exponent  $\alpha = 0.07 \pm 0.01$  (Fig. 4.5).

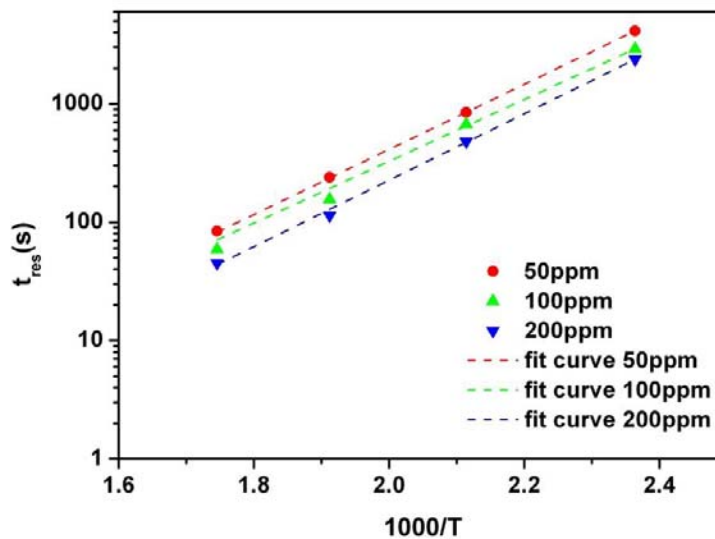


**Figure 4.4**  $t_{res}$  vs.  $1000/T$  and fitted curves.

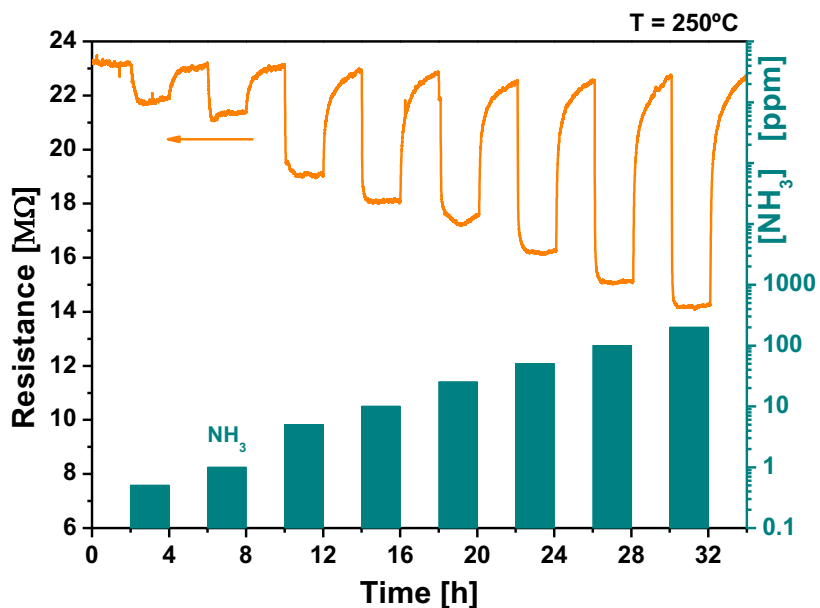


**Figure 4.5** Response to extended  $\text{NH}_3$  concentrations at  $250^{\circ}\text{C}$  (concentration pulses from 0.5 to 200ppm were used).

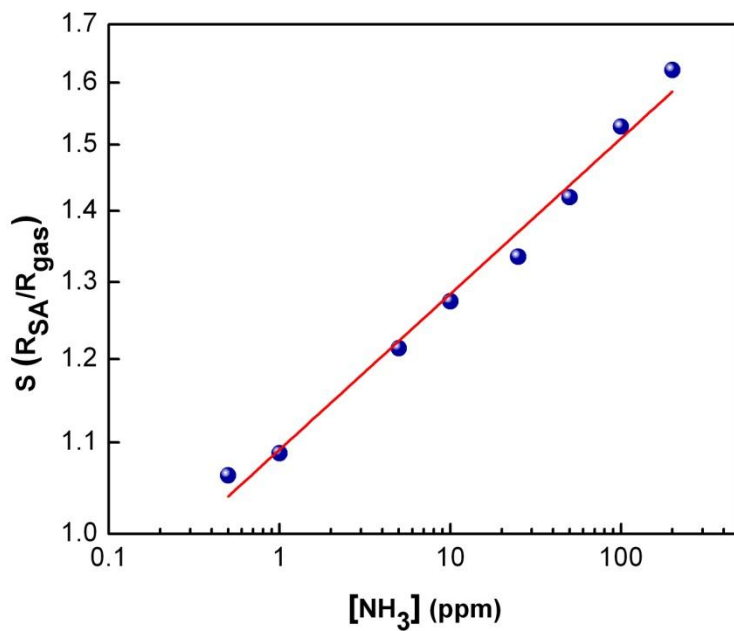


**Figure 4.6**  $S$  vs.  $[\text{NH}_3]$  for the test showing in figure 4.5.

#### 4.2.2 Response to NH<sub>3</sub> in humidified SA

Understanding the role of water in the sensing behaviour of SnO<sub>2</sub> is essential for the evaluation of the full potential of these devices [49]. The interference of moisture on gas sensing has been investigated in some cases [1, 50, 52, 64, 65], and the modelling of water sensing with SnO<sub>2</sub> nanowires has been vaguely described in the past [49]. Nevertheless, to the best of our knowledge, a direct quantification of the cross sensitivity between NH<sub>3</sub> and H<sub>2</sub>O has not been reported before this work. H<sub>2</sub>O sensing by SnO<sub>2</sub> nanowires is a completely reversible process, which temporarily enhances the surface electrical conductivity. The associated electrical resistance changes are usually related to the formation of hydroxyl groups at the nanowire surface [49].

Prior to the NH<sub>3</sub> sensing in humidified SA, the sensors' response to pure humidified SA was examined at different temperatures. As shown in figure 4.7, at three levels of relative humidity (RH) applied (25, 50 and 75%), the stabilized resistance values were almost identical, indicating the SnO<sub>2</sub> surface was already saturated at 25% RH, which was the lowest RH applied. The response and recover processes were found to be faster at higher temperatures (a few minutes at 250°C). By monitoring the RH in the inlet gas pipe, the quick stabilization of resistance toward 25% RH at 250°C showed that the saturation happened at RH<25%. This is an indirect indication of the high affinity of water for the SnO<sub>2</sub> surface and results in its high coverage by water-related products. Overall, the result shows the potential interference of RH on reducing gas sensing like NH<sub>3</sub>.

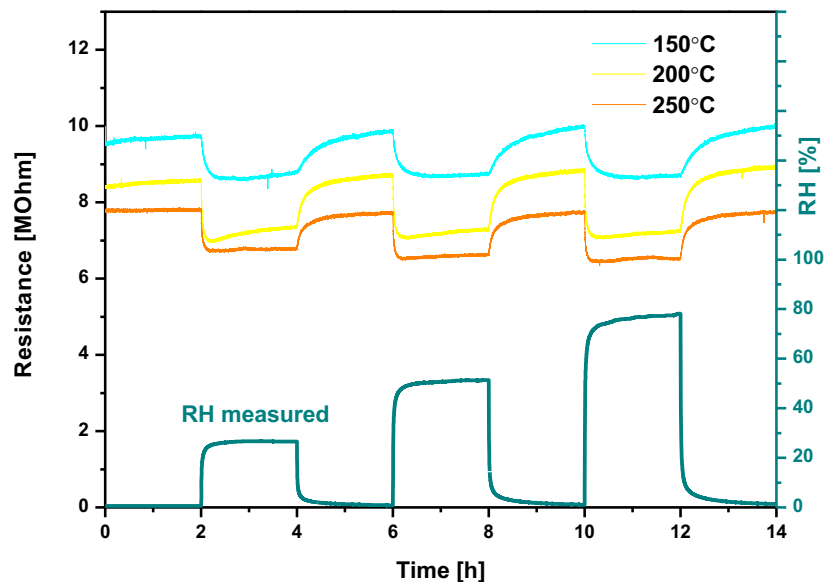


**Figure 4.7** Response of SnO<sub>2</sub> nanowire to different RH levels in SA.

Dosing of NH<sub>3</sub> in humidified SA background further brought down the resistance of the nanowire. Although it appeared fully reversible and had retained the dependence on [NH<sub>3</sub>], the changes were always smaller than in dry SA (see figure 4.8). Therefore, the sensitivity is lower (up to 30%<sup>1</sup>) in humidified SA. Due to the saturation to RH, the initial resistances R<sub>SA</sub> at different RH were often found very close and could not be discriminated. In addition, it is adequate enough to claim that at different RH and same NH<sub>3</sub> levels, the resistance stabilized at the same value, which does not correspond to the simple addition of resistance changes due to RH and NH<sub>3</sub> separately. The coupled effects between H<sub>2</sub>O and NH<sub>3</sub> for a single nanowire sensor reveal a competing mechanism between the two gases which will be evaluated in the next section.

<sup>1</sup> Calculated as  $(S_{dry} - S_{humid})/S_{dry}$

The influence of RH is a serious drawback in real sensing application where fluctuating humidity level in the environment may lead to false NH<sub>3</sub> read outs. For this reason, this effect must be taken into account in the design of real devices. To minimize it, the use of external filter is an effective solution [66, 67].

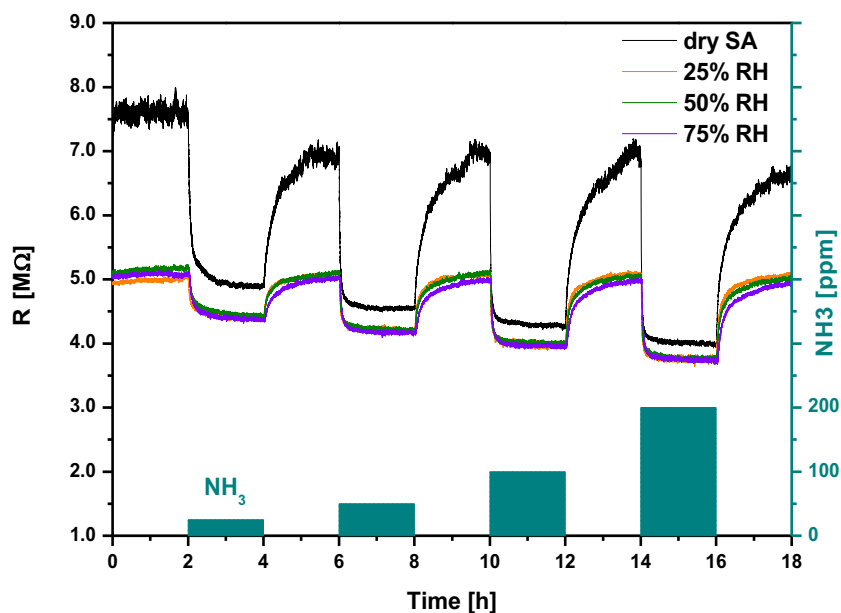


**Figure 4.8** Response of SnO<sub>2</sub> nanowire to NH<sub>3</sub> in different RH levels.

### 4.3 DFT modeling of NH<sub>3</sub> interaction with SnO<sub>2</sub> (110) surface

#### 4.3.1 Adsorption of NH<sub>3</sub> on stoichiometric and reduced surface

The (110) surface of SnO<sub>2</sub> consists of four kinds of atoms: Sn<sub>5c</sub>, Sn<sub>6c</sub>, bridging O<sub>2c</sub> and in-plane O<sub>3c</sub> (Figure 4.9a). Sn<sub>5c</sub> is a Lewis acid site that is able to withdraw electrons from an electron rich atom like nitrogen in the NH<sub>3</sub> molecule. DFT calculation of NH<sub>3</sub> adsorption on other MOX

had shown that the bonding happens between the unsaturated metal atoms and the N of NH<sub>3</sub> [56]. Therefore, the adsorption geometry applied first was the NH<sub>3</sub> adsorption on the Sn<sub>5c</sub> site with the N binding to the Sn<sub>5c</sub> with the Sn<sub>5c</sub>-N bond perpendicular to the surface plane, as shown in figure 4.9b. The obtained  $E_{ads}$  values are listed in table 4.2. After counting for entropy, the 50% coverage (NH<sub>3</sub>/Sn<sub>5c</sub> site) adsorption energy falls in the low end of Redhead desorption energy by TPD [39]. Rotating the NH<sub>3</sub> molecule along the axis of Sn<sub>5c</sub>-N bond made negligible changes in  $E_{ads}$  (<10meV). While adding a second NH<sub>3</sub> on the neighbor Sn<sub>5c</sub> site to imitate the 100% coverage (figure 4.9c) reduced the average  $E_{ads}$  ( $E_{ads} = (E_{tot} - E_{sur} - E_{mol \times 2})/2$ ) to -0.73eV, indicating the lateral interaction between the adsorbed molecules could prevent dense coverage.

**Table 4.2** Calculated adsorption geometries and  $E_{ads}$ .

	adsorption config.	in Figure 4.9	$E_{ads}$ (eV)	bond length (Å)
stoichiometric	1 NH <sub>3</sub> on Sn <sub>5c</sub>	(b)	-1.14	2.32
	2 NH <sub>3</sub> on Sn <sub>5c</sub>	(c)	-0.73	2.35
reduced surface (50% O <sub>2c</sub> vacancy)	1 NH <sub>3</sub> on Sn <sub>5c</sub>	(d)	-0.50	2.40
	1 NH <sub>3</sub> on O <sub>2c</sub> vacancy	(e)	-0.43	2.93
reduced surface (100% O <sub>2c</sub> vacancy)	1 NH <sub>3</sub> on Sn <sub>5c</sub>	(f)	-0.40	2.41
	1 NH <sub>3</sub> on Sn <sub>4c</sub>	(g)	0.13	N/A
surface with O <sub>ads</sub>	1 NH <sub>3</sub>	(h)	-1.58	2.27

Reduced surfaces were created by removing one or two of the bridging O<sub>2c</sub> in the surface slab to form the 50% or 100% planar reduced surface. Two adsorption sites were considered for the 50% planar reduced surface: on top of Sn<sub>5c</sub> (figure 4.9d) and at the bridging O<sub>2c</sub> vacancy (figure 4.9e) with the N positioned at the previous O<sub>2c</sub> location. The  $E_{ads}$  on those two sites are both less

than half of the energy on the Sn<sub>5c</sub> of the stoichiometric surface. On the bridging O<sub>2c</sub> vacancy, the NH<sub>3</sub> molecule moved away from the surface after structure relaxation and the bond length is 2.93Å between the N and those two Sn<sub>5c</sub> atoms (previous Sn<sub>6c</sub>). On the 100% planar reduced surface, the Sn<sub>4c</sub> atom (figure 4.9f) is completely exposed. However, this geometry turned out to be not prone to adsorption as the  $E_{ads}$  is positive (endothermic). The  $E_{ads}$  on the Sn<sub>5c</sub> site (figure 4.9g) is -0.4eV, smaller than that on the 50% reduced. The results here are in contrast to the TPD conclusion [39] of stronger molecular adsorption on the exposed Sn<sub>4c</sub> than on the Sn<sub>5c</sub>, however reasonable for the general view of Sn<sub>4c</sub> to be a weaker acid than Sn<sub>5c</sub>.

#### 4.3.2 NH<sub>3</sub> dissociation and H<sub>2</sub>O formation with the bridging O<sub>2c</sub>

The surface reaction of adsorbed NH<sub>3</sub> has to start with the dehydrogenation. NEB calculation showed that the first step of NH<sub>3</sub> dehydrogenation toward O<sub>2c</sub> can proceed with an energy barrier  $E_b$  of 0.35eV and reaction energy  $E_r$  of 0.25eV. The result of the dehydrogenation was having an O<sub>2c</sub>H group and a NH<sub>2</sub> group on the surface (see figure 4.10). Further dehydrogenation toward the just formed O<sub>2c</sub>H group was not possible because the  $E_r$  is found to be extremely endothermic, 3.66eV.

Assuming the H atom in the just formed O<sub>2c</sub>H can diffuse to a nearby O<sub>2c</sub> site. The second dehydrogenation step from NH<sub>2</sub> will happen with a barrier  $E_b$  of 0.62eV and  $E_r$  of 0.48eV. Again, formation of water molecule (H<sub>2</sub>O<sub>2c</sub>) was found to be not possible due to a large  $E_r$  (see figure 4.11).

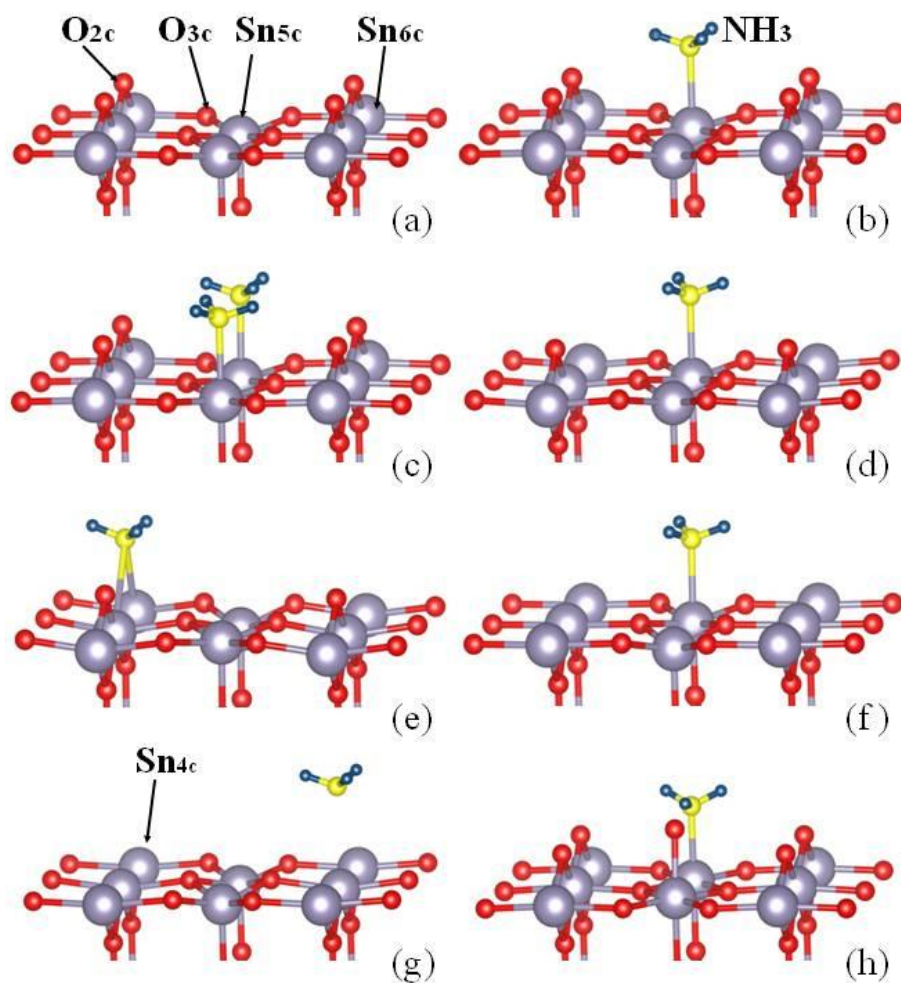


**Figure 4.9** (a) surface atoms of the stoichiometric SnO<sub>2</sub> (110) surface. (b) and (c) NH<sub>3</sub> adsorption geometries on stoichiometric surface. (d)-(h) NH<sub>3</sub> adsorption geometries on reduced and O adsorbed SnO<sub>2</sub>(110) surfaces. Sn: silver, O: red, N: yellow, H: cyan.



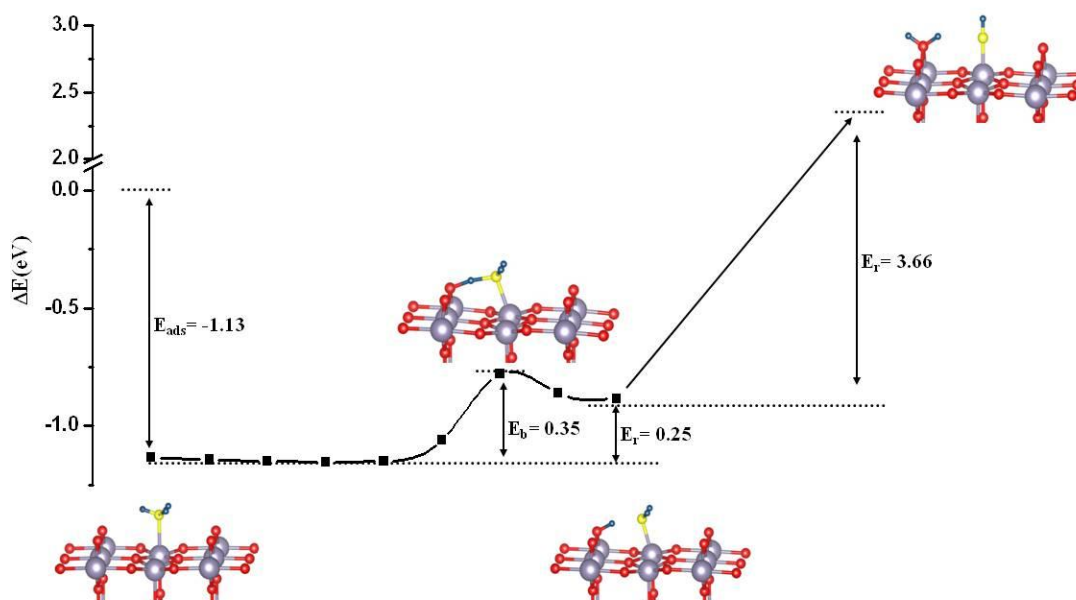


**Figure 4.10** Energy profile and structures of dehydrogenation of the first H from  $\text{NH}_3$  to  $\text{O}_{2c}$ .

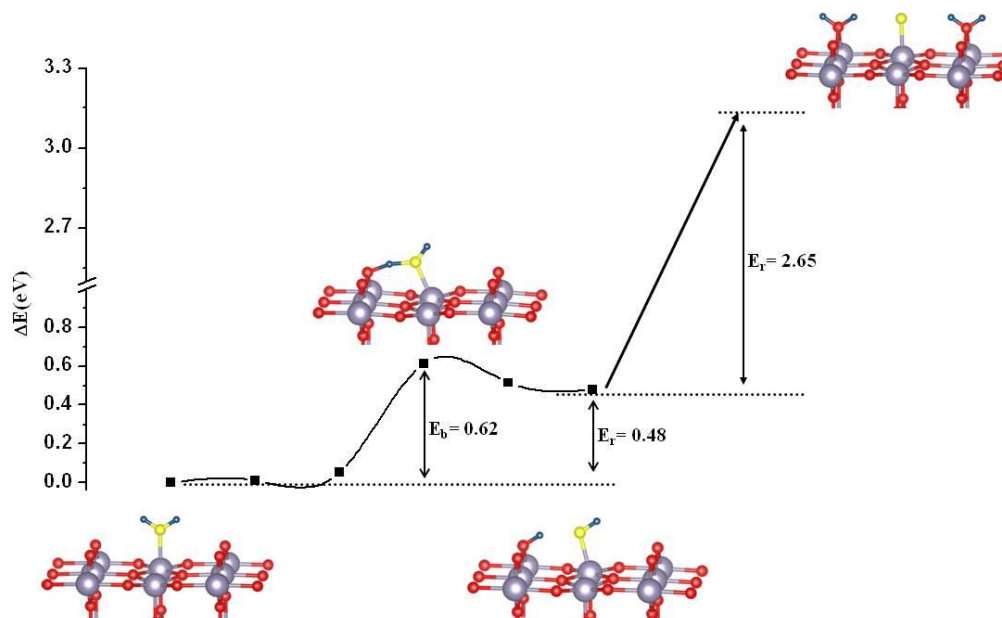


**Figure 4.11** Energy profile and structures of dehydrogenation of a second H from  $\text{NH}_2$  to  $\text{O}_{2c}$ .

The complete dehydrogenation of  $\text{NH}_3$  would not be possible in this 50% surface coverage due to the lack of  $\text{O}_{2c}$  sites available for H. It is however found that the formation of hydrazine,  $\text{N}_2\text{H}_4$  is endothermic by only about 0.70eV if the  $\text{NH}_2$  groups on the surface can overcome a diffusion barrier of 0.75eV. Therefore, we expand our modeling to an artificial  $(4\times 1)$  reconstructed surface slab with the energies obtained from the  $(2\times 1)$  slab. As shown in figure 4.12, the  $E_{ads}$  of 2  $\text{NH}_3$  on  $(4\times 1)$  reconstructed surface simply is the double of the  $E_{ads}$  of  $\text{NH}_3$  on the  $(2\times 1)$  slab and the dehydrogenation of the first H from each  $\text{NH}_3$  is same to previous description. Once the  $\text{N}_2\text{H}_4$  is formed, H abstraction by  $\text{O}_{2c}$  takes place, leading to  $\text{N}_2\text{H}_3$ ,  $\text{N}_2\text{H}_2$  and  $\text{N}_2\text{H}$  with the endothermicity of all these processes being less than 1.3eV. The last step from  $\text{N}_2\text{H}$  to  $\text{N}_2$  is exothermic by about -1eV because the formation of the very stable gas-phase molecule. Desorption of two water molecules ( $\text{H}_2\text{O}_{2c}$ ) takes place endothermically and the reaction is completed by the formation of another water molecule ( $\text{H}_2\text{O}_{2c}$ ) by recombination of two  $\text{O}_{2c}\text{H}$  and further desorption.

### 4.3.3 $\text{NH}_3$ dissociation and $\text{H}_2\text{O}$ formation with the pre-adsorbed $\text{O}_{ads}$

Considering a more realistic reduced  $\text{SnO}_2$  (110) surface with bridging  $\text{O}_{2c}$  vacancies. It has been predicted that  $\text{O}_2$  molecules from the gas phase would adsorbed at the vacancy sites and dissociate to generated O atom onto under-coordinated  $\text{Sn}_{5c}$ , and at the same time recover the  $\text{O}_{2c}$  vacancy [44]. The O atom adsorbed to  $\text{Sn}_{5c}$  will be named  $\text{O}_{ads}$  here. Adsorption of  $\text{O}_2$  molecules onto  $\text{O}_{2c}$  vacancies is found to be exothermic by -0.63eV while the subsequent activation of the  $\text{O}_2$  dissociation step is activated by  $E_b = 1.12\text{eV}$ , and thus, the effective barrier for  $\text{O}_2$  adsorption

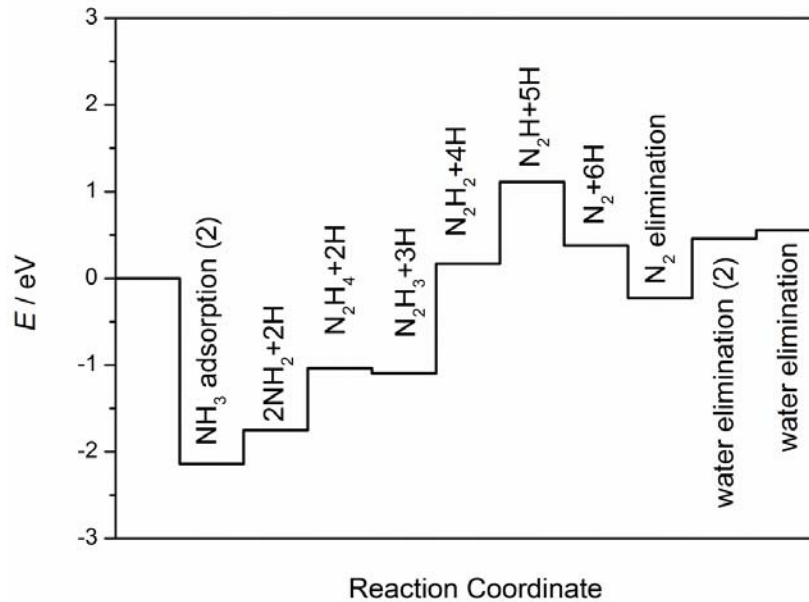


**Figure 4.12** Reaction energy profile for the thermodynamics of all the steps involved in the reaction of ammonia with stoichiometric  $\text{SnO}_2$  (110) surface.

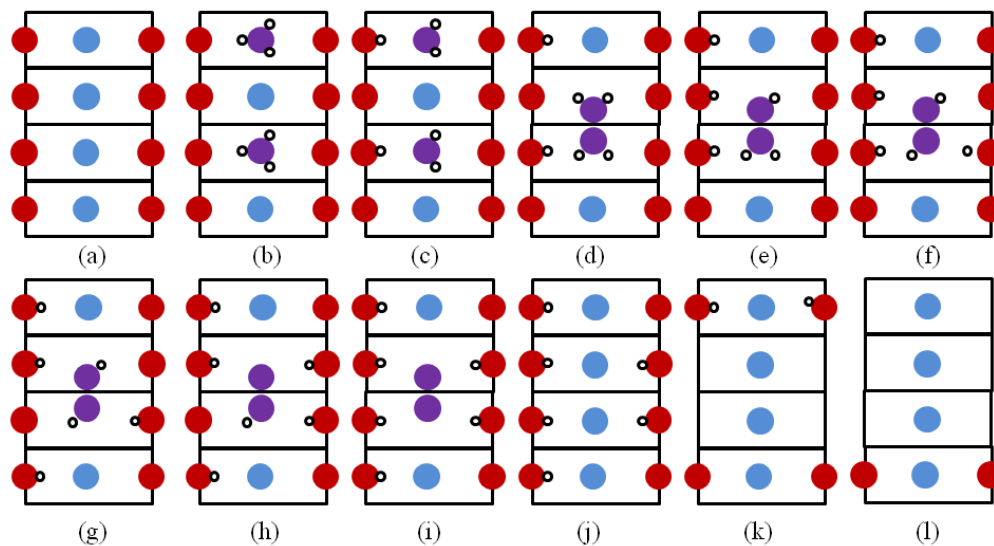


**Figure 4.13** Top view of the schematic representation of interaction steps between  $\text{NH}_3$  molecules and the stoichiometric  $\text{SnO}_2$  (110) surface. Cyan spheres represent  $\text{Sn}_{5c}$  atoms, red  $\text{O}_{2c}$  atoms, white H atoms and purple N.

is 0.49eV. For the structure showing in figure 4.9h, the  $E_{ads}$  of  $\text{NH}_3$  on the remaining  $\text{Sn}_{5c}$  was found to be -1.58eV. It is 0.44eV larger than on the stoichiometric surface. The  $\text{O}_{ads}$  had the bond with  $\text{Sn}_{5c}$  5.3° tilted from the surface normal to the direction of  $\text{NH}_3$  and the distance from the  $\text{O}_{ads}$  to the closest H of  $\text{NH}_3$  is 1.98 Å, indicating the presence of hydrogen bonding.

The dissociation of adsorbed  $\text{NH}_3$  starts with breaking the H-N bond of the above mentioned H atom and forming a hydroxyl group with the  $\text{O}_{ads}$  (see figure 4.14). This step is slightly endothermic with the  $E_b = 0.29\text{eV}$  and  $E_r = 0.03\text{eV}$ . The formed intermediate states noted as  $\text{NH}_2+\text{HO}_{ads}$  can have its geometry changed by rotating along the N- $\text{Sn}_{5c}$  and O- $\text{Sn}_{5c}$  bonds to a more stable structure ( $\Delta E = -0.18\text{eV}$ )  $\text{NH}_2+\text{HO}_{ads}\text{II}$  with the H in  $\text{HO}_{ads}$  pointing to a neighbor

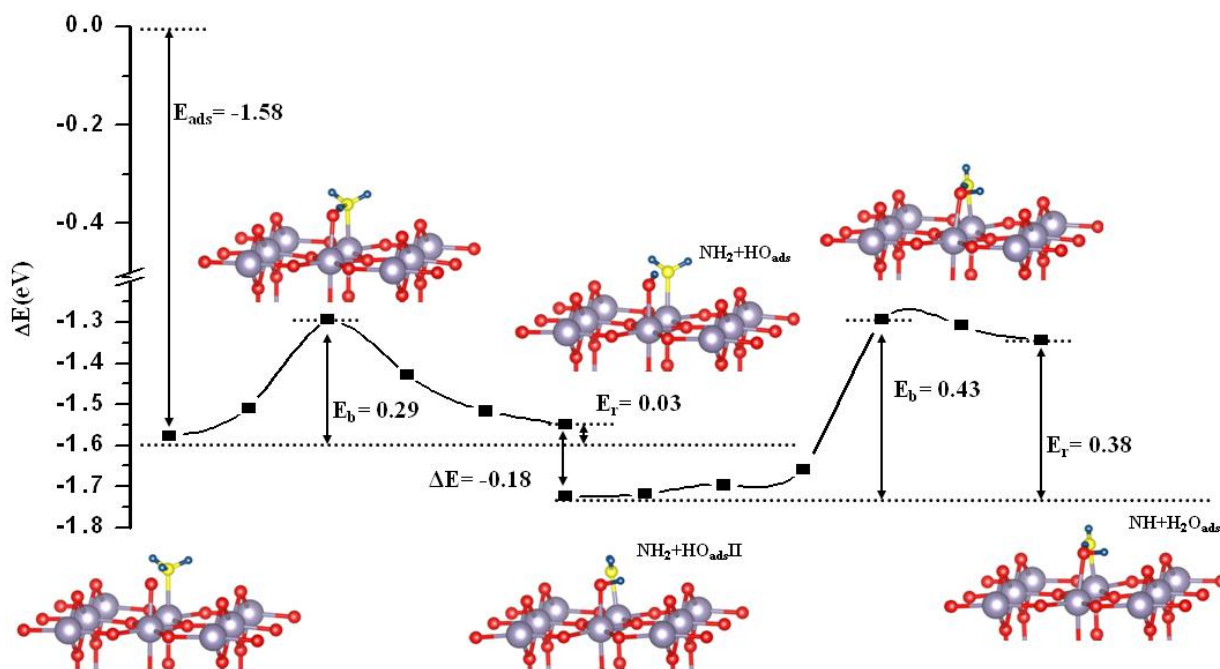


**Figure 4.14** Energy profile and structures of dehydrogenation with the  $\text{O}_{ads}$ .

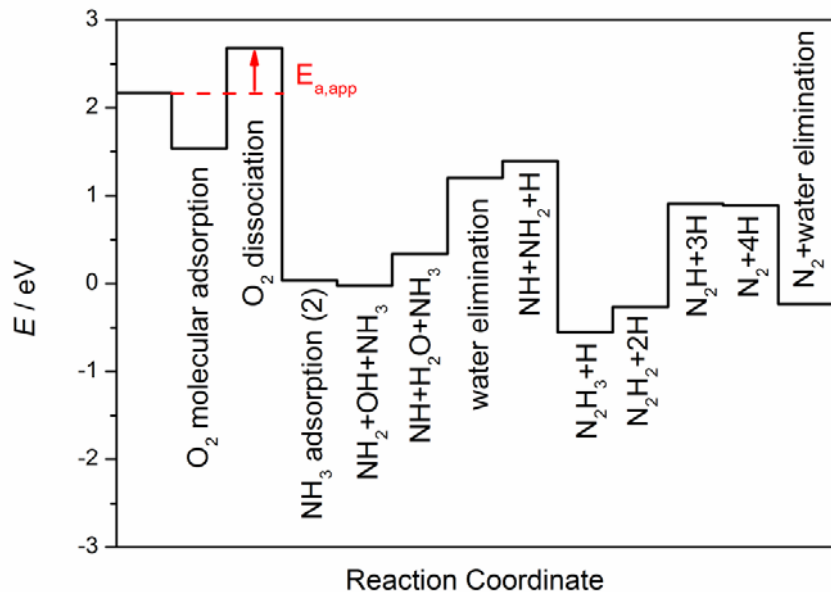


**Figure 4.15** Reaction energy profile for the thermodynamics of all the steps in the reaction of ammonia with  $O_{\text{ads}}$  and  $\text{SnO}_2(110)$  surface.

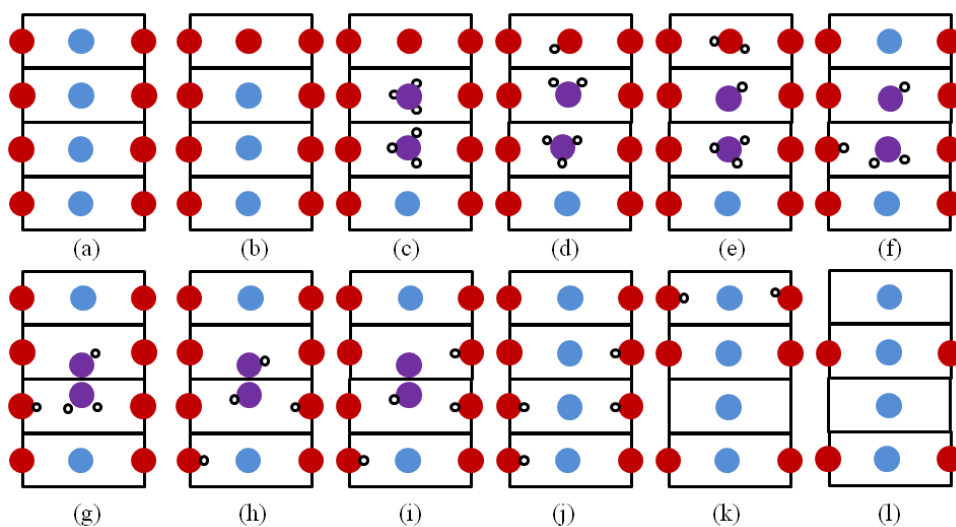


**Figure 4.16** Top view of the schematic representation of interaction steps between  $\text{NH}_3$  molecules and the  $O_{\text{ads}}$  adsorbed  $\text{SnO}_2(110)$  surface. Cyan spheres represent  $\text{Sn}_{5c}$  atoms, red  $O_{2c}$  atoms, white H atoms and purple N.

$O_{2c}$ , from there, the next H dissociation can happen with a barrier  $E_b = 0.43\text{eV}$  and a total reaction energy  $E_r = 0.38\text{eV}$ . The produced structure  $NH+H_2O_{ads}$  can have the  $H_2O_{ads}$  desorbed from surface with the desorption energy  $E_{des}$  of  $1.2\text{eV}$ . The resulting NH moieties on the surface can combine to other  $NH_x$  fragments since diffusions of both  $NH_2$  and NH are low energy demanding ( $0.75$  and  $0.45\text{eV}$ ) elementary steps. Condensation to  $HNNH_2$  intermediates is exothermic by almost  $2\text{eV}$ . The energy profile of following steps were modeled in the  $(4\times 1)$  super cell and plotted in figure 4.15. The elimination of the resting H atoms from  $HNNH_2$  is possible as the processes are endothermic by  $0.29$  and  $1.18\text{eV}$ . Water formation at the lattice position sees higher energy. Finally, the  $N_2$  and  $H_2O_{2c}$  will be desorbed from the surface.

As we have seen, the  $O_{ads}$  on the reduced surface are more likely to attract H from  $NH_3$  comparing to the  $O_{2c}$ . The evolution of  $H_2O_{ads}$  and  $H_2O_{2c}$  into gas phase is considered the ultimate responsible for the resistance reduction upon exposure to  $NH_3$ . The  $O_{ads}$  formation step sees the highest point in figure 4.15 and the effective barrier ( $0.49\text{eV}$ ) of  $O_{ads}$  formation on the reduced surface is found to be very close to the experimental  $E_a$  ( $0.54\text{eV}$ ) determined by the  $t_{res}$  of the nanowire sensor in section 4.2.1. It is therefore concluded that the  $O_{ads}$  formation step is the rate determining step of the sensor response. And the reduced surface with  $O_{ads}$  is the system that more accurately representing the sensor surface.

#### 4.3.4 $H_2O$ adsorption and its influence on $NH_3$ sensing

Depending on  $H_2O$  adsorption geometries, the adsorption energy of a  $H_2O$  molecule ( $0.5\text{monolayer}$  coverage) on the  $Sn_{5c}$  of the stoichiometric  $SnO_2(110)$  surface is found to ranges from  $-0.45$  to  $-0.87\text{eV}$ . As shown in figure 4.17, the structure with largest molecular  $E_{ads}$  is

however an unstable state which easily loss one H atom to the  $O_{2c}$  and gain another 0.3eV energy. Nevertheless, from the experience with  $NH_3$ , it can be expected that the dissociation can routinely happen with the  $O_{ads}$  as well.

Knowing the fact that typical water concentration in humid environments (in the percentage range) are exceedingly high compared to ammonia levels tested (hundreds of ppm), resulting in preferential adsorption of water by pressure effects,  $NH_3$  response-blocking by moisture can be interpreted from two directions: i) the competition for surface adsorption site between O,  $NH_3$  and  $H_2O$  hinders the formation of surface depletion layer and reduces the chance of surface reactions associated with  $NH_3$ ; ii) being one of the products of the surface reaction that cause gas sensing effect, the presence of water in the gas-phase (excess of product molecules) might push the equilibrium of  $N_2$  formation towards reactants.

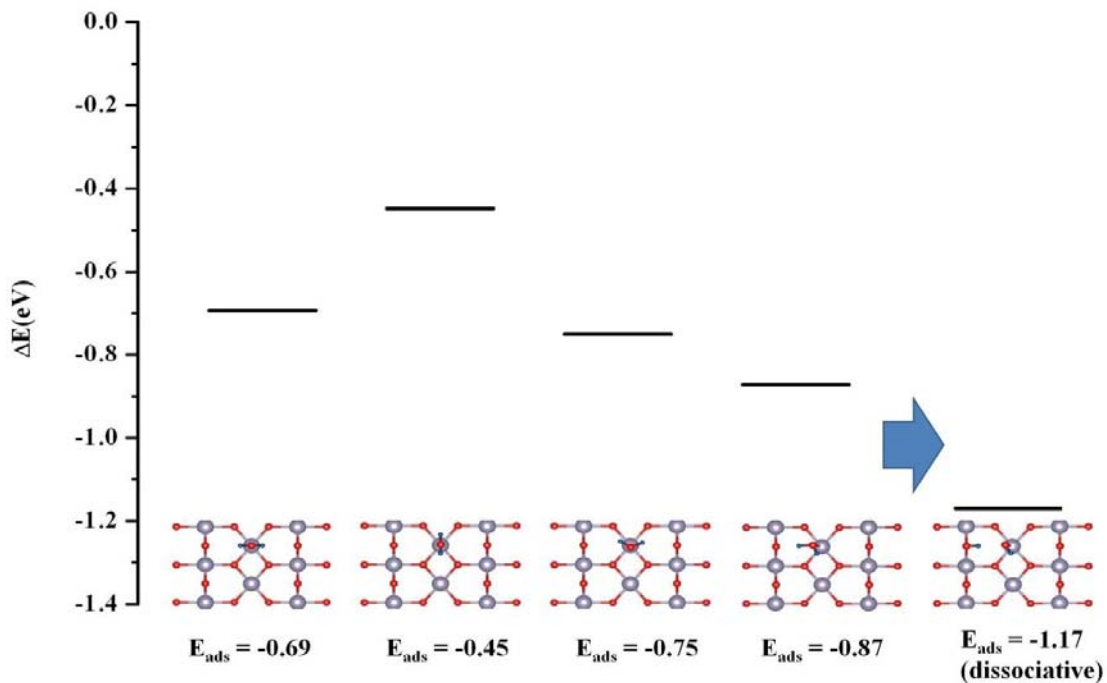


**Figure 4.17**  $E_{ads}$  and structures of  $H_2O$  adsorption on  $SnO_2$  (110) surface.

## 4.4 Conclusions

The chemical-to-electrical transduction mechanisms between  $\text{NH}_3$  molecules and  $\text{SnO}_2$  (110) were examined by DFT and confronted to experimental results obtained with individual nanowire devices.  $\text{NH}_3$  undergoes a dehydrogenation process onto the metal oxide surface with  $\text{N}_2$  and  $\text{H}_2\text{O}$  as the main resulting products, which is not solely physically but also chemically in nature. Under realistic working conditions, adsorbed non-lattice oxygen ( $\text{O}_{\text{ads}}$ ) onto the reduced surface plays a determinant role to complete the  $\text{NH}_3$  sensing pathway in  $\text{SnO}_2$ . The activation energy for the whole process follows the activation of oxygen on the surface. In addition, the competition between  $\text{NH}_3$  molecules and water for the same adsorption sites,  $\text{Sn}_{5\text{c}}$ , results in a partial suppression of the  $\text{NH}_3$  signal in humid conditions and it is easily explained by thermodynamic and concentration arguments. This undesired effect, which is determined by the intrinsic characteristics of  $\text{SnO}_2$  (110) surface, compromises the full potential of  $\text{SnO}_2$  based devices as efficient ammonia sensors.



## References

- [1] N. Bârsan, U. Weimar, Understanding the Fundamental Principles of Metal Oxide based Gas Sensors; the Example of CO Sensing with SnO<sub>2</sub> Sensors in the Presence of Humidity, *J. Phys.: Condens. Matter* 15 (2003) R813–R839.
- [2] S. Ahlers, G. Müller, T. Doll, A rate equation approach to the gas sensitivity of thin film metal oxide materials, *Sensors and Actuators B: Chemical*, 107 (2005) 587-599.
- [3] N. Barsan, U. Weimar, Conduction Model of Metal Oxide Gas Sensors, *J. Electroceram.*, 7 (2001) 143–167.
- [4] U.S.D.o.H.a.H. Services, Occupational Safety and Health Guideline for Ammonia, in, 1992.
- [5] J.T. AREDDY, Deadly Fire Renews China Work-Safety Fears in: *The Wall Street Journal*, online, 2013.
- [6] C.G.a.C. MacLaggan, Ammonium nitrate stores exploded at Texas plant: state agency, in: *Reuters US edition*, online, 2013.
- [7] C.N. Xu, N. Miura, Y. Ishida, K. Matsuda, N. Yamazoe, Selective detection of NH<sub>3</sub> over NO in combustion exhausts by using Au and MoO<sub>3</sub> doubly promoted WO<sub>3</sub> element, *Sensors and actuators B*, 65 (2000) 164–165.
- [8] B. Timmer, W. Olthuis, A.V.D. Berg, Ammonia sensors and their application---a review, *Sens. Actuators B Chem.*, 107 (2005) 666-677.
- [9] I. Nova, C. Ciardelli, E. Tronconi, D. Chatterjee, B. Bandl-Konrad, NH<sub>3</sub>–NO/NO<sub>2</sub> chemistry over V-based catalysts and its role in the mechanism of the Fast SCR reaction, *Catalysis Today*, 114 (2006) 3-12.
- [10] C. Imawan, F. Solzbacher, H. Steffes, E. Obermeier, Gas-sensing characteristics of modified-MoO<sub>3</sub> thin films using Ti-overlayers for NH<sub>3</sub> gas sensors, *Sensors and Actuators B: Chemical*, 64 (2000) 193–197.
- [11] A. Lassesson, M. Schulze, J.v. lith, S.A. Brown, Tin oxide nanocluster hydrogen and ammonia sensors, *Nanotechnology*, 19 (2008) 015502.
- [12] R. Triantafyllopoulou, X. Illa, O. Casals, S. Chatzandroulis, C. Tsamis, A. Romano-Rodriguez, J.R. Morante, Nanostructured oxides on porous silicon microhotplates for NH<sub>3</sub> sensing, *Microelectronic Engineering*, 85 (2007) 1116–1119.
- [13] Y.D. Wang, Q.Y. Mu, G.F. Wang, Z.L. Zhou, Sensing Characterization to NH<sub>3</sub> of nanocrystalline Sb-doped SnO<sub>2</sub> synthesized by a nonaqueous sol-gel route, *Sensors and actuators B*, 145 (2010) 847–853.
- [14] D.C. Meier, S. Semancik, B. Button, E. Strelcov, A. Kolmakov, Coupling Nanowire Chemiresistors with MEMS Microhotplate Gas Sensing Platforms, *Appl. Phys. Lett.*, 91 (2007) 063118.

- [15] L.V. Thong, N.D. Hoa, D.T.T. Le, D.T. Viet, P.D. Tam, A.-T. Le, N.V. Hieu, On-chip fabrication of SnO<sub>2</sub>-nanowire gas sensor: The effect of growth time on sensor performance, *Sensors and Actuators B: Chemical*, 146 (2010) 361–367.
- [16] A. Forleo, L. Francioso, S. Capone, F. Casino, P. Siciliano, O.K. Tan, H. Hui, Fabrication at wafer level of miniaturized gas sensors based on SnO<sub>2</sub> nanorods deposited by PECVD and gas sensing characteristics, *Sensors and Actuators B: Chemical*, 154 (2011) 283-287.
- [17] Q. Qi, T. Zhang, L. Liu, X.J. Zheng, G.Y. Lu, Improved NH<sub>3</sub>, C<sub>2</sub>H<sub>5</sub>OH, and CH<sub>3</sub>COCH<sub>3</sub> sensing properties of SnO<sub>2</sub> nanofibers by adding block copolymer P123, *Sensors and actuators B*, 141 (2009) 174–178.
- [18] G.X. Wang, e. al, Synthesis and high gas sensitivity of tin oxide nanotubes, *Sensors and Actuators B*, (2008) 313–317.
- [19] Y.M. Zhao, Y.Q. Zhu, Room temperature ammonia sensing properties of W<sub>18</sub>O<sub>49</sub> nanowires, *Sensors and Actuators B: Chemical*, 137 (2009) 27–31.
- [20] A. Ponzoni, E. Comini, G. Sberveglieri, e. al, Untrasensitive and highly selective gas sensors using three-dimensional tungsten oxide nanowire networks, *Applied Physics Letters*, (2006) 203101.
- [21] S.J. Chang, e. al, High sensitivity of a ZnO nanowire-based ammonia gas sensor with Pt nanoparticles, *Nano Communication Networks*, (2010).
- [22] J.X. Wang, X.W. Sun, Y. Yang, H. Huang, Y.C. Lee, O.K. Tan, L. Vayssieres, Hydrothermally grown oriented ZnO nanorod arrays for gas sensing applications, *Nanotechnology*, 17 (2006) 4995–4998.
- [23] O. Lupan, V.V. Ursaki, G. Chai, L. Chow, G.A. Emelchenko, I.M. Tiginyanu, A.N. Gruzintsev, A.N. Redkin, Selective hydrogen gas nanosensor using individual ZnO nanowire with fast response at room temperature, *Sensors and Actuators B: Chemical*, 144 (2010) 56-66.
- [24] J.Y. Liu, e. al, Novel single crystalline hierarchical structured ZnO nanorods fabricated via a wet chemical route: combined high gas sensing performance with enhanced optical properties, *Crystal Growth& Design*, 9 (2009) 1716–1722.
- [25] B. Karunagaran, e. al., TiO<sub>2</sub> thin film gas sensor for monitoring ammonia, *Materials characterization*, 58 (2007).
- [26] C. Li, e. al, Surface Treatment and Doping Dependence of In<sub>2</sub>O<sub>3</sub> Nanowires as Ammonia Sensors, *Journal of Physical Chemistry B*, (2003) 12451–12455.
- [27] Z. Liu, T. Yamazaki, Y. Shen, T. Kikuta, N. Nakatani, T. Kawabata, Room temperature gas sensing of p-type TeO<sub>2</sub> nanowires, *Applied Physics Letters*, 90 (2007) 173119-173113.
- [28] K.-Y. Dong, J. Choi, Y.D. Lee, B.H. Kang, Y.-Y. Yu, H.H. Choi, B.-K. Ju, Detection of a CO and NH<sub>3</sub> gas mixture using carboxylic acid-functionalized single-walled carbon nanotubes, *Nanoscale Research Letters*, 8 (2013) 12.

- [29] L. Zhang, F. Meng, et al, A novel ammonia sensor based on high density, small diameter polypyrrole nanowire arrays, *Sensors and actuators B*, (2009) 204–209.
- [30] S.C. Hernandez, D. Chaudhuri, W. Chen, N.V. Myung, A. Mulchandani, Single Polypyrrole Nanowire Ammonia Gas Sensor, *Electroanalysis*, 19 (2007) 2125-2130.
- [31] J. Wang, S. Chan, R.R. Carlson, Y. Luo, G. Ge, R.S. Ries, J.R. Heath, H.-R. Tseng, Electrochemically Fabricated Polyaniline Nanoframework Electrode Junctions that Function as Resistive Sensors, *Nano Letters*, 4 (2004) 1693-1697.
- [32] H. Liu, J. Kameoka, D.A. Czaplewski, H.G. Craighead, Polymeric Nanowire Chemical Sensor, *Nano Letters*, 4 (2004) 671-675.
- [33] M. Batzill, U. Diebold, The surface and materials science of tin oxide, *Prog. Surf. Sci*, 79 (2005) 47-154.
- [34] N.V. Hieu, V.V. Quang, N.D. Hoa, D. Kim, Preparing Large-scale WO<sub>3</sub> Nanowire like Structure for High Sensitivity NH<sub>3</sub> Gas Sensor Through a Simple Route, *Curr. Appl. Phys.*, 11 (2011) 657–661.
- [35] I. Jimenez, M.A. Centeno, R. Scotti, F. Morazzoni, A. cornet, NH<sub>3</sub> Interaction with Catalytically Modified Nano WO<sub>3</sub> Poders for Gas Sensing Applications, *J. Electro. Chem. Soc.*, 150 (2003) 72–80.
- [36] Y. Shimizu, T. Okamoto, Y. Takao, M. Egashira, Desorption Behavior of Ammonia from TiO<sub>2</sub> based Specimens -Ammonia Sensing Mechanism of Double Layer Sensors with TiO<sub>2</sub> based Catalyst Layers, *J. Mol. Catal. A: Chem.*, 155 (2000) 183–191.
- [37] J. Oviedo, M.J. Gillan, The Energetics and Structure of Oxygen Vacancies on the SnO<sub>2</sub>(110) Surface, *Surf. Sci.*, 467 (2000) 35–48.
- [38] D.F. Cox, T.B. Fryberger, S. Semancik, Oxygen Vacancies and Defect Electronic States on the SnO<sub>2</sub>(110)-1×1 Surface, *Phys. Rev. B*, 38 (1988) 2072–2083.
- [39] M.W. Abee, D.F. Cox, NH<sub>3</sub> Chemisorption on Stoichiometric and Oxygen-deficient SnO<sub>2</sub>(110) Surfaces, *Surf. Sci.*, 520 (2002) 65–77.
- [40] M. Batzill, U. Diebold, The Surface and Materials Science of Tin Oxide, *Prog. Surf. Sci.* , 79 (2005) 47–154.
- [41] S. Lenaerts, J. Roggen, G. Maes, FT-IR Characterization of Tin Dioxide Gas Sensor Materials under Working Conditions, *Spectrochim. Acta, Part A*, 51 (1995) 883–894.
- [42] S.C. Chang, Oxygen Chemisorption on Tin Oxide: Correlation between Electrical Conductivity and EPR Measurements, *J. Vac. Sci. Technol*, 17 (1979) 366–369.
- [43] T. Sahn, A. Gurlo, N. Barsan, U. Weimar, Basics of oxygen and SnO<sub>2</sub> interaction: work function change and conductivity measurements, *Sens. Actuators: B*, 118 (2006).

- [44] J. Oviedo, M.J. Gillan, First-principles study of the interaction of oxygen with the SnO<sub>2</sub> (110) surface, *Surf. Sci.*, (2001) 221–236.
- [45] W. Wei, Y. Dai, B.B. Huang, Role of Cu Doping in SnO<sub>2</sub> Sensing Properties Toward H<sub>2</sub>S, *J. Phys. Chem. C*, 115 (2011) 18597–18602.
- [46] M. Habgood, N. Harrison, An *ab initio* study of oxygen adsorption on tin dioxide, *Surface science*, 602 (2008) 1072–1079.
- [47] D. Koziej, N. Barsan, U. Weimar, J. Szuber, e. al., Water- oxygen interplay on tin dioxide surface: implication on gas sensing, *Chemical Physics Letters*, (2005) 321-323.
- [48] J.-M. Ducéré, A. Hemeryck, A. Estève, M.D. Rouhani, G. Landa, P. Ménini, C. Tropis, A. Maisonnat, P. Fau, B. Chaudret, A computational chemist approach to gas sensors: Modeling the response of SnO<sub>2</sub> to CO, O<sub>2</sub>, and H<sub>2</sub>O Gases, *Journal of Computational Chemistry*, 33 (2012) 247-258.
- [49] F.H. Ramirez, S. Barth, A. Taron, O. Casals, E. Pellicer, J. Rodriguez, A.R. Rodriguez, J.R. Morante, S. Mathur, Water Vapor Detection with Individual Tin Oxide Nanowires, *Nanotechnology*, 18 (2007) 424016.
- [50] N. Bârsan, R. Ionescu, The Mechanism of the Interaction between CO and an SnO<sub>2</sub> Surface: the Role of Water Vapour, *Sens. Actuators B Chem.*, 12 (1993) 71–75.
- [51] M.M. Franco, G. Pacchioni, CO adsorption on SnO<sub>2</sub>(110): cluster and periodic *ab initio* calculations, *Surface science*, (2000) 54–66.
- [52] W. Schmid, N. Bârsan, U. Weimar, Sensing of Hydrocarbons and CO in Low Oxygen Conditions with Tin Dioxide Sensors: Possible Conversion Paths, *Sens. Actuators B Chem.*, 103 (2004) 362–368.
- [53] V.V. Kovalenko, A.A. Zhukova, M.N. Rumyantseva, A.M. Gaskov, V.V. Yushchenko, I.I. Ivanova, T. Pagnier, Surface chemistry of nanocrystalline SnO<sub>2</sub>: Effect of thermal treatment and additives, *Sensors and Actuators B: Chemical*, 126 (2007) 52-55.
- [54] C. Guimon, A. Gervasini, A. Auroux, XPS Study of the Adsorption of SO<sub>2</sub> and NH<sub>3</sub> over Supported Tin Dioxide Catalysts Used in de-NO<sub>x</sub> Catalytic Reaction, *The Journal of Physical Chemistry B*, 105 (2001) 10316–10325.
- [55] R.M. Yuan, G. Fu, X. Xu, H.L. Wan, Mechanisms for Selective Catalytic Oxidation of Ammonia over Vanadium Oxides, *J. Phys. Chem. C*, (2011) 21218–21229.
- [56] D.J. Cheng, J.H. Lan, D.P. Cao, W.C. Wang, Adsorption and Dissociation of Ammonia on Clean and Metal-covered TiO<sub>2</sub> Rutile (110) Surface: A Comparative DFT Study, *Appl. Catal., B: Environ.*, 106 (2011) 510–519.
- [57] J. Perez-Ramirez, N. Lopez, E.V. Kondratenko, Pressure and Materials Effects on the Selectivity of RuO<sub>2</sub> in NH<sub>3</sub> Oxidation, *J. Phys. Chem. C*, 114 (2010) 16660–16668.

- [58] I. Onal, S. Soyer, S. Senkan, Adsorption of water and ammonia on TiO<sub>2</sub>-anatase cluster models, Surf. Sci., (2006) 2457–2469.
- [59] Q.Z. Yuan, Y.P. Zhao, L.M. Li, T.H. Wang, *Ab Initio* Study of ZnO Based Gas Sensing Mechanisms: Surface Reconstruction and Charge Transfer, J. Phys. Chem. C, (2009) 6107–6113.
- [60] D.A. McQuarrie, J.D. Simon, Physical Chemistry: A Molecular Approach, University Science Books, 1997.
- [61] G. Sakai, N. Matsunaga, K. Shimano, N. Yamazoe, Theory of gas-diffusion controlled sensitivity for thin film semiconductor gas sensor, Sens. Actuators B Chem., 80 (2001) 125–131.
- [62] N. Yamazoe, K. Shimano, Theory of power laws for semiconductor gas sensors, Sens. Actuators B Chem., 128 (2008) 566-573.
- [63] L.V. Thong, L.T.N. Loan, N. Van Hieu, Comparative Study of Gas Sensor Performance of SnO<sub>2</sub> Nanowires and their Hierarchical Nanostructures, Sens. Actuators B Chem., 150 (2010) 112-119.
- [64] W. Schmid, N. Bársan, U. Weimar, Sensing of Hydrocarbons with Tin Oxide Sensors: Possible Reaction Path as Revealed by Consumption Measurements, Sens. Actuators B Chem., 89 (2003) 232–236.
- [65] R. Ionescu, A. Vancu, C. Moise, A. Tomescu, Role of Water Vapour in the Interaction of SnO<sub>2</sub> Gas Sensors with CO and CH<sub>4</sub>, Sens. Actuators B Chem., 61 (1999) 39–42.
- [66] D.K. Schierbaum, Surface Processes in the Detection of Reducing Gases with SnO<sub>2</sub>-based Devices, Sens. Actuators, 18 (1989) 71–113.
- [67] N. Barsan, M. Schweizer-Berberich, W. Göpel, Fundamental and Practical Aspects in the Design of Nanoscaled SnO<sub>2</sub> Gas Sensors: a Status Report, Fresenius J. Anal. Chem., 365 (1999) 287–304.

## **5. H<sub>2</sub>S sensing with SnO<sub>2</sub> nanowires and CuO@SnO<sub>2</sub> nanoheterostructure**

Hydrogen sulphide (H<sub>2</sub>S) is an extremely dangerous pollutant even in very low concentration. CuO decorated SnO nanowires (CuO@SnO<sub>2</sub> heterostructure) were evaluated as selective H<sub>2</sub>S sensors and the working principle behind their good performance was qualitatively modelled. It was concluded that the sensing mechanism is dissimilar to standard redox reactions that are typical of simple MOX sensors, but can be ascribed to the sulfurization of CuO and the consequent modulation of the p-n junctions at the CuO-SnO<sub>2</sub> interface. Experimental data showed that these H<sub>2</sub>S sensors suit well for alarm applications with extremely high selectivity and sensitivity to this gas for concentrations between 1 ppm and 10 ppm.

### **5.1 Introduction**

Hydrogen sulphide (H<sub>2</sub>S) is a colourless, flammable and toxic gas with an offensive odour of rotten eggs [1]. Naturally, it is produced from the anaerobic decomposition of animal or plant waste and contained in the natural gas, which is also a major source of H<sub>2</sub>S. In the chemical industry, sulphur containing compounds need to be removed from oil through the hydrodesulphurization processes that also generate H<sub>2</sub>S as a product. While large amount of H<sub>2</sub>S is being used in chemical production and metal treatment, very low level (<20ppm) of exposure can cause discomfort to Humans. It soon becomes life threaten at concentration larger than 100ppm, and a few breaths at around 500ppm is simply lethal [2]. Occupational exposure limit

has been set to between 5 to 20 ppm for 8-h time weighted average (TWA) in US [3], UK [4] and Canada [5], making the real time monitoring of this pollutant a critical issue.

MOXs have shown outstanding sensing properties to different chemical species with simple and cost effective device configurations [6, 7]. Nevertheless, a major drawback of this technology is the lack of selectivity among the gases of similar redox potentials, which is a measure of the electronegativity of the molecules. Taking the reducing gases  $\text{NH}_3$  and  $\text{H}_2\text{S}$  for example, they both cause the n-type MOX to decrease the resistance therefore making it impossible to tell one from the other. Application of MOX as sensing material is therefore hindered and the search of new methods for the detection of  $\text{H}_2\text{S}$  has attracted a huge interest within the past years [8].

Heterostructures of the MOX with noble metal or other metal oxides [9-11] has been proven to be an effective way to improve the selectivity by enhancing the response to a specific gas and keeping others unchanged. For example, Pt or Pd doping have been used to enhance the sensing of CO and  $\text{H}_2$  [6]. In turn,  $\text{SnO}_2$  mixed or coated with CuO has been reported to be a robust material for the sensing of  $\text{H}_2\text{S}$  and the sensing response readily achieves several orders of magnitude [12-16]. It is usually explained by two different but complementary contributions: i) the particular interaction of CuO and  $\text{H}_2\text{S}$ ; ii) the intrinsic properties of the CuO- $\text{SnO}_2$  interface.

This Chapter writes about p-CuO (particle)/n- $\text{SnO}_2$  (nanowire) heterostructured devices and their application as  $\text{H}_2\text{S}$  sensors. The high sensitivity and selectivity to this pollutant were evaluated and compared to bare n- $\text{SnO}_2$  nanowire sensors, showing significant improvements in terms of sensitivity and selectivity. Based on the tests with individual nanowire and *ex-situ* SAEDS analysis, the working principle of the p-n junction heterostructure was modeled.

## 5.2 Materials

Like SnO<sub>2</sub> nanowires, CuO@SnO<sub>2</sub> nanowires were also supplied by our colleagues of European FP7 project (S3) from the University of Cologne. The production followed a two step chemical vapour deposition (CVD) of corresponding metal precursors. In the first stage, single crystalline SnO<sub>2</sub> nanowires were deposited using Sn(OBut)<sub>4</sub> at 725°C on Al<sub>2</sub>O<sub>3</sub> substrates covered with gold nanoparticles [17]. In the second stage, copper particles were deposited on the as grown SnO<sub>2</sub> nanowires by the CVD with [(C<sub>5</sub>H<sub>4</sub>N)<sub>2</sub> Cu<sup>II</sup> (CHCOCF<sub>3</sub>)<sub>2</sub>]<sub>2</sub>, following a procedure reported in ref.[18] (T<sub>substrate</sub> = 780°C, T<sub>precursor</sub> = 155°C, t = 40 min). The resulting SnO<sub>2</sub> nanowires decorated with Cu particles of average 200 nm in diameter were annealed in air at 300°C for 24h for oxidation. After annealing, a size-increase of particles was evident due to the volume expansion associated to the transformation of Cu to CuO. SAEDS analysis coupled with TEM observation confirmed the presence of crystalline SnO<sub>2</sub> as well as the copper oxide (figure 5.1). No atomic resolution Transmission Electron Microscopy (TEM) image of the CuO-SnO<sub>2</sub> interfaces could be obtained due to the large dimensions of both the nanowires and nanoparticles.

## 5.3 Results and discussions

### 5.3.1 H<sub>2</sub>S sensing with bare SnO<sub>2</sub> nanowire

H<sub>2</sub>S sensing with SnO<sub>2</sub> nanowire resembles the sensing of NH<sub>3</sub> in a great extent. Although a smaller range of H<sub>2</sub>S concentration was applied (see figure 5.2), the sensitivity was comparable with previous NH<sub>3</sub> tests, showing the cross sensitivity of this material toward gases of similar redox property. Nevertheless, the response followed regular temperature and target gas



concentration dependence, which has the highest sensitivity at 250°C but the fastest response at 300°C.

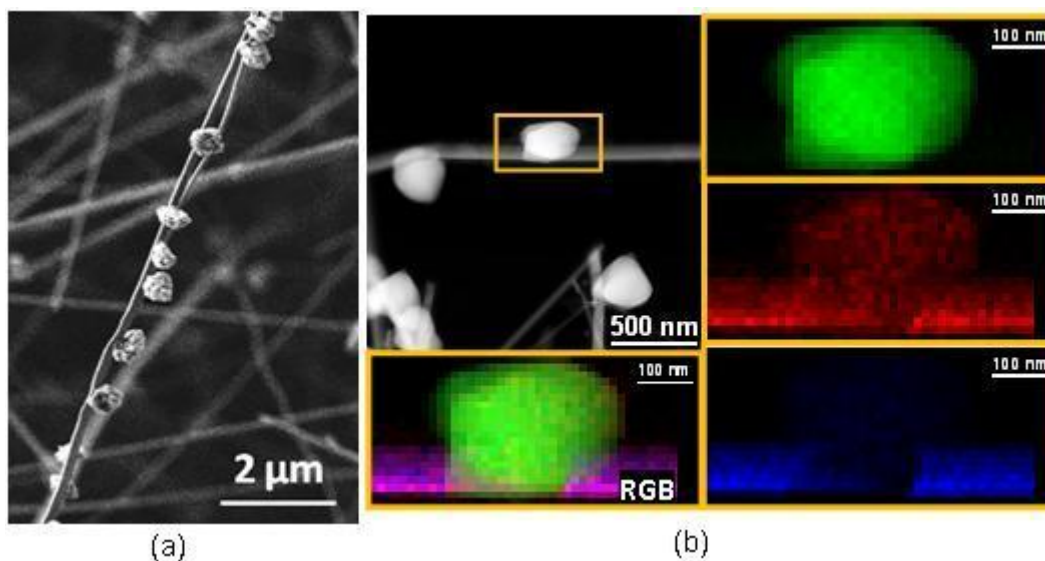


**Figure 5.1** (a) SEM image of a CuO@SnO<sub>2</sub> nanowire in the background of nanowire bundles. The lengths of the SnO<sub>2</sub> nanowires are in the range of 10 to 20 μm and diameters about 100 to 300 nm. The CuO nanoparticles have irregular shapes, the diameters are about 100 to 300 nm if considered as a sphere. The pictures in (b) are the TEM image and the SAEDS mapping of Cu (green), O (red) and Sn (blue).

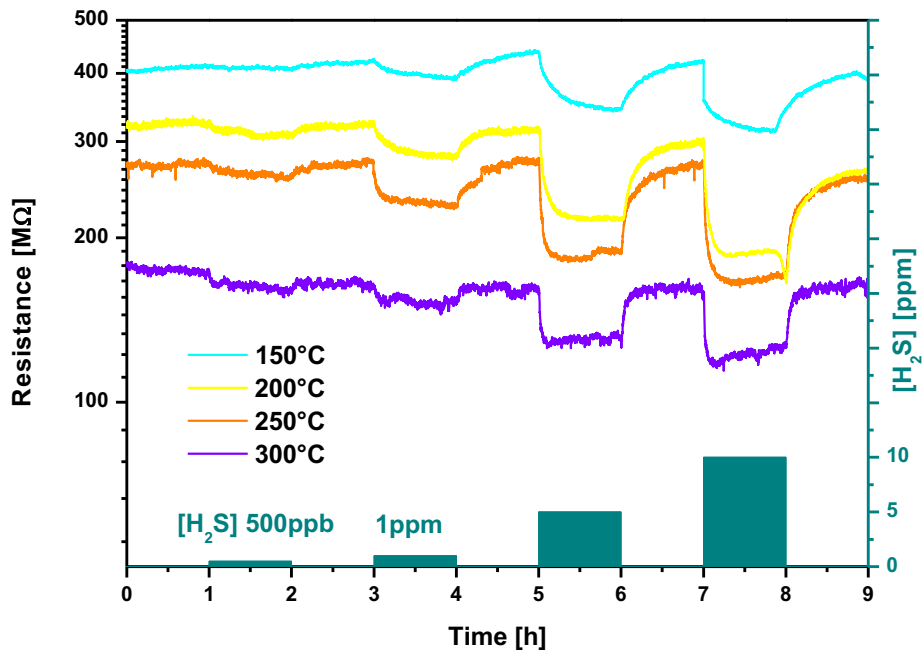


**Figure 5.2** H<sub>2</sub>S sensing response of an individual SnO<sub>2</sub> nanowire sensor.

### 5.3.2 H<sub>2</sub>S sensing with CuO decorated SnO<sub>2</sub> nanowires

Sensing H<sub>2</sub>S with individual CuO@SnO<sub>2</sub> nanowires obtained much higher sensitivity at the higher H<sub>2</sub>S concentrations applied (5 and 10ppm) while the sensitivity at lower concentrations (0.5 and 1ppm) remained on a par with bare SnO<sub>2</sub> nanowire. As can be seen in figure 5.3, the sensitivity  $S$  is 1.3, 8 and 20.1 for 1, 5 and 10ppm respectively. A comparison of sensitivity between bare SnO<sub>2</sub> and CuO decorated SnO<sub>2</sub> nanowires is given in figure 5.4.

Although improved sensitivity was obtained with several CuO@SnO<sub>2</sub> nanowires in individual configuration, the stability appeared to be an issue. The resistance value was often unstable when the nanowire was exposed to H<sub>2</sub>S. These structures could be reused for a next sensing test, but

their resistance become unstable even in SA. This issue is likely caused by the instability of SnO<sub>2</sub> and CuO interface during the sulfurization/oxidation reaction of CuO nanoparticles which will be described in next the section.

The H<sub>2</sub>S sensing experiment performed by the producer of these nanowires with bulk quantity of CuO@SnO<sub>2</sub> nanowires however showed sufficient stability and reproducibility, showing the advantage of using a macroscopic sensing layer [18]. With the CuO@SnO<sub>2</sub> nanowires, they also tested NH<sub>3</sub> and CO sensing, but showed no visible improvement comparing to bare SnO<sub>2</sub> nanowires. It is worth noting that a threshold H<sub>2</sub>S concentration of about 0.6ppm was found for the sensitivity enhancement in the experiments. This result, to some extent, justifies our finding that certain H<sub>2</sub>S concentration has to be reached for the sensitivity boost.

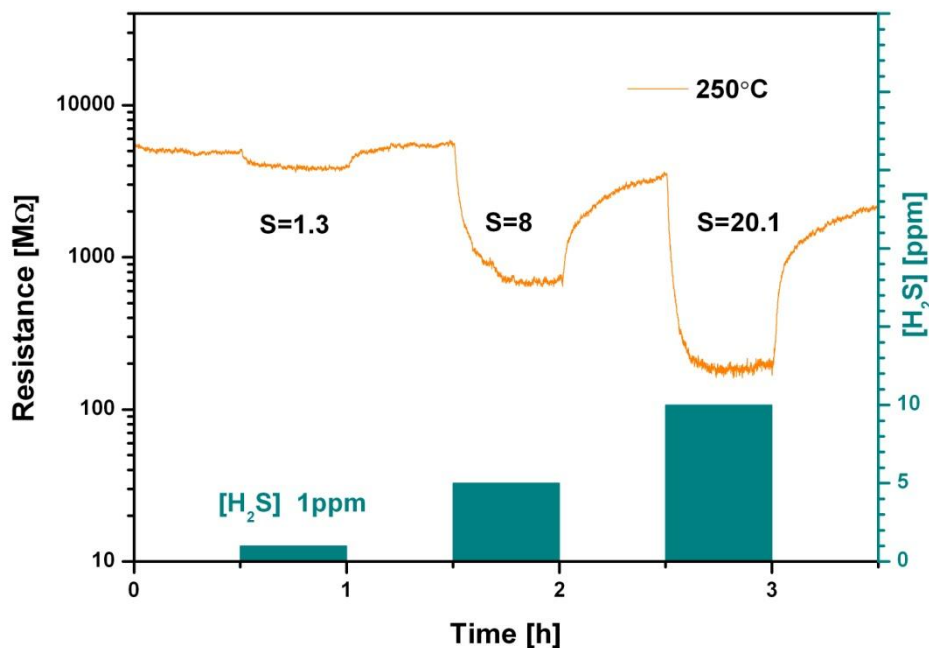


**Figure 5.3** Response of an individual CuO@SnO<sub>2</sub> nanowire to H<sub>2</sub>S pulses.

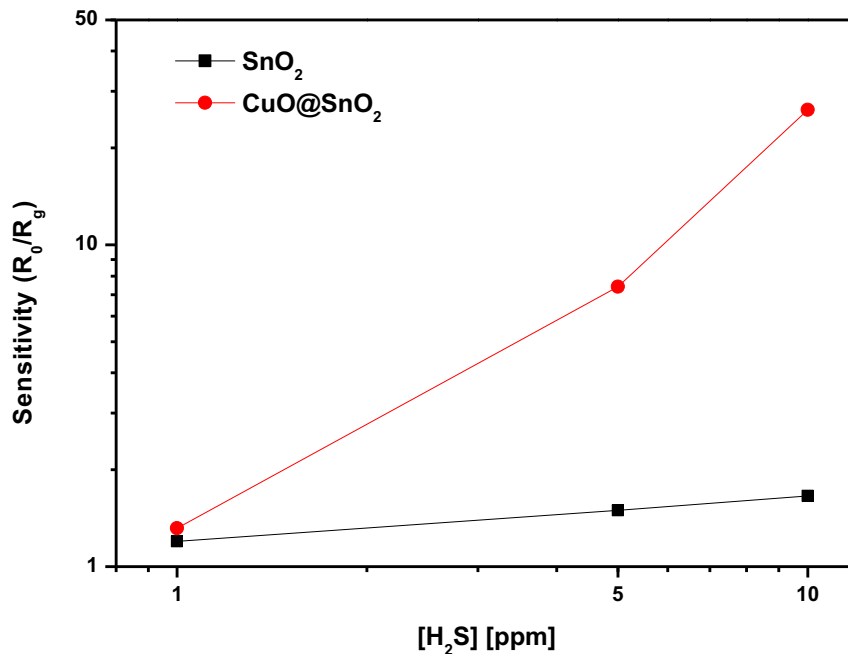


**Figure 5.4** Sensitivity comparison of SnO<sub>2</sub> and CuO@SnO<sub>2</sub> nanowires.

### 5.3.3 Qualitatively modeling of H<sub>2</sub>S sensing mechanisms by CuO decorated SnO<sub>2</sub> and SnO<sub>2</sub> nanowires

#### *Standard explanation*

It is well known that using heterostructures of the MOX with noble metals or other MOX is an effective way to improve the selectivity of MOX gas sensors by highlighting the response to certain gas specie while keeping the others low. Among the CuO-SnO<sub>2</sub> heterostructures that have been reported, the morphology varies depending on the methods of preparation [12-16]. But the proposed mechanism of their H<sub>2</sub>S sensing has been only one: the reversible modulation of the

depletion region at the p-n junction of CuO-SnO<sub>2</sub> interface due to the reversible reactions of CuO, H<sub>2</sub>S and O<sub>2</sub>. First of all, due to the small diameter of the SnO<sub>2</sub> nanowire, the depletion region has a profound effect on the conductivity of the nanowire. In accordance, significantly increased resistance of the CuO decorated SnO<sub>2</sub> nanowire comparing to bare SnO<sub>2</sub> nanowire was found (more than 1 order of magnitude when comparing figure 5.2 and figure 5.3, neglecting other size differences). When the nanowire is exposed to H<sub>2</sub>S at high temperature, sulfurization of CuO takes place as given in equation (R5.1) [19, 20]. The CuO is transferred into CuS, a metallic material. The p-n junction breaks up and the depletion region disappears to allow the free transport of charge carrier so the resistance diminishes.



In a reverse process, when the H<sub>2</sub>S is removed from air, spontaneous oxidation of CuS happens according to reaction equation (R5.2) [21, 22]. The p-n junction will be regenerated and the resistance returns close to the original value. It is clear that above sulfurization (R5.1) and oxidation (R5.2) reactions are two opposite reactions that occur simultaneously when H<sub>2</sub>S is mixed with SA. This explains why a certain H<sub>2</sub>S concentration is required when the high sensitivity can be measured because the H<sub>2</sub>S has to be in enough high concentration to let the sulfurization reaction dominate.

Figure 5.4 depicts the as-described H<sub>2</sub>S sensing mechanism of the CuO@SnO<sub>2</sub> nanowire. CuO as a p-type and SnO<sub>2</sub> as an n-type semiconductor form a p-n junction with a depletion zone in between. In the p and n-type semiconductor, depletion zone width is related to the doping and the absolute value of the working function of the involved semiconductor materials. Therefore, any

structural/compositional modification of the MOX which involves Fermi level variations will change the depletion zone and as a result, strongly modulates the electrical properties of the entire heterostructure. Sulfurization of the copper oxide and finally bring the ternary  $\text{Cu}_x\text{O}_z\text{S}_y$  system toward metallic  $\text{Cu}_x\text{S}_y$  changes the p-n junction toward a metal-semiconductor interface which have a significant effect on the electrical properties of the sensor.

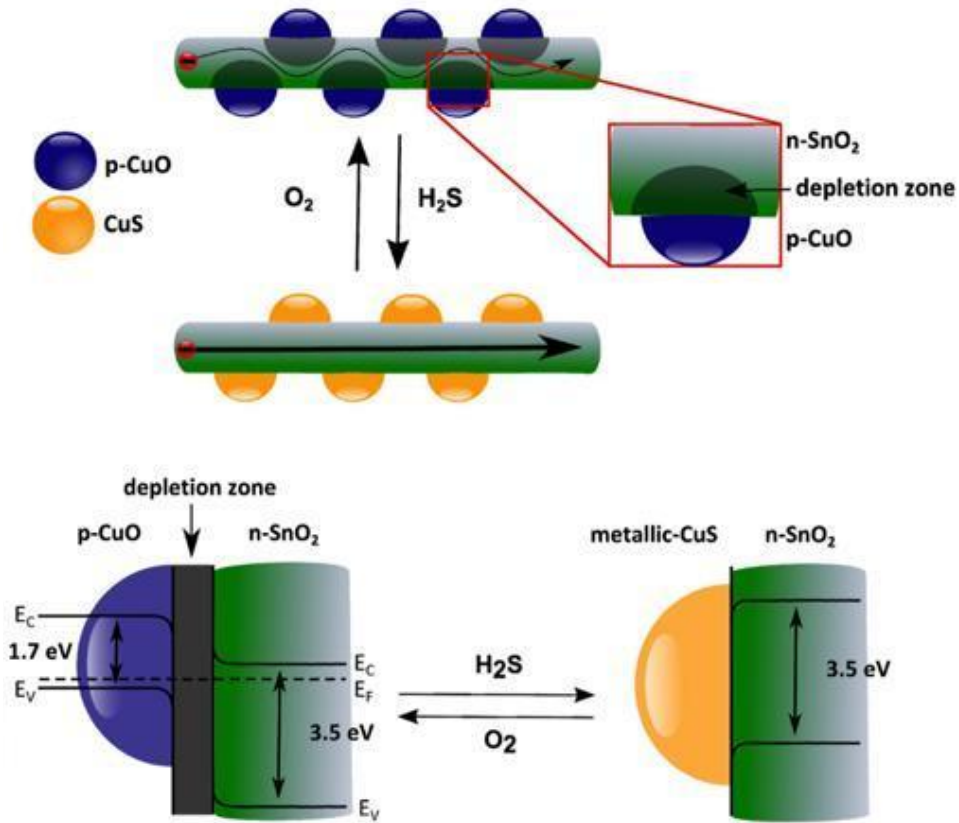


**Figure 5.5** General sketch of the heterostructure: p-CuO particles on the n-SnO<sub>2</sub> surface create a p-n junction. The depleted region reduces the effective conduction channel in the nanowire, leading to a higher resistance. During H<sub>2</sub>S sensing, p-CuO particles change to metallic CuS, resulting in a breakup of the p-n junction, a wider conduction channel in the nanowire and as a consequence lower the resistance.

The surface redox reactions taking place at the SnO<sub>2</sub> surface of both nanowires should not be forgotten. As written in equations (R5.3) and (R5.4) [23, 24], these reactions result in the release of electrons back into the SnO<sub>2</sub> and therefore are able to explain the sensing response of the bare SnO<sub>2</sub> nanowires. In the case of SnO<sub>2</sub>-CuO nanowires, such reactions also take place, but make a second order effect on the overall resistance modulation.



### ***SAEDS analysis***

In order to provide some evidence to the as summarized H<sub>2</sub>S sensing mechanism of the CuO@SnO<sub>2</sub> nanowire, SAEDS analyses were taken in a SEM with the CuO nanoparticle as the object of observation. Due to the resolution limit of the technique, the signal acquiring area is usually several times larger than the projection area of the CuO nanoparticles and the Cu atoms generally only correspond to less than 1at.% of total detected atoms. Therefore, following results are rather qualitative than quantitative.

Figure 5.6 shows the site where the SAEDS measurements were centered. As a reference site, the measurement at "Spectrum1" in figure 5.6a detected neither Cu nor S. After heating the nanowire in 10ppm H<sub>2</sub>S at 250°C for 2h and allowed to cool down in the same gas, an average S/Cu atomic ratio of about 1 was obtained with several measurements at the "Spectrum2" in Figure 5.6b. Repeating the measurement at the "Spectrum2" after heating at 250°C in SA obtained the average S/Cu value of 0.6. These results indicate that the CuO nanoparticle was transferred into CuS after heating with H<sub>2</sub>S, but the heating in SA did not completely oxidize it, instead, CuS<sub>x</sub>O<sub>1-x</sub> appears to be the proper formula. Overall, the SAEDS measurements

confirmed the incorporation of S into CuO, and indirectly the role in the H<sub>2</sub>S sensing mechanism proposed.

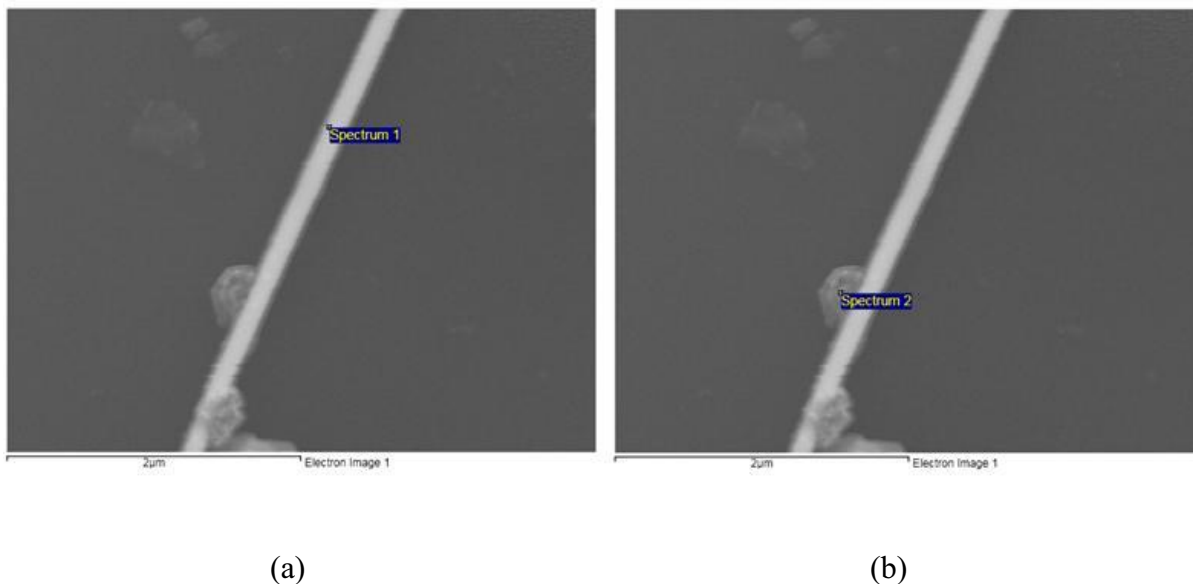


**Figure 5.6** Positions where SAED tests were performed. (a) bare SnO<sub>2</sub> surface and (b) CuO particle.

## 5.4 Conclusions

Individual SnO<sub>2</sub> and CuO decorated SnO<sub>2</sub> nanowires were evaluated for H<sub>2</sub>S sensing applications. The specific interaction between this pollutant and the CuO particles and the amplifying effect of the p-n junction strongly enhanced the sensitivity and selectivity to this gas in comparison to other reducing gas of reference. The proposed sensing mechanism was indirectly validated by the SAED measurements. The CuO decorated SnO<sub>2</sub> nanowire appears to be a promising material for H<sub>2</sub>S sensing, especially for alarm applications.



## References

- [1] Wikipedia, Hydrogen sulfide, [https://en.wikipedia.org/wiki/Hydrogen\\_sulfide](https://en.wikipedia.org/wiki/Hydrogen_sulfide), (2013-3-15).
- [2] C.H. Selene, J. Chou, Hydrogen Sulfide: Human Health Aspects, in: Concise International Chemical Assessment Document WHO, 2003.
- [3] Occupational Safety and Health Standards -Toxic and Hazardous Substances, in: OSHA (Ed.), U.S. Department of Labor.
- [4] M.G. Costigan, Hydrogen sulfide: UK occupational exposure limits, Occupational and Environmental Medicine, 60 (2003) 308-312.
- [5] Occupational Health and Safety of Hydrogen Sulphide (H<sub>2</sub>S), in: CAPP (Ed.), 2003.
- [6] G. Sberveglieri, Recent developments in semiconducting thin-film gas sensors Sens. Actuators: B, 23 (1995) 103 - 109.
- [7] A. Kolmakov, M. Moskovits, Chemical sensing and catalysis by one-dimensional metal-oxide nanostructures, Annu. Rev. Mater. Res, 34 (2004) 151.
- [8] S.K. Pandey, K.-H. Kim, K.-T. Tang, A Review of Sensor-Based Methods for Monitoring Hydrogen Sulfide, TrAC, Trends Anal. Chem., 32 (2012) 87–99.
- [9] N. Yamazoe, J. Tamaki, N. Miura, Role of hetero-junctions in oxide semiconductor gas sensors, Materials Science and Engineering B, 41 (1996).
- [10] X.M. Shuai, W.Z. Shen, A Facile Chemical Conversion Synthesis of ZnO/ZnS Core/Shell Nanorods and Diverse Metal Sulfide Nanotubes, J. Phys. Chem. C, 115 (2011) 6415- 6422.
- [11] Y. Takao, K. Miyazaki, Y. Shimizu, M. Egashira, High Ammonia Sensitive Semiconductor Gas Sensors with Double-Layer Structure and Interface Electrodes, J. Electrochem. Soc, 141 (1994) 1028-1034.
- [12] I.-S. Hwang, J.-K. Choi, S.-J. Kim, K.-Y. Dong, J.-H. Kwon, B.-K. Ju, J.-H. Lee, Enhanced H<sub>2</sub>S sensing characteristics of SnO<sub>2</sub> nanowires functionalized with CuO, Sensors and Actuators B: Chemical, 142 (2009) 105-110.
- [13] X.H. Kong, Y.D. Li, High sensitivity of CuO modified SnO<sub>2</sub> nanoribbons, Sensors and Actuators B, 105 (2005) 449- 453.
- [14] X.Y. Xue, L. Xing, Y. Chen, S. Shi, Y. Wang, T. Wang, Synthesis and H<sub>2</sub>S sensing properties of CuO-SnO<sub>2</sub> core/shell PN-junction nanorods, J. Phys. Chem. C, 112 (2008) 12157- 12160.
- [15] L.A. Patil, D.R. Patil, Heterocontact type CuO-modified SnO<sub>2</sub> sensor for the detection of a ppm level H<sub>2</sub>S gas at room temperature, Sensors and Actuators B, 120 (2006) 316-323.

- [16] S.-W. Choi, J. Zhang, K. Akash, S.S. Kim, H<sub>2</sub>S sensing performance of electrospun CuO-loaded SnO<sub>2</sub> nanofibers, *Sensors and Actuators B: Chemical*, 169 (2012) 54-60.
- [17] S. Mathur, S. Barth, H. Shen, J.-C. Pyun, U. Werner, Size-dependent Photoconductance in SnO<sub>2</sub> Nanowires, *small*, 1 (2005) 713–717.
- [18] I. Giebelhaus, E. Varechkina, T. Fischer, M. Rumyantseva, V. Ivanov, A. Gaskov, J.R. Morante, J. Arbiol, W. Tyrra, S. Mathur, One-dimensional CuO-SnO<sub>2</sub> p-n heterojunctions for enhanced detection of H<sub>2</sub>S, *Journal of Materials Chemistry A*, 1 (2013) 11261-11268.
- [19] J. Tamaki, T. Maekawa, N. Miura, N. Yamazoe, CuO-SnO<sub>2</sub> element for highly sensitive and selective detection of H<sub>2</sub>S, *Sensors and Actuators B: Chemical*, 9 (1992) 197-203.
- [20] T. Pagnier, M. Boulova, A. Galerie, A. Gaskov, G. Lucazeau, Reactivity of SnO<sub>2</sub>-CuO nanocrystalline materials with H<sub>2</sub>S: a coupled electrical and Raman spectroscopic study, *Sensors and Actuators B: Chemical*, 71 (2000) 134-139.
- [21] J.G. Dunn, C. Muzenda, Thermal oxidation of covellite (CuS), *Thermochimica Acta*, 369 (2001) 117-123.
- [22] C. Mu, J. He, Confined conversion of CuS nanowires to CuO nanotubes by annealing-induced diffusion in nanochannels, *Nanoscale Research Letters*, 6 (2011) 150.
- [23] V.V. Malyshev, A.V. Pislyakov, SnO<sub>2</sub>-based thick-film-resistive sensor for H<sub>2</sub>S detection in the concentration range of 1–10 mg m<sup>-3</sup>, *Sensors and Actuators B: Chemical*, 47 (1998) 181-188.
- [24] X. Li, Y. Wang, Y. Lei, Z. Gu, Highly sensitive H<sub>2</sub>S sensor based on template-synthesized CuO nanowires, *RSC Advances*, 2 (2012) 2302-2307.

## **6. Preparation and characterization of individual CuO nanowire sensors for gas sensing**

Up to now, the mostly studied MOX sensing materials are mainly n-type semiconductors, e.g., SnO<sub>2</sub> and In<sub>2</sub>O<sub>3</sub>. The performance of p-type MOX is however not often discussed and as a result, the knowledge about the sensing properties of p-type MOX is relatively scarce. There is thus a potential to use these materials for future improvements in the MOX sensor field. And from a fundamental point of view, it is interesting to study the synergy between the gas molecules and the p-type MOX surface.

### **6.1 Introduction**

With the reported band gap in the range of 1.0 to 1.9eV [1-3], cupric oxide (CuO) is an intrinsic p-type semiconductor due to the presence of Cu vacancies [4, 5]. Although the physical properties of this material have been less studied [6, 7] and its integration in devices has been quite limited [8] compared to the lower oxide, i.e., cuprous oxide (Cu<sub>2</sub>O); CuO has been studied in the past as a gas sensing material in the structures of porous film or compact thin film [9-11].

More recently, the discovery of a facile method — direct oxidation of Cu [4, 12, 13] to prepare high quality CuO nanowires has triggered a new wave of research. Comparing to the more conventional methods, e.g., template based, electro-spinning or solution synthesis [14-16], this method requires significant less lab expertise while offers nanowires with pleasing properties in terms of crystallinity and dimension [17]. The p-type character was validated in both back-gated

single nanowire field effect transistor (FET) measurements [18-20] and XPS band structure studies [7]. The optical emission properties were studied by photoluminescence spectroscopy [21], and field emission characteristics were also reported [7]. In regards with gas sensing, promising properties have been demonstrated, either with bundles [14, 22] of nanowires or individual structures [18, 19]. Nevertheless, a reliable determination of the conductivity was still not available.

In this work, we prepared CuO nanowires by direct oxidation of Cu foil in air; the influence of heating time on the nanowire morphology was investigated and the electrical properties were determined using devices fabricated with focused ion beam (FIB) nanolithography. The gas sensing performance of individual CuO nanowire sensors toward NO<sub>2</sub>, NH<sub>3</sub> and H<sub>2</sub>S were examined comparing to the response to those obtained with individual SnO<sub>2</sub> nanowires.

## **6.2 Results and discussion**

### **6.2.1 Morphology and crystalline structure**

The Cu foil after heating was covered with thin black layers on both sides, which crack easily and detach. SEM observations showed that the as grown nanowires were there. Figure 6.1 contains both top and cross sectional images of the nanowires on the Cu foils. The growth was more profound within the first 2 h and the length change was less evident after that. In all the samples, the nanowires had two typical length ranges: roughly 3 to 5 μm and 10 to 15 μm for the 30 min and 1 h growth; 5 to 10 μm and 15 to 25 μm for the longer growth times. The shorter nanowires have needle like shapes with the diameter (approx. 100 to 300 nm) larger at the

bottom. The longer nanowires have a thinner and more uniform diameter of about 100 nm. The identification of such two types of morphology was also reported by other group [23]. Images in figure 6.2 provide a better view of this character.

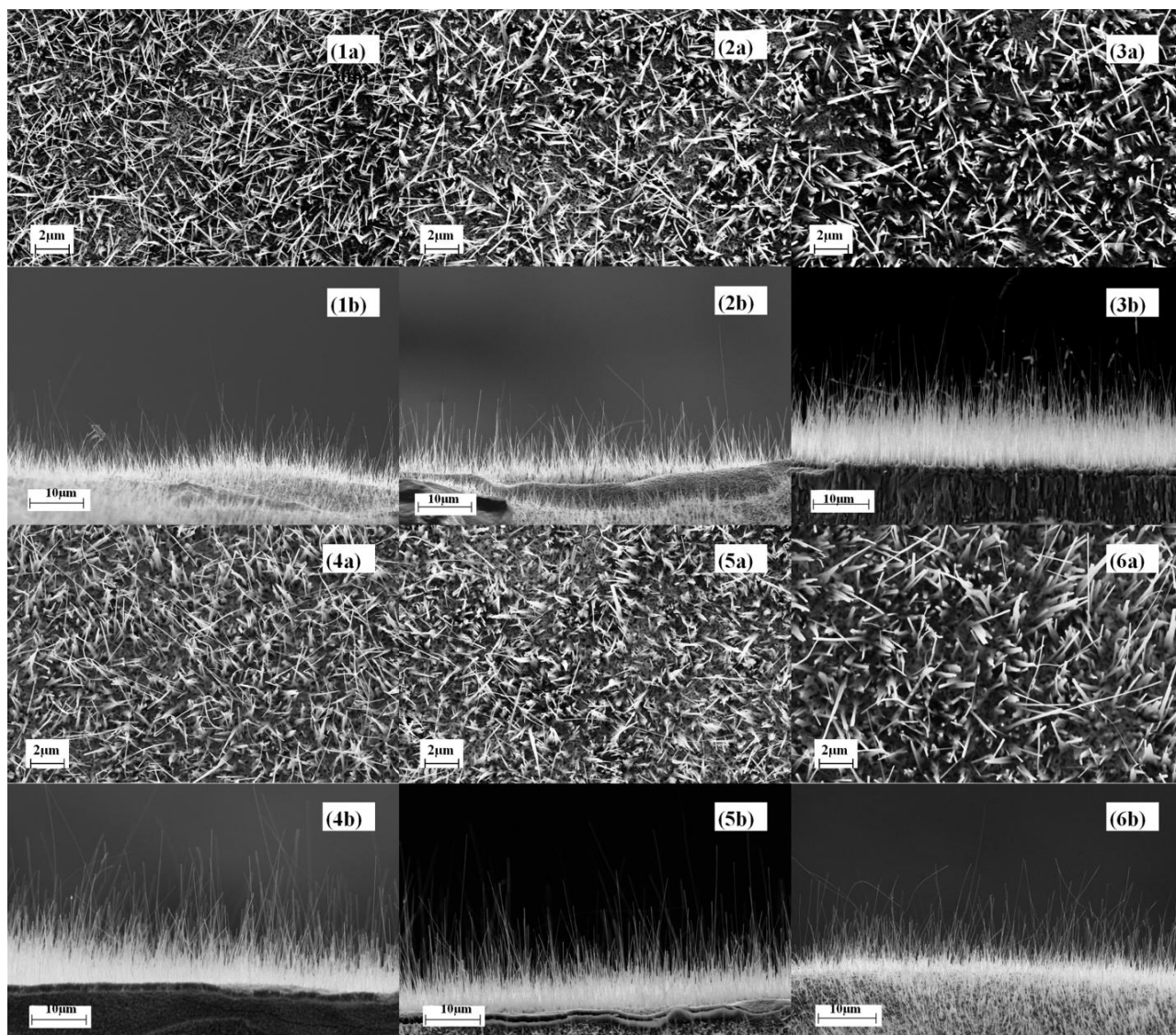


**Figure 6.1** Top and cross sectional images of CuO nanowires with increasing growth time. 1a&b: 0.5h; 2a&b: 1h; 3a&b: 2h; 4a&b: 4h; 5a&b: 6h; 6a&b: 8h. The scale bars are 2 μm for top view and 10 μm for side view.

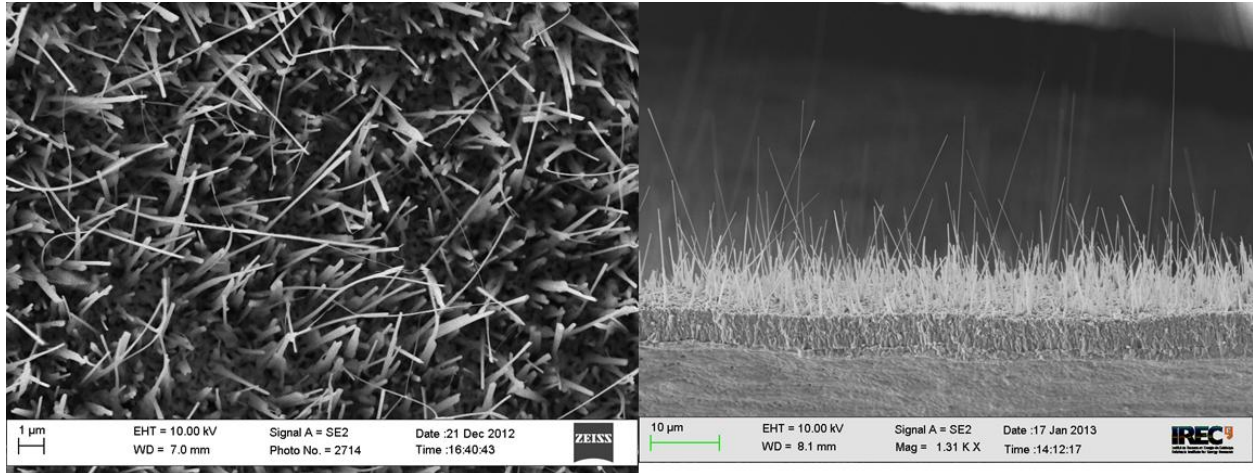
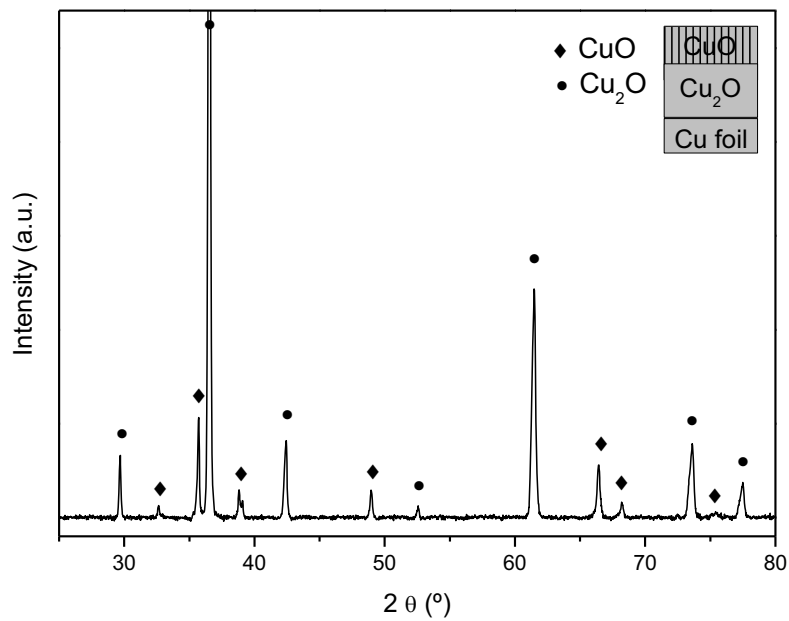


Figure 6.2 Top and cross sectional images of CuO nanowires to show the difference in morphologies.

XRD pattern in figure 6.3 indicates the coexistence of  $\text{Cu}_2\text{O}$  and  $\text{CuO}$  phases. Cu peaks are not seen because the metallic copper is covered by the oxidized layers. SAEDS analysis on the cross section of the black layer has given the Cu/O atomic ratio of 1.8 in the bottom part and 0.8 at the interface/nanowire part (figure 6.4). Considering the accuracy limitation of EDS analysis and the potential oxygen over counting due to adsorbed species, e.g.,  $\text{H}_2\text{O}$  and  $\text{O}_2$ , the bottom layer and the interface/nanowire part can be assigned to be  $\text{Cu}_2\text{O}$  and  $\text{CuO}$  respectively. According to the phase diagrams [24], the three phases coexist (Cu,  $\text{Cu}_2\text{O}$  and  $\text{CuO}$ ) at temperatures below  $1050^\circ\text{C}$ . The growth of  $\text{CuO}$  nanowires involved the progressive oxidation of the copper substrate as given by equations (R6.1) and (R6.2) and the relative amount of  $\text{Cu}_2\text{O}$  and  $\text{CuO}$  strongly depends on the temperature and the oxygen partial pressure during the process:





**Figure 6.3** XRD pattern of CuO/Cu<sub>2</sub>O film, after thermal oxidation for 4h at 500°C in air.

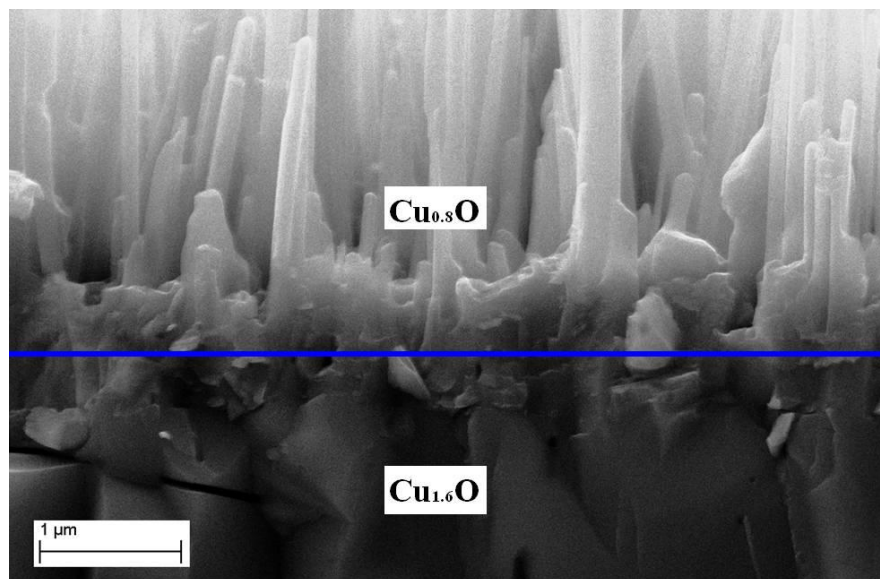


**Figure 6.4** Cross sectional image showing the Cu<sub>2</sub>O bottom layer, CuO interface layer, and CuO nanowires. The blue line represents a border between the two compositions.

It is often observed [23, 25, 26] that the growth rate of CuO nanowires length, CuO interface layer and Cu<sub>2</sub>O layers' thickness all followed a parabolic law with time, evidencing the Cu ion diffusion as the parameter controlling the whole growth process. L. Yuan et al.[23] further observed that the nanowires were mainly grown from the CuO grains, suggesting [23, 25] that the diffusion of Cu cations along the grain boundary is driven by the compressive stress at the CuO layer caused by the interaction between the CuO and Cu<sub>2</sub>O layers.

### 6.2.2 Electrical measurements

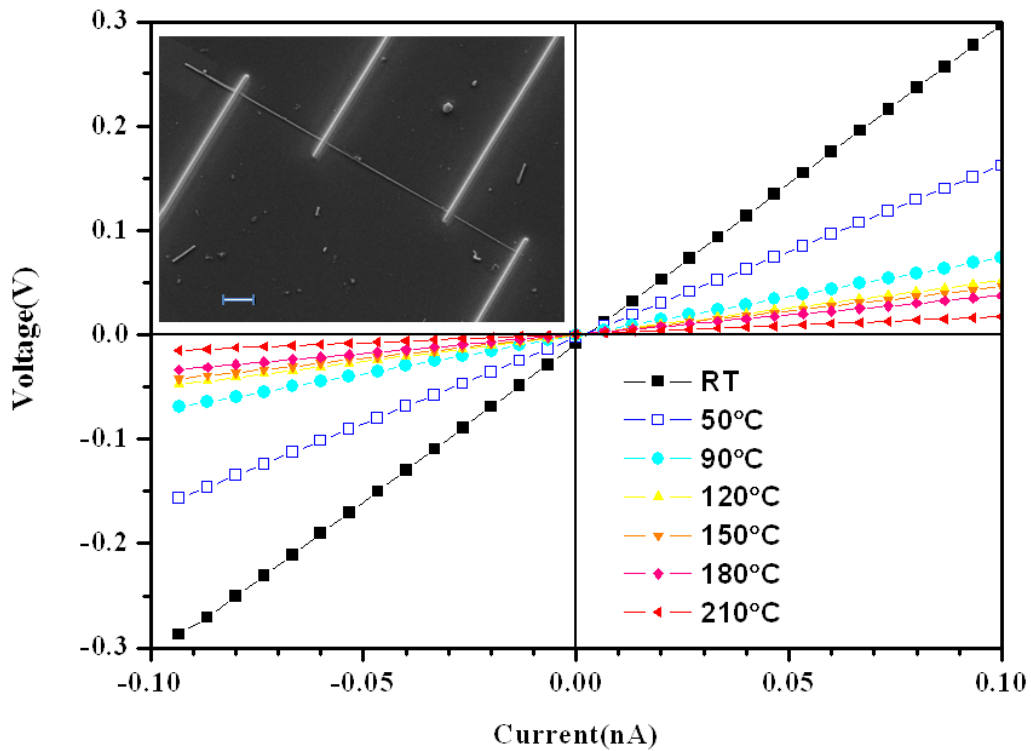


**Figure 6.5** 4-probe IV measurements on CuO nanowire at different temperatures. Inset: SEM of the CuO nanowire contacted by 4 Pt strips, scale bar is 2 μm.



4-probe IV measurements were performed on individual nanowires. As shown in figure 6.5, the nanowire has diameter of about 100nm and length of 21 $\mu$ m. Voltage was measured while current was swept over the range from -0.1 to +0.1nA. The resistance of the nanowire decreased as temperature increase, showing the semiconductor character of the sample. The conductivity  $\sigma$  at room temperature was calculated to be  $6.9 \times 10^{-3} \Omega^{-1} \text{cm}^{-1}$ , which is on the same magnitude but larger than the  $1.1 \times 10^{-3} \Omega^{-1} \text{cm}^{-1}$  reported for the thermally oxidized CuO nanowire FET device in ref.[18] and  $5.6 \times 10^{-3} \Omega^{-1} \text{cm}^{-1}$  for the sputtered CuO thin film in ref.[27]. The relative large value of conductivity can be ascribed to the exclusion of contact resistance in the 4-probe measurement and the potential contamination of CuO nanowire surface by Pt deposition [28].

### **6.2.3 Gas sensing and discussion**

As depicted in figures 6.6a-c, the resistive responses of the individual CuO nanowire in 2-probe configuration were tested with different concentrations of NH<sub>3</sub>, H<sub>2</sub>S and NO<sub>2</sub> in dry SA. The nanowire responded to all these gases by increasing the resistance in a reversible way. The upward change of resistance to NH<sub>3</sub>, H<sub>2</sub>S was expected because of the p-type of CuO and the reducing character of NH<sub>3</sub> and H<sub>2</sub>S. On the other hand, for NO<sub>2</sub>, the resistance changing tendency was contrary to the common response to oxidizing gases and the mechanism seemed more complex than it was initially expected.

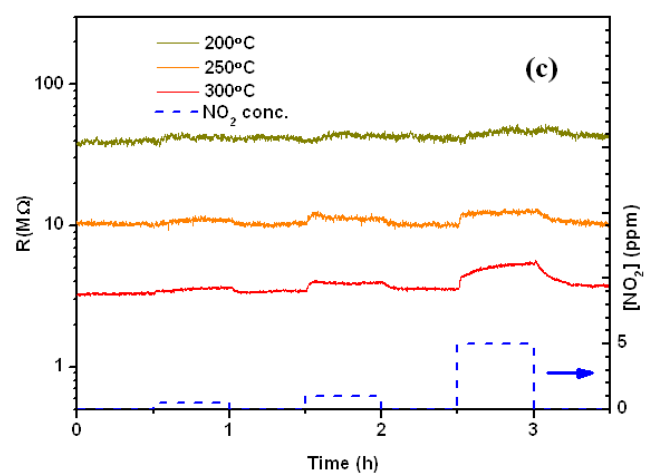
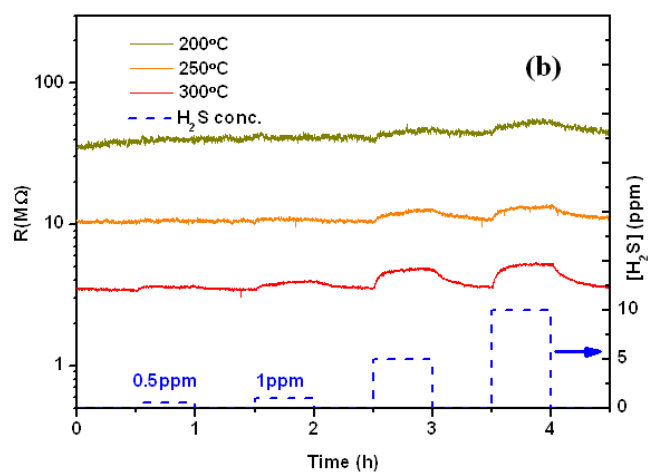
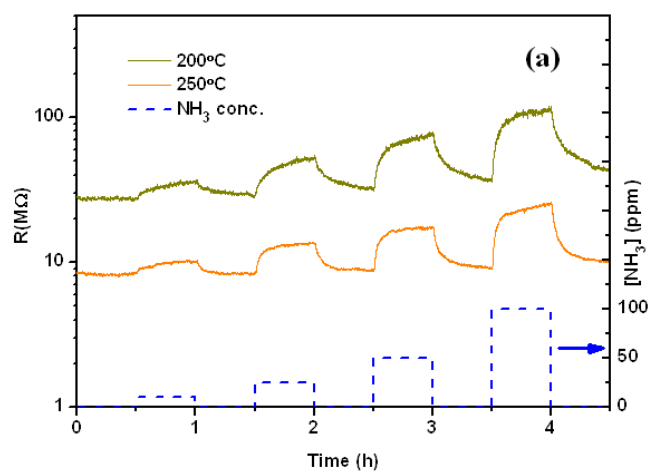


**Figure 6.6** Gas response of individual CuO nanowire to  $\text{NH}_3$  (a),  $\text{H}_2\text{S}$  (b) and  $\text{NO}_2$  (c).

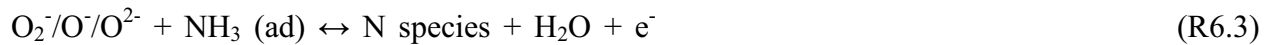
The optimal working temperature for NH<sub>3</sub> was between 200 and 250°C, whereas it was at 300°C for H<sub>2</sub>S and NO<sub>2</sub>. Due to the temperature resistance of the Pt contacts, higher temperatures were not allowed in these experiments. The responses at temperatures below 150°C were either very slow or negligible, therefore were omitted from further studies. SnO<sub>2</sub> was used as the reference material to compare the gas response observed with CuO nanowires. Due to the different changing tendency, here we define the sensitivity to be  $S = R_{gas}/R_{SA}$  for CuO nanowire and  $S = R_{SA}/R_{gas}$  for the SnO<sub>2</sub> nanowire presented in Chapter 4 ( $R_{gas}$ ,  $R_{SA}$  is the resistance in gas mixture and in dry SA, respectively). And response/recovery time ( $t_{res}/t_{rec}$ ) is the time corresponding to complete 90% of resistance changes.

### **NH<sub>3</sub>**

The  $S$  value to NH<sub>3</sub> ranged from 1.1 to 3.1, and it is higher than the obtained with individual SnO<sub>2</sub> nanowire based sensors ( $S= 1$  to 1.8) for the same NH<sub>3</sub> concentrations. The gas concentration dependence of  $S$  is plotted in logarithmic scale (see Fig. 6.7a) and fitted with the power function,  $S = a[conc.]^n$ , here  $[conc.]$  is the gas concentration and  $a$  and  $n$  are constants. The  $n$  obtained by fitting is also indicated in the figure (the curves with similar slopes are indicated with an  $n$  of average value). A clear difference of  $n$  value can be found between the CuO and SnO<sub>2</sub> nanowires. And the  $n$  of SnO<sub>2</sub> nanowire at 150°C is different from the rest of temperatures. The  $n$  is therefore both temperature and material dependent. The response time  $t_{res}$  ( $\approx 6$ min) is on par with the SnO<sub>2</sub> sensors. Slight faster responses are found at higher temperature. On the other side, the recovery time is much longer than the response time.

A few works [20, 29] have reported the sensing of NH<sub>3</sub> by CuO, but the detailed study of the sensing mechanism remains uncompleted. Nevertheless, the classic conduction model [30] of

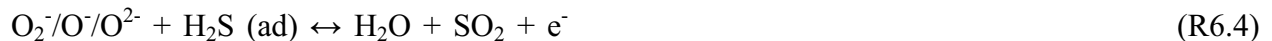
MOX gas sensors can be adopted to explain experimental data in rough approximation: the surface oxygen species ( $O_2^-$ ,  $O^-$  and  $O^{2-}$ ) withdraw electrons from the CuO so the resistance of this p-type semiconductor decreases because charge carriers (hole) are created. When the  $NH_3$  molecule is present, the complex surface reactions can be described by the following simple equation:



The electrons released by the surface reactions diminish the hole concentration, thereby increasing the resistance of the material.

### ***H<sub>2</sub>S***

Response to  $H_2S$  improved as the temperature increased. Thus, response to low level of  $H_2S$  (0.5, 1ppm) was obtained only at 300°C. The log-log plot of  $S$  vs.  $H_2S$  concentration is shown in figure 6.7b. In this case, the  $n$  difference between CuO and  $SnO_2$  is less significant and indeed the  $S$  of the two materials are very close. The rise of resistance matches with the expectation for a p-type semiconductor response to reducing gases. And the following equation [9] can qualitatively describe the involved sensing mechanism:



Despite the above surface reaction can properly explain the experimental result, there is another sensing mechanism that should be considered, the sulfurization of CuO into metallic CuS:



Reaction (R6.5) has been proposed to explain the resistance drop of CuO sensor at relative low temperature [31] or high  $H_2S$  concentrations [10, 17] as in those experimental conditions the

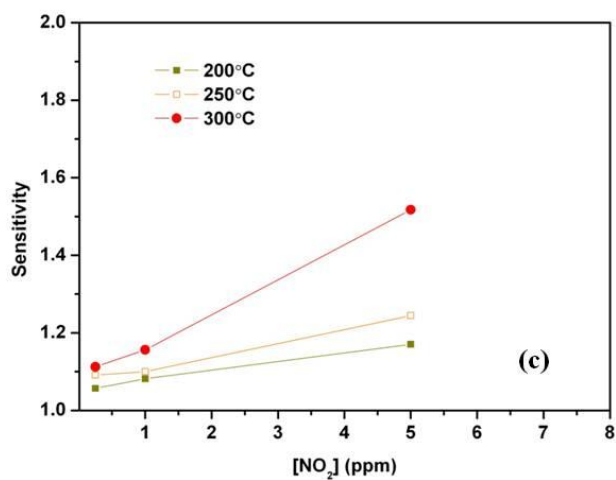
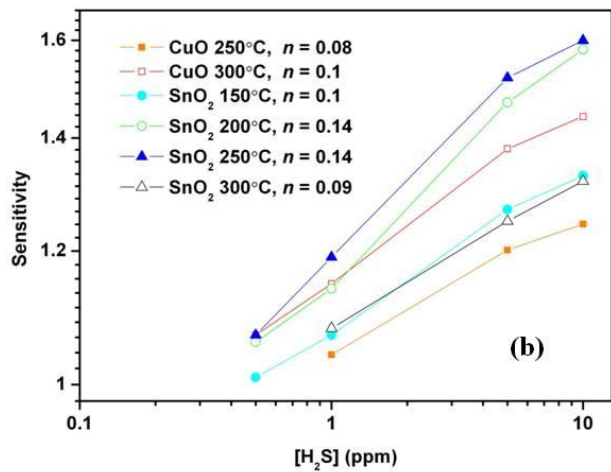
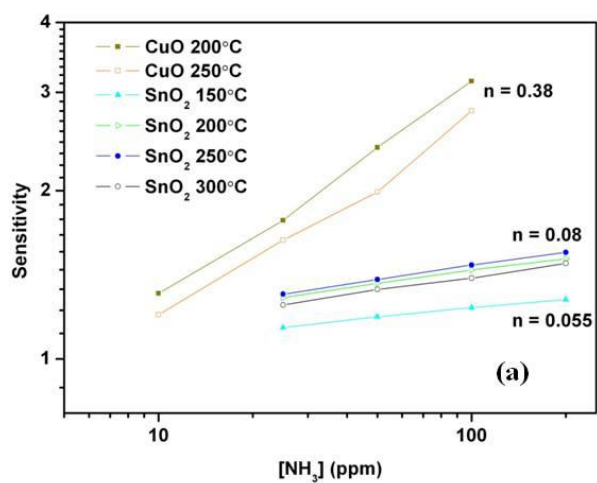


**Figure 6.7** Log-log plots of sensitivity vs. concentration.  $\text{NH}_3$  (a),  $\text{H}_2\text{S}$  (b) and  $\text{NO}_2$ (c).

sulfurization process is expected to become dominant. That means, depending on the  $\text{H}_2\text{S}$  concentration range and temperature, two different mechanisms have been suggested for the dynamic response of CuO to  $\text{H}_2\text{S}$  traces. Each one is able to explain one type of experimentally observed responses in CuO: resistance rise or drop. The mechanism that matches with our data is the surface O related redox process: at high temperature with low  $\text{H}_2\text{S}$  concentration, (R6.4) will have a major effect on the resistance, i.e., the release of electrons back to the CuO and the resistance of the p-type material will rise. On the other hand, if the  $\text{H}_2\text{S}$  concentration is high or the temperature is not favored by oxidation, the sulfurization of CuO occurs according to equation (R6.5). The formation of CuS decreases the resistance because CuS is metallic in nature. The reverse oxidation reaction leads to the recovery of the resistance.

In the Chapter 5, we have concluded that the sulfurization process (R6.5) was dominating the interaction between CuO nanoparticle and  $\text{H}_2\text{S}$ . Even through the same  $\text{H}_2\text{S}$  concentration and temperature were applied in the two adjacent works, we are seeing two different processes. SAEDS analysis (as shown in figure 6.8) was performed on the individual CuO nanowire heated in 10ppm of  $\text{H}_2\text{S}$  at  $250^\circ\text{C}$  for 2h and left to cool down in  $\text{H}_2\text{S}$ . While the copper counts for approximate 1.8% of total atoms, no sulfur was detected. Applying the same methods, roughly 1:1 ratio of Cu:S was found on the CuO nanoparticles attached to the  $\text{SnO}_2$  nanowire. These results suggest that those two materials (nanowire and nanoparticle) have undergone different interactions with the same  $\text{H}_2\text{S}$  applied. We ascribe this to the different crystallinity of the two CuO materials (single crystalline of CuO nanowire and amorphous CuO nanoparticles, which was produced by oxidizing the Cu nanoparticle [32]).

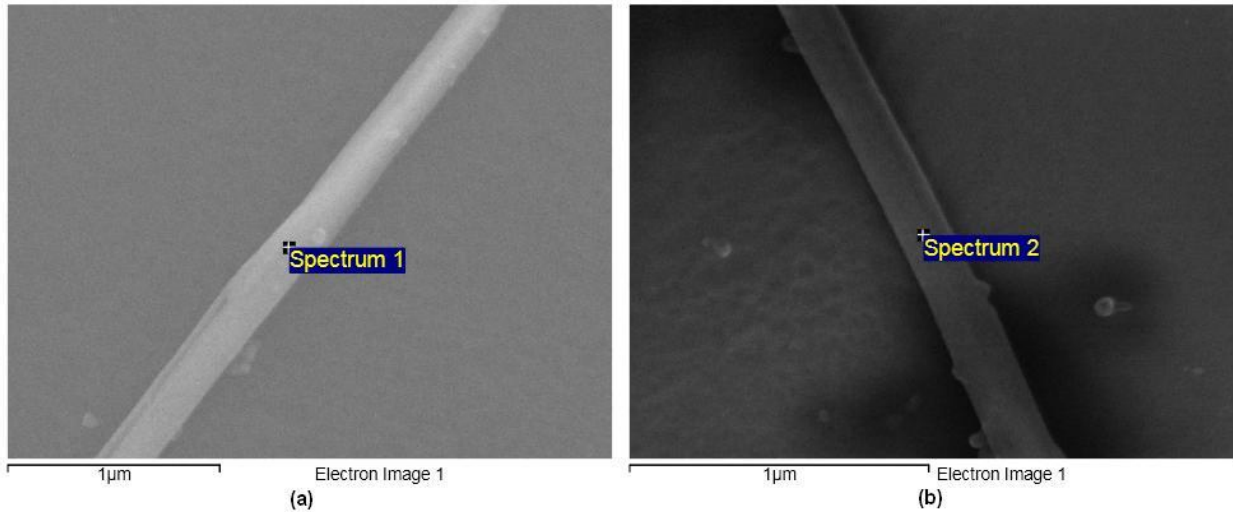


**Figure 6.8** Spot of SAEDS analysis on individual CuO nanowires heated 2h at 250°C either in 10ppm H<sub>2</sub>S (a) or in SA (b).

### *NO<sub>2</sub>*

In the case of NO<sub>2</sub>, small *S* was obtained at 200°C and the tests at RT and 150°C showed no response to the NO<sub>2</sub>. The concentration dependence of sensitivity is not linear in the log-log plot, therefore has been presented in a direct scale in figure 6.7c. It was surprising to see that the *S* increased at higher temperatures because the NO<sub>2</sub> is generally considered to be an oxidizing gas for metal oxides and upon adsorption, electron will transfer from the metal oxides to the NO<sub>2</sub> [18, 33, 34]:



The result of above surface process is the decrease of resistance in the p-type semiconductor, which is opposite to our experimental evidence. This phenomena can be explained by the concentration dependent sensing mechanism of NO<sub>2</sub> that was reported by Kim et al. [35]. It was

proposed that equation (R6.6) dominates when the NO<sub>2</sub> concentration is relatively high (temperature and material dependent, usually above several tenths of ppm). When the concentration is low, the surface reaction with adsorbed atomic oxygen will make the largest contribution to the resistance change [36]:



The release of electrons to a p-type semiconductor will then increase its resistance, which is the situation in our case. It is worth noting that the over-spread Pt in electron beam deposition might work as a catalyst to this process.

### 6.3 Conclusions

CuO nanowires were obtained by the facile method of thermal oxidation. The material after oxidation was examined with XRD, SEM and SAEDS. Using FIB lithography, the electrical conductivity of CuO individual nanowires was characterized with the 4-probe method. CuO nanowires in the individual configuration were evaluated for gas sensing and were found to be a promising material. In terms of NH<sub>3</sub> sensitivity, CuO nanowires showed higher sensitivity than the previously reported SnO<sub>2</sub> nanowires. The response to H<sub>2</sub>S led to the conclusion of a different CuO-H<sub>2</sub>S interaction mechanism from the sulfurization process on the CuO decorated SnO<sub>2</sub> nanowire. The response to NO<sub>2</sub> at low concentrations ( $\leq 5$ ppm) indicates that the surface oxygen species is again responsible for the sensing governance in this experimental condition. The gas sensing results shown here has helped the understanding of different sensing mechanisms by CuO.



## References

- [1] Cupric oxide (CuO) electronic properties, O. Madelung, U. Rössler, M. Schulz (Eds.).
- [2] K.L. Hardee, A.J. Bard, Semiconductor Electrodes: X . Photoelectrochemical Behavior of Several Polycrystalline Metal Oxide Electrodes in Aqueous Solutions, *Journal of The Electrochemical Society*, 124 (1977) 215-224.
- [3] W.Y. Ching, Y.-N. Xu, K.W. Wong, Ground-state and optical properties of Cu<sub>2</sub>O and CuO crystals, *Physical Review B*, 40 (1989) 7684-7695.
- [4] D. Zappa, E. Comini, R. Zamani, J. Arbiol, J.R. Morante, G. Sberveglieri, Copper oxide nanowires prepared by thermal oxidation for chemical sensing, *Procedia Engineering*, 25 (2011) 753-756.
- [5] Y. Peng, Z. Zhang, T.V. Pham, Y. Zhao, P. Wu, J. Wang, Density functional theory analysis of dopants in cupric oxide, *Journal of Applied Physics*, 111 (2012) 103708-103705.
- [6] A. Gurbani, J.L. Ayastuy, M.P. González-Marcos, M.A. Gutiérrez-Ortiz, CuO–CeO<sub>2</sub> catalysts synthesized by various methods: Comparative study of redox properties, *International Journal of Hydrogen Energy*, 35 (2010) 11582-11590.
- [7] P. Shao, S. Deng, J. Chen, J. Chen, N. Xu, Study of field emission, electrical transport, and their correlation of individual single CuO nanowires, *Journal of Applied Physics*, 109 (2011) 023710-023716.
- [8] B.K. Meyer, A. Polity, D. Reppin, M. Becker, P. Hering, P.J. Klar, T. Sander, C. Reindl, J. Benz, M. Eickhoff, C. Heiliger, M. Heinemann, J. Bläsing, A. Krost, S. Shokovets, C. Müller, C. Ronning, Binary copper oxide semiconductors: From materials towards devices, *physica status solidi (b)*, 249 (2012) 1487-1509.
- [9] F. Zhang, A. Zhu, Y. Luo, Y. Tian, J. Yang, Y. Qin, CuO Nanosheets for Sensitive and Selective Determination of H<sub>2</sub>S with High Recovery Ability, *The Journal of Physical Chemistry C*, 114 (2010) 19214-19219.
- [10] N.S. Ramgir, S.K. Ganapathi, M. Kaur, N. Datta, K.P. Muthe, D.K. Aswal, S.K. Gupta, J.V. Yakhmi, Sub-ppm H<sub>2</sub>S sensing at room temperature using CuO thin films, *Sensors and Actuators B: Chemical*, 151 (2010) 90-96.
- [11] M. Hübner, C.E. Simion, A. Tomescu-Stănoiu, S. Pokhrel, N. Bârsan, U. Weimar, Influence of humidity on CO sensing with p-type CuO thick film gas sensors, *Sensors and Actuators B: Chemical*, 153 (2011) 347-353.
- [12] X. Jiang, T. Herricks, Y. Xia, CuO Nanowires Can Be Synthesized by Heating Copper Substrates in Air, *Nano Letters*, 2 (2002) 1333-1338.
- [13] G. Filipič, U. Cvelbar, Copper oxide nanowires: a review of growth, *Nanotechnology*, 23 (2012) 194001.

- [14] X. Li, Y. Wang, Y. Lei, Z. Gu, Highly sensitive H<sub>2</sub>S sensor based on template-synthesized CuO nanowires, *RSC Advances*, 2 (2012) 2302-2307.
- [15] W. Wang, Z. Liu, Y. Liu, C. Xu, C. Zheng, G. Wang, A simple wet-chemical synthesis and characterization of CuO nanorods, *Appl Phys A*, 76 (2003) 417-420.
- [16] H. Wu, D. Lin, W. Pan, Fabrication, assembly, and electrical characterization of CuO nanofibers, *Applied Physics Letters*, 89 (2006) 133125-133123.
- [17] D. Zappa, E. Comini, R. Zamani, J. Arbiol, J.R. Morante, G. Sberveglieri, Preparation of copper oxide nanowire-based conductometric chemical sensors, *Sensors and Actuators B: Chemical*, 182 (2013) 7-15.
- [18] D.D. Li, J. Hu, R.Q. Wu, J.G. Lu, Conductometric Chemical Sensor based on Individual CuO Nanowires, *Nanotechnology*, 21 (2010) 485502.
- [19] L. Liao, Z. Zhang, B. Yan, Z. Zheng, Q.L. Bao, T. Wu, C.M. Li, Z.X. Shen, J.X. Zhang, H. Gong, J.C. Li, T. Yu, Multifunctional CuO nanowire devices: p-type field effect transistors and CO gas sensors, *Nanotechnology*, 20 (2009) 085203.
- [20] B.J. Hansen, N. Kouklin, G. Lu, I.K. Lin, J. Chen, X. Zhang, Transport, Analyte Detection, and Opto-Electronic Response of p-Type CuO Nanowires, *The Journal of Physical Chemistry C*, 114 (2010) 2440-2447.
- [21] C.Y. Huang, A. Chatterjee, S.B. Liu, S.Y. Wu, C.L. Cheng, Photoluminescence properties of a single tapered CuO nanowire, *Applied surface science*, 256 (2010) 3688-3692.
- [22] J. Chen, K. Wang, L. Hartman, W. Zhou, H<sub>2</sub>S Detection by Vertically Aligned CuO Nanowire Array Sensors, *J. Phys. Chem. C*, 112 (2008) 16017- 16021.
- [23] L. Yuan, Y. Wang, R. Mema, G. Zhou, Driving force and growth mechanism for spontaneous oxide nanowire formation during the thermal oxidation of metals, *Acta Materialia*, 59 (2011) 2491-2500.
- [24] ASM Handbook Volume 03: Alloy Phase Diagrams, ASM International, 1992.
- [25] A.M.B. Goncalves, L.C. Campos, A.S. Ferlauto, R.G. Lacerda, On the growth and electrical characterization of CuO nanowires by thermal oxidation, *Journal of Applied Physics*, 106 (2009) 034303-034305.
- [26] C. Shao-Liang, C. Ming-Feng, C. Cheng-Hsuan, Synthesis and growth kinetics of large-scale CuO nanowires grown by oxidation of Cu films, in: *Nanoelectronics Conference (INEC), 2011 IEEE 4th International*, 2011, pp. 1-2.
- [27] A. Parretta, M.K. Jayaraj, A. Di Nocera, S. Loreti, L. Quercia, A. Agati, Electrical and Optical Properties of Copper Oxide Films Prepared by Reactive RF Magnetron Sputtering, *physica status solidi (a)*, 155 (1996) 399-404.

- [28] F.H. Ramirez, A. Tarancon, O. Casals, J. Rodriguez, A. Romano-Rodriguez, J.R. Morante, S. Barth, S. Mathur, Y. Choi T, D. Poulidakos, V. Callegari, P.M. Nellen, Fabrication and Electrical Characterization of Circuits based on Individual Tin Oxide Nanowires, *Nanotechnology*, 17 (2006) 5577–5583.
- [29] R.K. Bedi, I. Singh, Room-Temperature Ammonia Sensor Based on Cationic Surfactant-Assisted Nanocrystalline CuO, *ACS Applied Materials & Interfaces*, 2 (2010) 1361-1368.
- [30] N. Barsan, U. Weimar, Conduction Model of Metal Oxide Gas Sensors, *J. Electroceram.*, 7 (2001) 143–167.
- [31] S. Steinhauer, E. Brunet, T. Maier, G.C. Mutinati, A. Köck, O. Freudenberg, C. Gspan, W. Grogger, A. Neuhold, R. Resel, Gas sensing properties of novel CuO nanowire devices, *Sensors and Actuators B: Chemical*.
- [32] I. Giebelhaus, E. Varechkina, T. Fischer, M. Rumyantseva, V. Ivanov, A. Gaskov, J.R. Morante, J. Arbiol, W. Tyrra, S. Mathur, One-dimensional CuO-SnO<sub>2</sub> p-n heterojunctions for enhanced detection of H<sub>2</sub>S, *Journal of Materials Chemistry A*, 1 (2013) 11261-11268.
- [33] J.D. Prades, A. Cirera, J.R. Morante, *Ab initio* calculations of NO<sub>2</sub> and SO<sub>2</sub> chemisorption onto non-polar ZnO surfaces, *Sensors and Actuators B: Chemical*, 142 (2009) 179-184.
- [34] J. Hu, D. Li, J.G. Lu, R. Wu, Effects on Electronic Properties of Molecule Adsorption on CuO Surfaces and Nanowires†, *The Journal of Physical Chemistry C*, 114 (2010) 17120-17126.
- [35] Y.-S. Kim, I.-S. Hwang, S.-J. Kim, C.-Y. Lee, J.-H. Lee, CuO nanowire gas sensors for air quality control in automotive cabin, *Sensors and Actuators B: Chemical*, 135 (2008) 298-303.
- [36] B. Ruhland, T. Becker, G. Müller, Gas-kinetic interactions of nitrous oxides with SnO<sub>2</sub> surfaces, *Sensors and Actuators B: Chemical*, 50 (1998) 85-94.

## **7. ZnO nanowire sensors based on micro hot plates and the NH<sub>3</sub> response in temperature-pulsed mode**

Micro Hot Plates ( $\mu$ HPs) provide new opportunities to improve the performance of MOX gas sensors by lowering the power consumption, enabling a fast thermal response and their small size, etc. However, the deposition of sensing materials onto the  $\mu$ HP surface remains as a challenge, especially when the sensing material is prepared in a separated process. And that is the side effect of their extremely small sizes ( $\sim 1\text{mm}$ ), which has also brought it with those advantages. In this chapter, we describe a facile method to deposit the solution prepared ZnO nanowires onto  $\mu$ HPs. Nanowires were successfully aligned between Inter Digital Electrodes (IDEs) by applying dielectrophoretic (DEP) forces. The NH<sub>3</sub> sensing performance of the resulting sensors was then examined in both conventional isothermal sensing mode and the temperature-pulsed sensing mode. When working in the temperature-pulsed mode, a significant enhancement of the NH<sub>3</sub> sensitivity was observed and the mechanism behind was discussed.

### **7.1 Introduction**

Micro hot plates based on standard CMOS (Complementary Metal Oxide Semiconductor) technology have the characteristics of low power consumption, high temperature capability with fast thermal response and they can be produced in high volume with low cost [1, 2]. Therefore is the ideal substrate for resistive MOX gas sensors. In addition, they are compatible with the integration of other functional electronics onto the same chip [3]. In these devices, IDEs are

usually patterned on a thin insulating membrane, in which the heating element is also implanted. The size of the whole device is often mm × mm and the dimensions of the IDEs are hundreds of microns.

Non-localized deposition techniques, such as sputtering [4, 5], evaporation [6], spray coating [7] or electro-spinning [8] have to be combined with lithography of a deposition window or alignment of shadow mask. Whereas localized deposition techniques that utilize the internal heater to activate the growth have to use the vapor phase precursors [1]. If the seed layer is required by the localized growth, the non-localized technique is again needed to realize the seed layer [9-11]. An alternative type of localized deposition technique is the direct deposition of sensing materials presented in fluid (solution) form to the micro hot plate surface by screen printing [12], micro droplet coating [13, 14] or ink-jet printing [15], which all require dedicated equipments and knowhow about the precursor preparation.

DEP technique has been widely used to manipulate nanomaterials [16-19], especially metallic [20] and semiconductor [18, 21] nanowires. The DEP force arises from the polarization of the non-charged subject in a non-uniform electric field and it attracts the subject to the electrodes. It was successfully applied to align nanowires onto ceramic based sensor substrates [20, 22], and it has been found to be fully compatible with the standard CMOS technology for wafer-scale implementation [23, 24].

In this chapter, the deposition of the sensing material onto  $\mu$ HPs to build gas sensors was further simplified by applying DEP alignment of ZnO nanowires at the post CMOS wafer stage. With this method, nanowires prepared from a wide range of methods can be readily integrated in sensing devices. The gas sensing performance of these prototypes was tested with NH<sub>3</sub> and CO

working in isothermal mode and with  $\text{NH}_3$  in temperature-pulsed mode. The mechanism behind the enhanced sensor response in the temperature-pulsed mode is also qualitatively discussed.

## **7.2 Results and discussion**

### **7.2.1 Self-assembly of nanowires onto $\mu\text{HPs}$**

The details about the  $\mu\text{HPs}$  used and the DEP deposition process are given in section 3.2.2. From the optical microscope images of figure 7.1a&b, we can see that most of the nanowires have been attracted to the IDEs after the DEP deposition while the rest of the membrane area remained relatively clean. The small amount of nanowires left on the membrane should not affect the overall performance of the device. As it can also be seen from figure 7.1a&b and figure 7.2, the edge area of the IDEs attracted more efficiently the nanowires, probably due to less potential interference than in the centre of the substrate where the multiple electrodes with opposite potential values are located very close to each other, which offset the polarization effect on the nanowires. SEM image in figure 7.3 shows that the length of the used nanowires is shorter than the gap between the IDEs, so that multiple nanowires are required to bridge the gap between the electrodes. Despite nanowires are finally interconnected to each other, some of them do not contribute to the measured resistance as they are not on the electrical path.

The contact between the semiconductor and metal can be either ohmic or rectifying. Ideally, ohmic contacts are formed with n-type semiconductors if the work function of the metal is close or smaller than the electron affinity of the semiconductor [25]. In our case, Au has a work function of  $5.1\pm 0.1\text{eV}$  [26] which is larger than the electron affinity of ZnO ( $\sim 4.2\text{eV}$ ) [25].

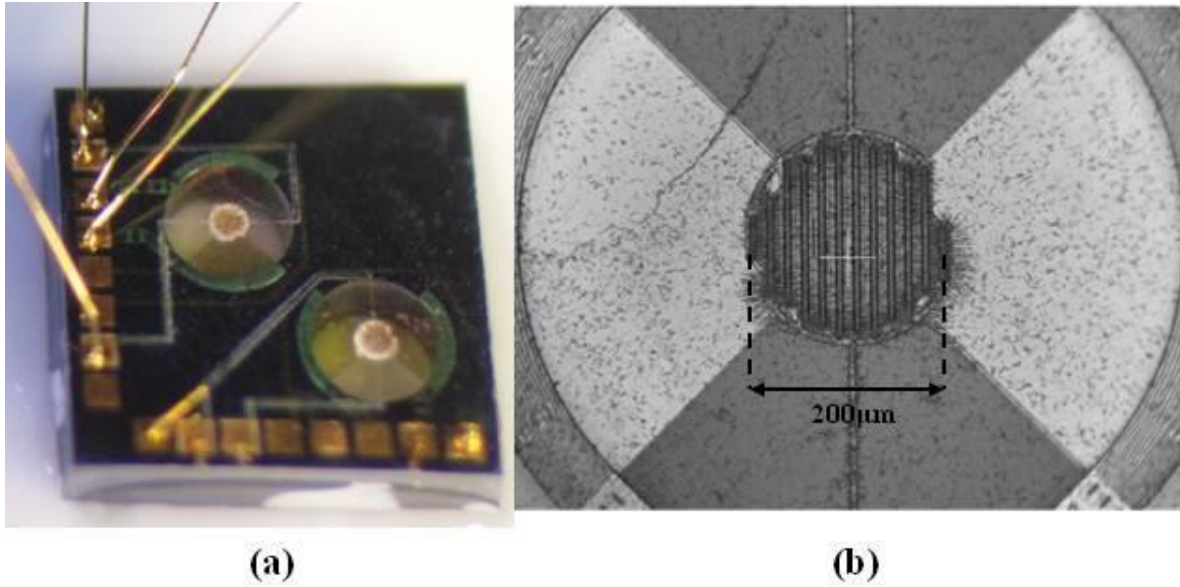


**Figure 7.1** (a) The  $\mu$ HP substrate after ZnO nanowire deposition and wire bonding (ZnO nanowires appear in white). (b) Optical microscope image of the membrane after nanowire deposition (in the center are the IDEs).

The room temperature (RT) I-V curve of the 400°C annealed device was non-linear (inset of figure 7.4), indicating the formation of the expected Schottky barrier at the Au-ZnO interface. As the temperature increases, both the current and linearity of the IV curve increased. By 200°C, the IV curve is almost linear and the contact resistance can be neglected. Further increasing of the annealing temperature up to 500°C had a negligible effect on the linearity of the IV curve, although as will be seen in the next section the gas sensing properties are quite different from the 400°C annealed.

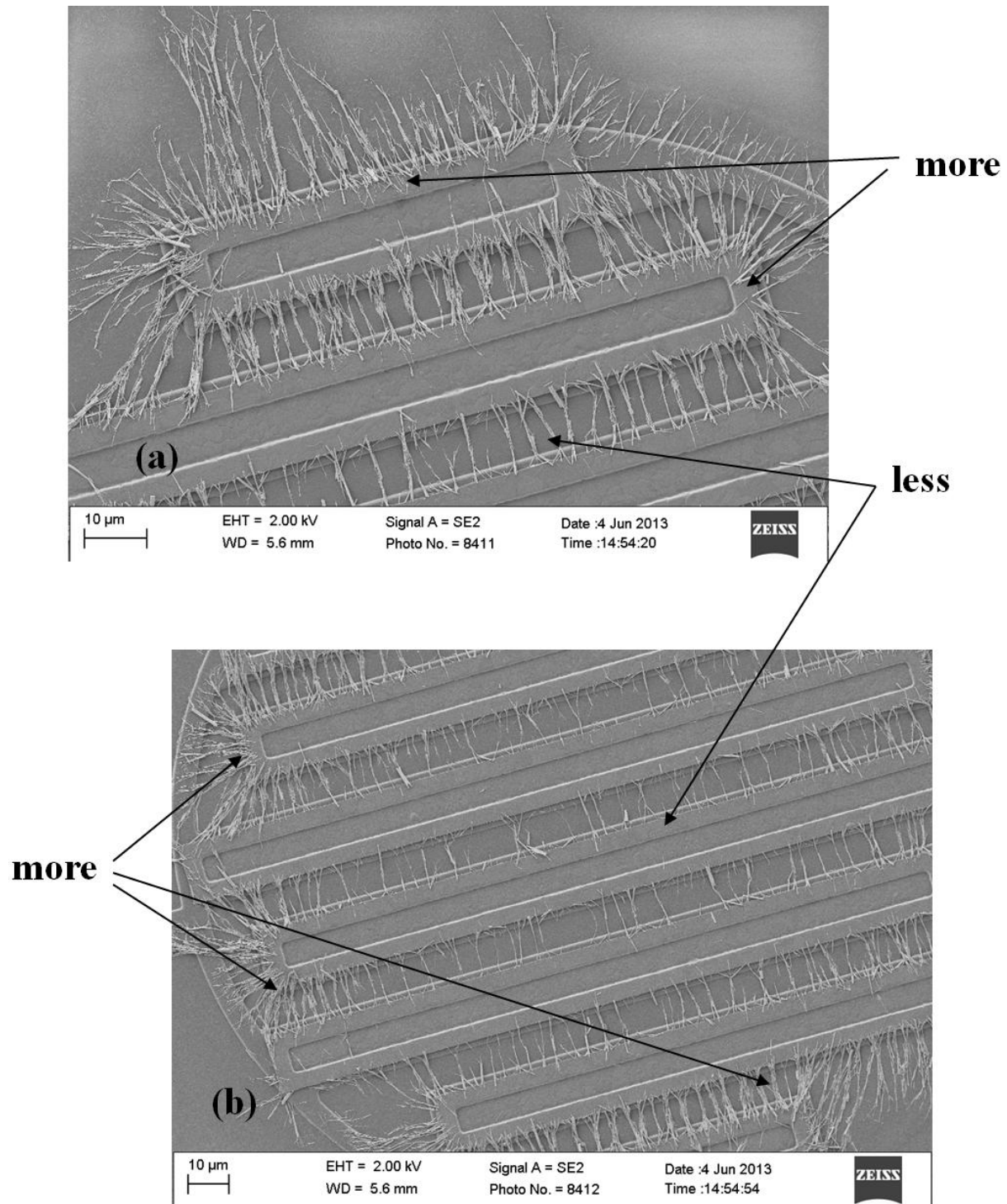


**Figure 7.2** SEM images showing that the edges of the IDEs attract more nanowires than the center.



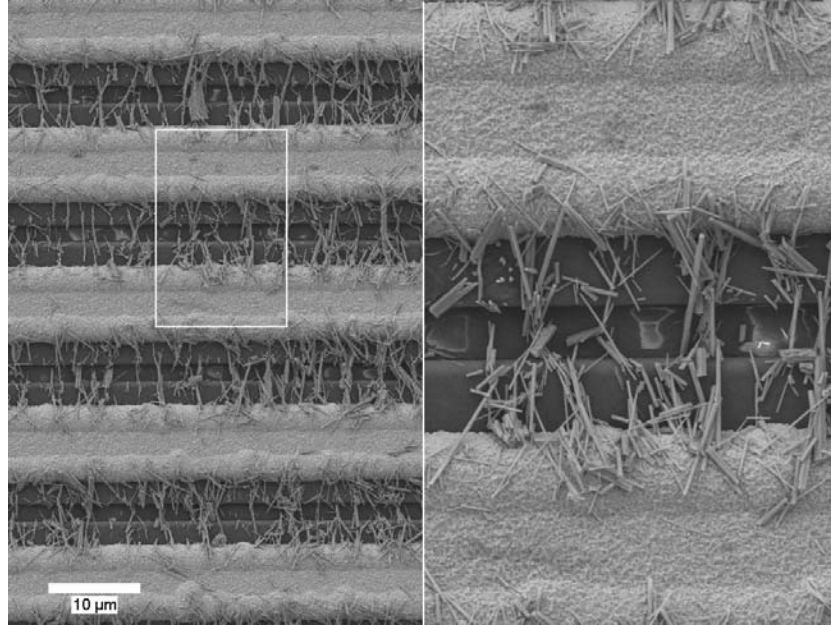


**Figure 7.3** SEM image showing nanowires assembled between the IDEs (The right half is the magnified image of the area in the white box on the left side).

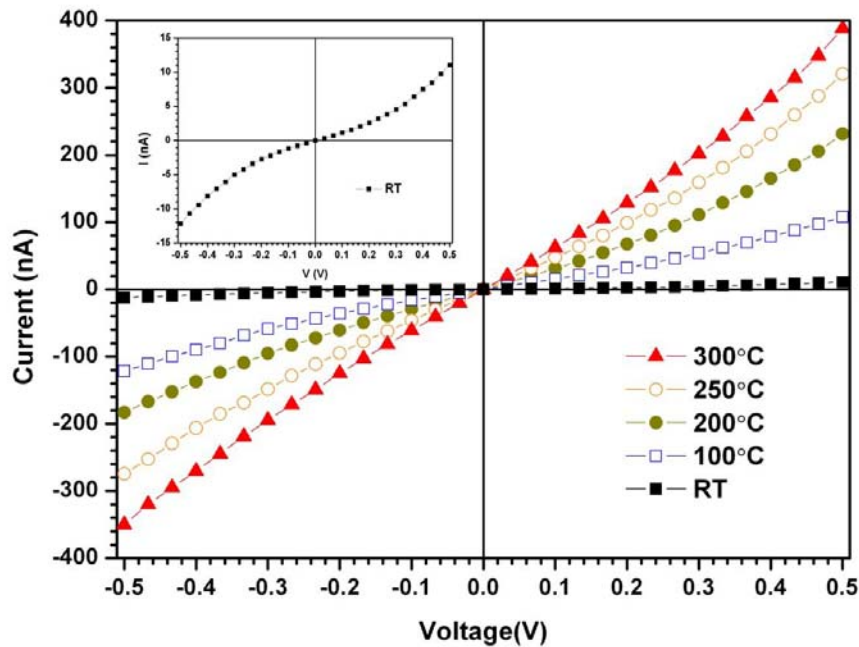


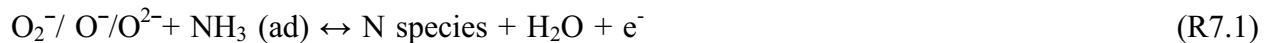
**Figure 7.4** IV curves of the annealed device at different temperatures, (inset) zoom in of the room temperature IV curve.

## 7.2.2 Gas sensing response of ZnO $\mu$ HP sensors

### *Isothermal mode*

NH<sub>3</sub> and CO sensing tests were performed at temperatures from 350°C to 200°C in isothermal mode. As shown in figure 7.5, the nanowire responded to NH<sub>3</sub> by decreasing the resistance and the change was reversible when NH<sub>3</sub> was purged. The decrease of resistance to NH<sub>3</sub> is expected as the ZnO is an n-type semiconductor and NH<sub>3</sub> is a reducing gas. For CO, only a small resistance variation was observed at 350°. No other response to CO was found at different temperatures (see figure 7.6). Again we define the sensitivity  $S$  to be  $R_{SA}/R_{gas}$ , where  $R_{SA}$  and  $R_{gas}$  is the resistance in dry SA and in gas mixture, respectively. Response/recovery time ( $t_{res}/t_{rec}$ ) is counted as the time it takes to complete 90% of the resistance changes. The optimal working temperature for NH<sub>3</sub> is found at around 300°C (figure 7.7). At this temperature, the response time is about 5min and the recovery time is generally a few minutes longer depending on the NH<sub>3</sub> concentration. Both response and recovery time are found to be shorter at higher temperatures.

The NH<sub>3</sub> sensing mechanism with ZnO nanowires is again explained using the classic conduction model [27] in MOXs: the surface oxygen species (molecular O<sub>2</sub><sup>-</sup> and atomic O<sup>-</sup>, O<sup>2-</sup>) withdraw electrons from the ZnO, creating a depletion layer that acts as a non conductive region at the surface or charge transfer barrier between nanowire junctions. When the NH<sub>3</sub> molecule is presented, surface reaction happens between the surface oxygen species and the NH<sub>3</sub> molecules. These complex surface reactions can be simplified by the following equation:



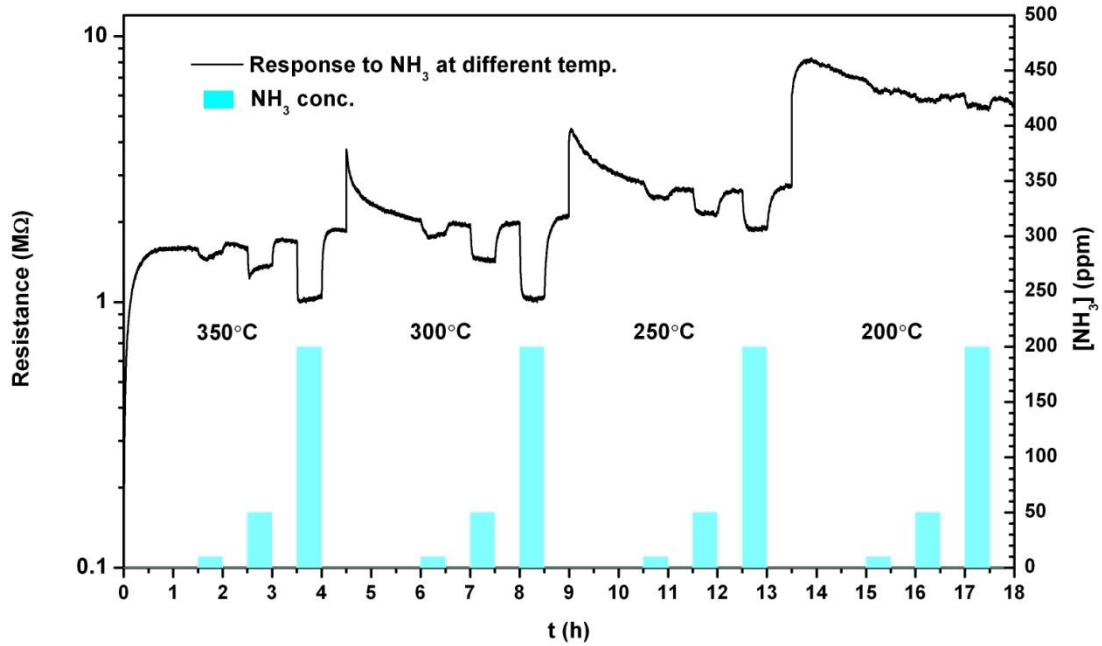


**Figure 7.5**  $\text{NH}_3$  sensing of the ZnO nanowire device in isothermal mode (400°C annealed), the baseline changed due to the change of working temperature.

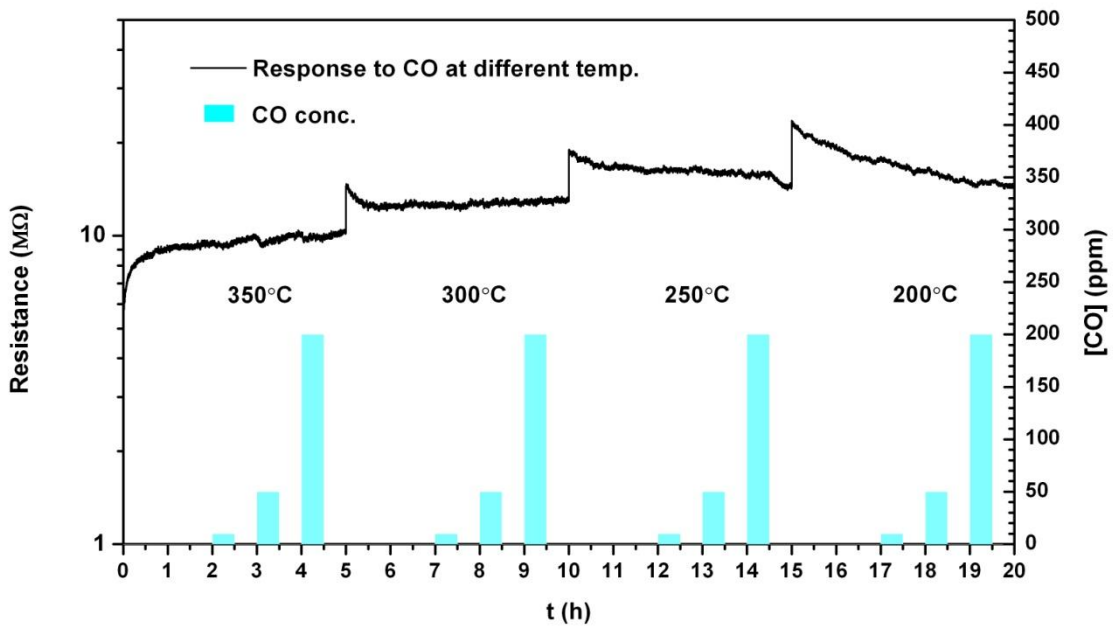


**Figure 7.6** CO sensing of the ZnO nanowire device in isothermal mode (400°C annealed).

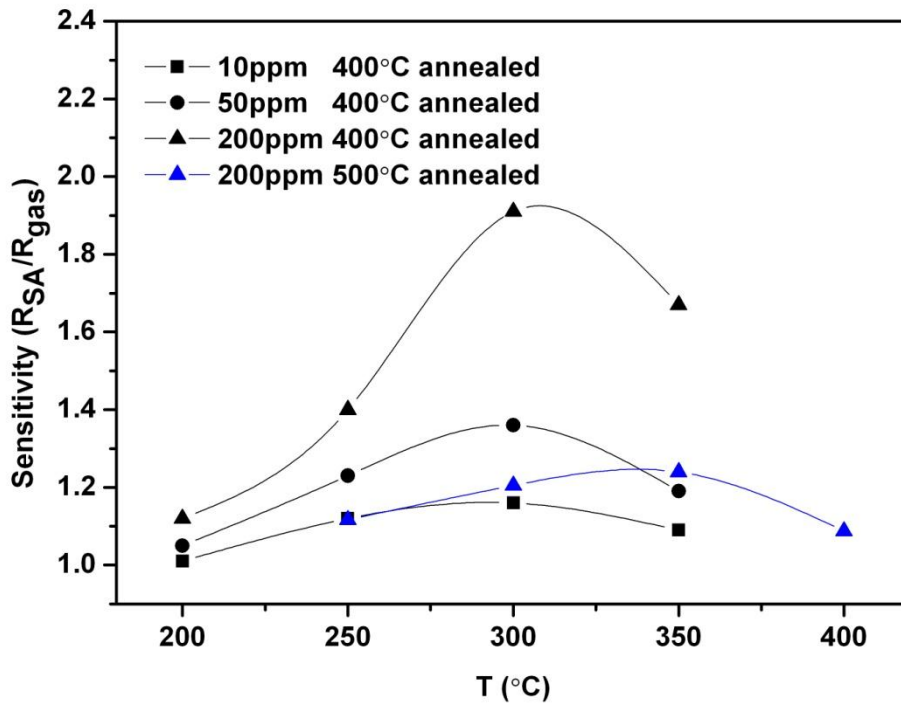


**Figure 7.7** Sensitivity vs. Temperature of ZnO to NH<sub>3</sub>.

Electrons are released by the surface reactions, decreasing the resistance of the ZnO. In figure 7.5, it can be noted that the resistance indeed showed upward shifting after a prior drop at the NH<sub>3</sub> response of 350°C and the 10ppm response of 300°C. Such character was ascribed to the generation of NO<sub>2</sub> in addition to N<sub>2</sub> as the reaction products. And NO<sub>2</sub> is considered to get adsorbed on the surface and withdraws electron [28-30].

On the other hand, relative NH<sub>3</sub> selectivity of ZnO from CO was also reported by Sekhar et al. [31]. And Ming [32] has shown that the CO and NH<sub>3</sub> relative sensitivity of ZnO thin film is dependent on the O concentration and annealing temperature.

With the annealing at 500°C, the NH<sub>3</sub> sensing response was deteriorated in two aspects: lowering of *S* and slower response (see figure 7.8). At the temperatures below 350°C, the analysis of *S* is less reliable as the resistance never stabilized during the 30min period of exposure to different gas mixtures. Nevertheless, the response to 200ppm NH<sub>3</sub> is also plotted in figure 7.7 to compare with the 400°C annealed device. The CO response is more visible at higher temperatures but remains to be negligible comparing to NH<sub>3</sub>. The deterioration of NH<sub>3</sub> sensing response indicates the change of ZnO properties with higher annealing temperature, which might have changed the surface oxygen vacancy density by oxygen incorporation. So the experiments will be described in the coming section were carried out with the 400°C annealed devices.

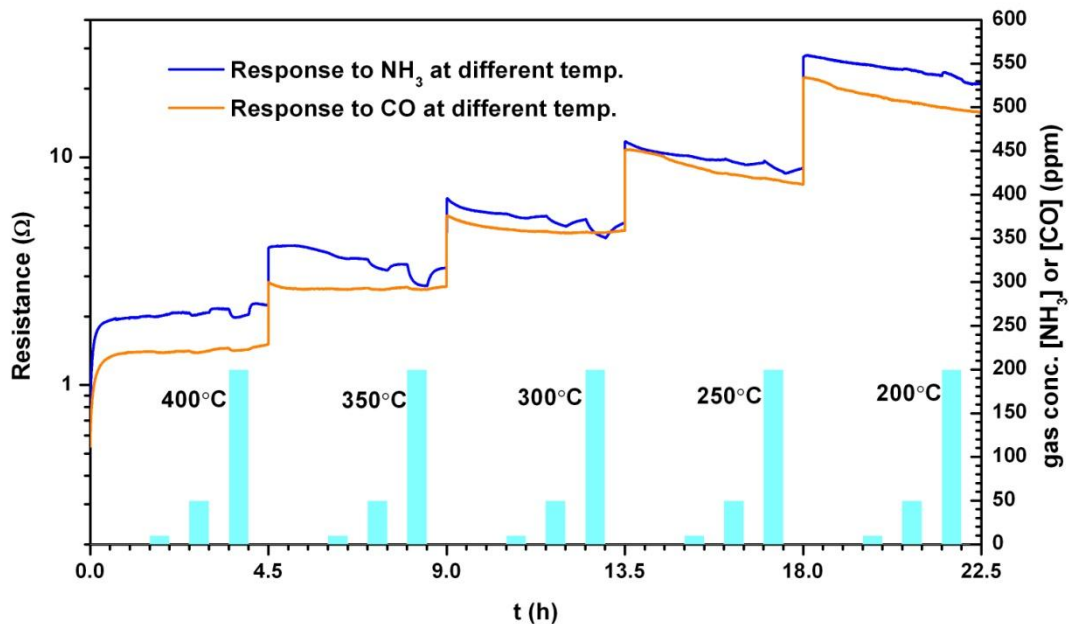


**Figure 7.8** NH<sub>3</sub> and CO sensing of the ZnO nanowire device in isothermal mode (500°C annealed).

### ***Temperature-pulsed mode***

$\mu$ HP based MOX gas sensor is often investigated under the temperature-programmed/modulated operation mode [30, 33-36], in which the sensor is subjected to pulses of different temperatures and duration instead of keeping the temperature fixed at a constant value. By this way, selectivity and even quantification [37, 38] can be achieved by pattern reading and data analysis. The approach we applied here is a variant of the temperature-programmed/modulated method, and it will be termed as temperature-pulsed operation mode. In this methodology, the temperature of the sensor was constantly changed between two temperatures every few seconds, e.g., 5s, while the resistance of the nanowires was recorded when the gas flow was changed from pure SA to 200ppm NH<sub>3</sub> in SA and then purged again with SA flux.

As shown in the figure 7.9a-c, when the sensor was operated in the temperature-pulsed mode, a significant enhancement of sensitivity comparing to the isothermal mode was observed at the low temperature end of the resistance, while it was almost identical at the high temperatures. A comparison of sensitivities is given in figure 7.10. It can be seen that the relative increase of sensitivity, calculated as  $\Delta S = (S_{low,pulsed} - S_{iso})/S_{iso} * 100\%$ , is larger when the low and high temperature difference in the pulsed mode is larger, i.e., the 250/400°C pulsed. Here  $S_{low,pulsed}$  is defined as the low temperature end sensitivity in pulsed mode operation and  $S_{iso}$  is the sensitivity in corresponding isothermal operation, respectively. In addition, nearly same  $S_{low,pulsed}$  are seen at the 250/400°C and 300/400°C pulsed mode operations. This indicates that  $S_{low,pulsed}$  is dominated by the effect of the high temperature regime in this working mode.

From figure 7.9a-c we can also see that the low temperature end resistance in the temperature-pulsed mode is higher than those at the same temperature but in the isothermal mode, whereas it

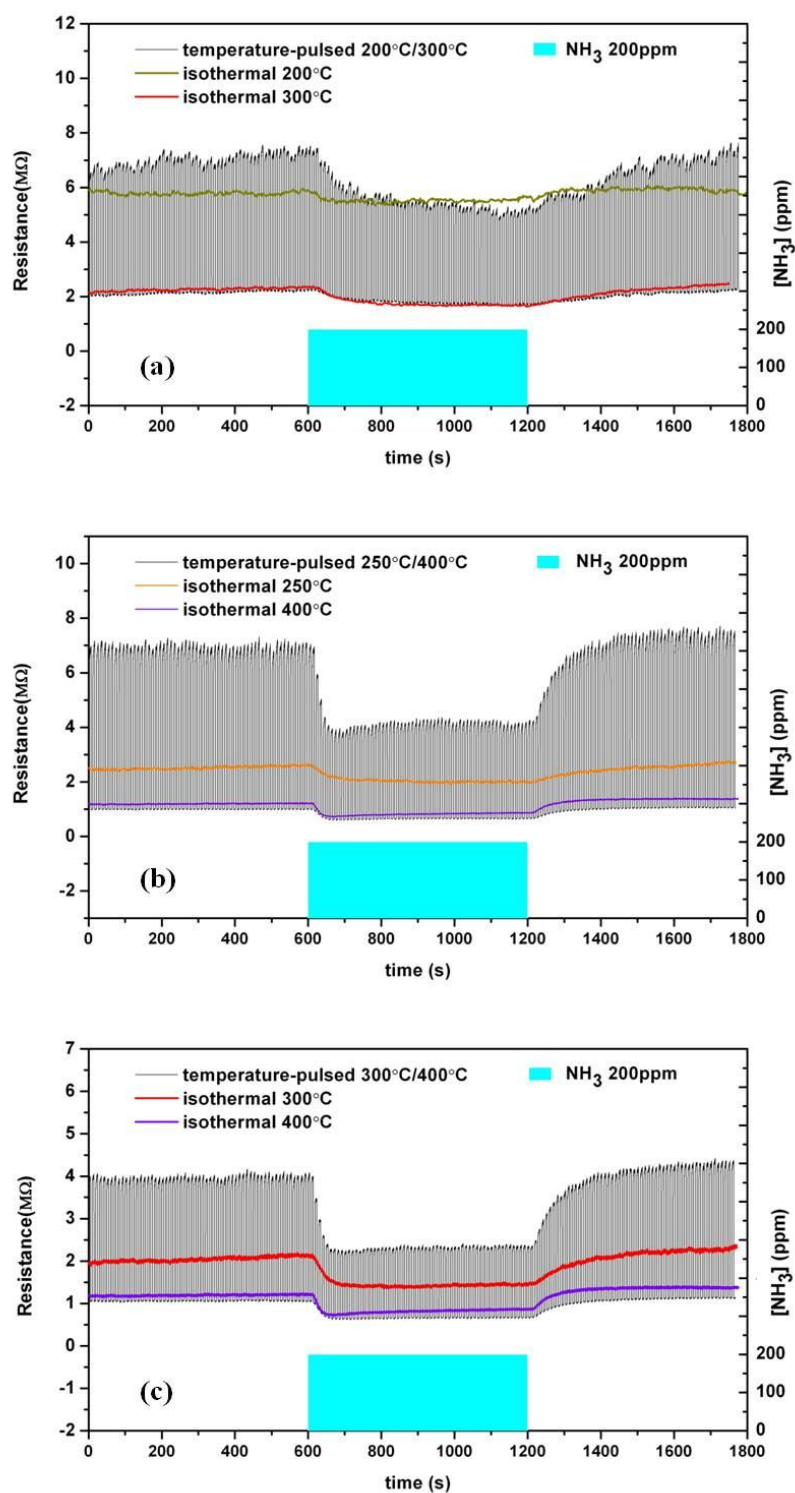


**Figure 7.9** Temperature-pulsed and isothermal sensing of 200ppm NH<sub>3</sub>. (a) 200-300°C, (b) 250-400°C, (c) 300-400°C.

is almost identical in the high temperature side. This indicates that the pulsed mode operation influences the nanowires' resistance mainly at the low temperature end. This behavior matches with just presented sensitivity enhancement preference.

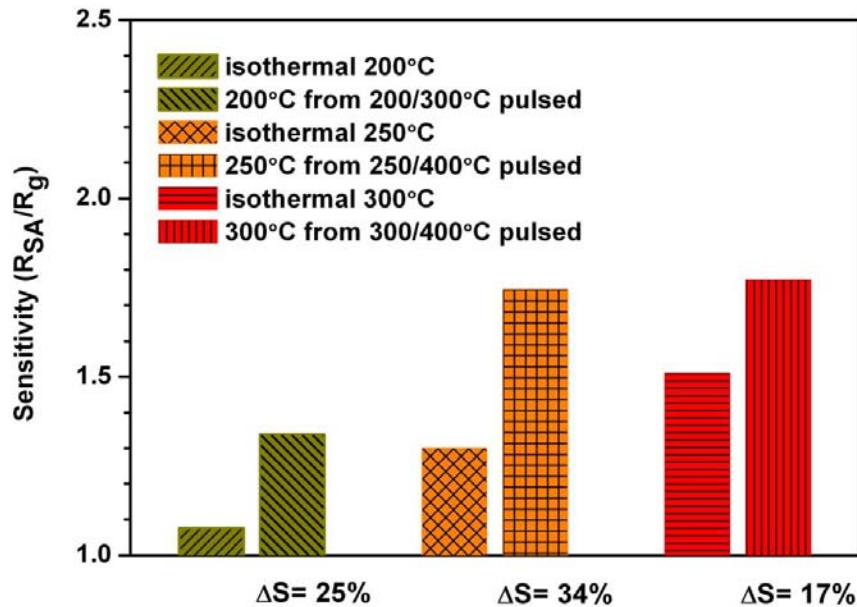


**Figure 7.10** Comparison of sensitivity from isothermal and temperature-pulsed sensing (200ppm  $\text{NH}_3$ ).

Similar sensitivity enhancement effects in the temperature-pulsed mode operation has been previously reported in several works [14, 37, 39, 40]. As the surface oxygen species play a key role in the sensing mechanism of reducing species, Heilig et al. [37], proposed that the improvement is originated by the presence of high temperature surface oxygen species, i.e.,  $\text{O}^-/\text{O}^{2-}$  [27] in the low temperature period, which are not or less present in the isothermal mode at this temperature.  $\text{O}^-/\text{O}^{2-}$  is produced after the dissociation [41] of surface adsorbed molecular



oxygen at high temperatures and remains there in the low temperature period due to the fast thermal transition induced by the  $\mu$ HP. They strongly regulate the electron concentration near the surface and when surface reaction with the reducing molecules, e.g.,  $\text{NH}_3$  takes place, electrons are then released back to the surface causing the larger resistance change.

As mentioned in refs. [14] and [36], the surface cleaning effect of the high temperature period could also be the reason behind the sensitivity enhancement. Here, for the  $\text{NH}_3$  sensing with ZnO nanowires, we propose two potential adsorbates that can deteriorate the sensitivity of the sensor in isothermal mode and be removed at high temperature cycling; the first is  $\text{H}_2\text{O}$  and its byproduct, hydroxyl group (OH).  $\text{H}_2\text{O}$  is a well known substance that interferes in the response of MOX sensors [31, 42]. There are three sources of  $\text{H}_2\text{O}$  that can be adsorbed onto ZnO surface: i) when the sensor was initially exposed to ambient air at RT; ii) and residual  $\text{H}_2\text{O}$  that presented in the test chamber; iii) trace levels of  $\text{H}_2\text{O}$  present in the SA.

The second one is  $\text{NO}_2$ , which was considered to be a secondary product of oxygen- $\text{NH}_3$  reaction at the MOX surface and has a counter effect to the  $\text{NH}_3$  response [28-30]. The sign of  $\text{NO}_2$  generation has also been presented in the previous section. It is therefore concluded that when operated in the temperature-pulsed mode, the amount of  $\text{H}_2\text{O}/\text{-OH}$  and  $\text{NO}_2$  can be diminished by the high temperature cycling, exposing the surface active site for  $\text{O}_2$  and  $\text{NH}_3$  in low temperature period. In overall, these contributions lead to the higher sensitivity that is experimentally observed.

Figure 7.12 shows, in a shorter time scale, the resistance of the device working in temperature-pulsed mode between 250 and 400°C in constant SA flow. The low temperature end resistance is found to be continuously increasing, indicating the material is in a meta-stable state. The

opposite happens at the high temperature end as the resistance is rather stable. The meta-stable state character of the low temperature end is indirect evidence to the as proposed mechanism of sensitivity enhancement due to high temperature surface oxygen species as it creates meta-stable state on the surface.

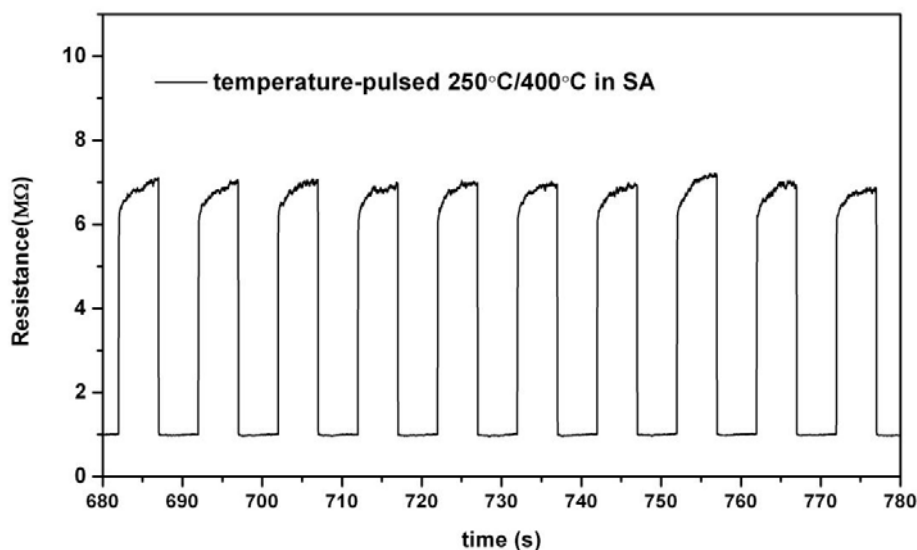


**Figure 7.12** Resistance of the nanowires in temperature-pulsed mode.

### 7.3 Conclusions

A facile method was used to deposit ZnO nanowires onto  $\mu$ HP substrates. The contacts between the ZnO and Au became ohmic at elevated temperatures enabling the electrical measurements. Relative selectivity of ZnO nanowire toward  $\text{NH}_3$  from CO was found in the isothermal sensing mode and could be ascribed to the intrinsic surface/bulk properties of ZnO. Annealing at  $500^\circ\text{C}$  was found to deteriorate the  $\text{NH}_3$  sensing performance. When working in the temperature-pulsed mode, a significant enhancement in the  $\text{NH}_3$  sensitivity was obtained in the low temperature end.

It was concluded that the enhancement is not only related to the different surface oxygen species due to the temperature modulation but also caused by the modulation of H<sub>2</sub>O and NO<sub>2</sub> populations on the surface.

## References

- [1] S. Semancik, R.E. Cavicchi, M.C. Wheeler, J.E. Tiffany, G.E. Poirier, R.M. Walton, J.S. Suehle, B. Panchapakesan, D.L. DeVoe, Microhotplate platforms for chemical sensor research, *Sensors and Actuators B: Chemical*, 77 (2001) 579-591.
- [2] M. Graf, A. Gurlo, N. Bârsan, U. Weimar, A. Hierlemann, Microfabricated gas sensor systems with sensitive nanocrystalline metal-oxide films, *Journal of Nanoparticle Research*, 8 (2006) 823-839.
- [3] D. Barrettino, M. Graf, M. Zimmermann, C. Hagleitner, A. Hierlemann, H. Baltes, A Smart Single-Chip Micro-Hotplate-Based Gas Sensor System in CMOS-Technology, *Analog Integrated Circuits and Signal Processing*, 39 (2004) 275-287.
- [4] J. Wöllenstein, J.A. Plaza, C. Cané, Y. Min, H. Böttner, H.L. Tuller, A novel single chip thin film metal oxide array, *Sensors and Actuators B: Chemical*, 93 (2003) 350-355.
- [5] M. Stankova, X. Vilanova, J. Calderer, E. Llobet, J. Brezmes, I. Gràcia, C. Cané, X. Correig, Sensitivity and selectivity improvement of rf sputtered WO<sub>3</sub> microhotplate gas sensors, *Sensors and Actuators B: Chemical*, 113 (2006) 241-248.
- [6] A. Friedberger, P. Kreisl, E. Rose, G. Müller, G. Kühner, J. Wöllenstein, H. Böttner, Micromechanical fabrication of robust low-power metal oxide gas sensors, *Sensors and Actuators B: Chemical*, 93 (2003) 345-349.
- [7] I. Jiménez, A. Cirera, A. Cornet, J.R. Morante, I. Gracia, C. Cané, Pulverisation method for active layer coating on microsystems, *Sensors and Actuators B: Chemical*, 84 (2002) 78-82.
- [8] Y. Zhao, X. He, J. Li, X. Gao, J. Jia, Porous CuO/SnO<sub>2</sub> composite nanofibers fabricated by electrospinning and their H<sub>2</sub>S sensing properties, *Sensors and Actuators B: Chemical*, 165 (2012) 82-87.
- [9] S. Sumita, Z.A. Syed, K.G. Prasanta, Z. Guofang, R. John, A.C. James, I.M. William, W.G. Julian, U. Florin, Post-CMOS wafer level growth of carbon nanotubes for low-cost microsensors—a proof of concept, *Nanotechnology*, 21 (2010) 485301.
- [10] S. Barth, R. Jimenez-Diaz, J. Sama, J. Daniel Prades, I. Gracia, J. Santander, C. Cane, A. Romano-Rodriguez, Localized growth and in situ integration of nanowires for device applications, *Chemical Communications*, 48 (2012) 4734-4736.
- [11] S. Santra, P.K. Guha, S.Z. Ali, P. Hiralal, H.E. Unalan, J.A. Covington, G.A.J. Amaratunga, W.I. Milne, J.W. Gardner, F. Udrea, ZnO nanowires grown on SOI CMOS substrate for ethanol sensing, *Sensors and Actuators B: Chemical*, 146 (2010) 559-565.
- [12] E. Llobet, P. Ivanov, X. Vilanova, J. Brezmes, J. Hubalek, K. Malysz, I. Gràcia, C. Cané, X. Correig, Screen-printed nanoparticle tin oxide films for high-yield sensor microsystems, *Sensors and Actuators B: Chemical*, 96 (2003) 94-104.

- [13] J. Puigcorb , A. Cirera, J. Cerd , J. Folch, A. Cornet, J.R. Morante, Microdeposition of microwave obtained nanoscaled SnO<sub>2</sub> powders for gas sensing microsystems, *Sensors and Actuators B: Chemical*, 84 (2002) 60-65.
- [14] A.M. Ruiz, X. Illa, R. D az, A. Romano-Rodr guez, J.R. Morante, Analyses of the ammonia response of integrated gas sensors working in pulsed mode, *Sensors and Actuators B: Chemical*, 118 (2006) 318-322.
- [15] M.A. Andio, P.N. Browning, P.A. Morris, S.A. Akbar, Comparison of gas sensor performance of SnO<sub>2</sub> nano-structures on microhotplate platforms, *Sensors and Actuators B: Chemical*, 165 (2012) 13-18.
- [16] H.Y. Yu, B.H. Kang, U.H. Pi, C.W. Park, S.-Y. Choi, G.T. Kim, V<sub>2</sub>O<sub>5</sub> nanowire-based nanoelectronic devices for helium detection, *Applied Physics Letters*, 86 (2005) 253102-253103.
- [17] A.W. Maijenburg, M.G. Maas, E.J.B. Rodijk, W. Ahmed, E.S. Kooij, E.T. Carlen, D.H.A. Blank, J.E. ten Elshof, Dielectrophoretic alignment of metal and metal oxide nanowires and nanotubes: A universal set of parameters for bridging prepatterned microelectrodes, *Journal of Colloid and Interface Science*, 355 (2011) 486-493.
- [18] C.S. Lao, J. Liu, P. Gao, L. Zhang, D. Davidovic, R. Tummala, Z.L. Wang, ZnO Nanobelt/Nanowire Schottky Diodes Formed by Dielectrophoresis Alignment across Au Electrodes, *Nano Letters*, 6 (2006) 263-266.
- [19] E.M. Freer, O. Grachev, X. Duan, S. Martin, D.P. Stumbo, High-yield self-limiting single-nanowire assembly with dielectrophoresis, *Nat Nano*, 5 (2010) 525-530.
- [20] X. Li, Y. Wang, Y. Lei, Z. Gu, Highly sensitive H<sub>2</sub>S sensor based on template-synthesized CuO nanowires, *RSC Advances*, 2 (2012) 2302-2307.
- [21] C. Leiterer, G. Broenstrup, N. Jahr, M. Urban, C. Arnold, S. Christiansen, W. Fritzsche, Applying contact to individual silicon nanowires using a dielectrophoresis (DEP)-based technique, *Journal of Nanoparticle Research*, 15 (2013) 1-7.
- [22] X. Li, Z. Gu, J. Cho, H. Sun, P. Kurup, Tin-copper mixed metal oxide nanowires: Synthesis and sensor response to chemical vapors, *Sensors and Actuators B: Chemical*, 158 (2011) 199-207.
- [23] A.H. Monica, S.J. Papadakis, R. Osiander, M. Paranjape, Wafer-level assembly of carbon nanotube networks using dielectrophoresis, *Nanotechnology*, 19 (2008) 085303.
- [24] S. Evoy, N. DiLello, V. Deshpande, A. Narayanan, H. Liu, M. Riegelman, B.R. Martin, B. Hailer, J.C. Bradley, W. Weiss, T.S. Mayer, Y. Gogotsi, H.H. Bau, T.E. Mallouk, S. Raman, Dielectrophoretic assembly and integration of nanowire devices with functional CMOS operating circuitry, *Microelectronic Engineering*, 75 (2004) 31-42.
- [25] L.J. Brillson, Y. Lu, ZnO Schottky barriers and Ohmic contacts, *Journal of Applied Physics*, 109 (2011) 121301-121333.

- [26] D.E. Eastman, Photoelectric Work Functions of Transition, Rare-Earth, and Noble Metals, *Physical Review B*, 2 (1970) 1-2.
- [27] N. Barsan, U. Weimar, Conduction Model of Metal Oxide Gas Sensors, *J. Electroceram.*, 7 (2001) 143–167.
- [28] I. Jimenez, M.A. Centeno, R. Scotti, F. Morazzoni, A. cornet, NH<sub>3</sub> Interaction with Catalytically Modified Nano WO<sub>3</sub> Poders for Gas Sensing Applications, *J. Electro. Chem. Soc.*, 150 (2003) 72–80.
- [29] Y. Shimizu, T. Okamoto, Y. Takao, M. Egashira, Desorption Behavior of Ammonia from TiO<sub>2</sub> based Specimens -Ammonia Sensing Mechanism of Double Layer Sensors with TiO<sub>2</sub> based Catalyst Layers, *J. Mol. Catal. A: Chem.*, 155 (2000) 183–191.
- [30] C. Bur, P. Reimann, A. Schutze, M. Andersson, A.L. Spetz, Increasing the selectivity of Pt-gate SiC field effect gas sensors by dynamic temperature modulation, in: *Sensors, 2010 IEEE*, 2010, pp. 1267-1272.
- [31] R. Chandra Sekhar, H. Manu, A. Govindaraj, C.N.R. Rao, Ammonia sensors based on metal oxide nanostructures, *Nanotechnology*, 18 (2007) 205504.
- [32] Y. Ming, Properties and sensor performance of zinc oxide thin films, in: *Dept. of Materials Science and Engineering, Massachusetts Institute of Technology*, 2003.
- [33] R.E. Cavicchi, J.S. Suehle, K.G. Kreider, M. Gaitan, P. Chaparala, Fast temperature programmed sensing for micro-hotplate gas sensors, *Electron Device Letters, IEEE*, 16 (1995) 286-288.
- [34] K.D. Benkstein, B. Raman, D.L. Lahr, J.E. Bonevich, S. Semancik, Inducing analytical orthogonality in tungsten oxide-based microsensors using materials structure and dynamic temperature control, *Sensors and Actuators B: Chemical*, 137 (2009) 48-55.
- [35] D.C. Meier, J.K. Evju, Z. Boger, B. Raman, K.D. Benkstein, C.J. Martinez, C.B. Montgomery, S. Semancik, The potential for and challenges of detecting chemical hazards with temperature-programmed microsensors, *Sensors and Actuators B: Chemical*, 121 (2007) 282-294.
- [36] A.P. Lee, B.J. Reedy, Temperature modulation in semiconductor gas sensing, *Sensors and Actuators B: Chemical*, 60 (1999) 35-42.
- [37] A. Heilig, N. Bârsan, U. Weimar, M. Schweizer-Berberich, J.W. Gardner, W. Göpel, Gas identification by modulating temperatures of SnO<sub>2</sub>-based thick film sensors, *Sensors and Actuators B: Chemical*, 43 (1997) 45-51.
- [38] R. Gosangi, R. Gutierrez-Osuna, Active temperature modulation of metal-oxide sensors for quantitative analysis of gas mixtures, *Sensors and Actuators B: Chemical*, 185 (2013) 201-210.
- [39] M. Jaegle, J. Wöllenstein, T. Meisinger, H. Böttner, G. Müller, T. Becker, C. Bosch-v.Braunmühl, Micromachined thin film SnO<sub>2</sub> gas sensors in temperature-pulsed operation mode, *Sensors and Actuators B: Chemical*, 57 (1999) 130-134.

[40] M. Schweizer-Berberich, S. Strathmann, U. Weimar, R. Sharma, A. Seube, A. Peyre-Lavigne, W. Göpel, Strategies to avoid VOC cross-sensitivity of SnO<sub>2</sub>-based CO sensors, *Sensors and Actuators B: Chemical*, 58 (1999) 318-324.

[41] J. Oviedo, M.J. Gillan, First-principles study of the interaction of oxygen with the SnO<sub>2</sub> (110) surface, *Surf. Sci.*, (2001) 221–236.

[42] F.H. Ramirez, S. Barth, A. Tاراcon, O. Casals, E. Pellicer, J. Rodriguez, A.R. Rodriguez, J.R. Morante, S. Mathur, Water Vapor Detection with Individual Tin Oxide Nanowires, *Nanotechnology*, 18 (2007) 424016.

## 8. Conclusions and future work

### 8.1 Conclusions

This PhD dissertation spans a broad range of research activities throughout the preparation, characterization, DFT modeling and optimization of MOX nanowire based gas sensors. Combination of theoretical and experimental methods was applied to the conventional n-type material SnO<sub>2</sub>. Explorations of new sensing materials, i.e., CuO@SnO<sub>2</sub> heterostructure, p-type CuO were combined with *ex-situ* analysis of the tested devices. The use of  $\mu$ HP based sensor in novel working mode has brought new features to nanowire-based sensors. In overall, surface O species were found to be the origin and most critical factor of gas sensing with MOXs. The special case is when the CuO@SnO<sub>2</sub> heterostructure was used for H<sub>2</sub>S sensing. Those findings of each chapter are given below.

SnO<sub>2</sub> nanowire in individual configuration showed moderate sensitivity to NH<sub>3</sub> and that was further lowered due to the interference of H<sub>2</sub>O. DFT calculations had drawn two surface reaction routines for the SnO<sub>2</sub>-NH<sub>3</sub> interaction. The one with the surface adsorbed O<sub>ads</sub> atom was found to be the preferable one as the energy barriers for dehydrogenation of the first two H atoms are lower and the computed rate limiting energy barrier can be correlated to the empirical modeling of experimental response time. The interference of H<sub>2</sub>O was also explained by DFT in terms of its competitive adsorption against NH<sub>3</sub> and the reverse kinetic effect of it on NH<sub>3</sub> dehydrogenation.

The CuO@SnO<sub>2</sub> heterostructure nanowire showed gas specific sensitivity enhancement toward H<sub>2</sub>S. The charge transport channel depletion model suited well to explain the behavior and was



supported by the *ex-situ* EDS analysis. It is the gas specific reaction between CuO and H<sub>2</sub>S causing the formation of metallic CuS and vanishes of the depletion layer at the otherwise p-n junction finally leading to the large amplitude variation of the resistance.

In the case of p-type CuO nanowire, the dominant role of surface O was concluded for all three gases tested, i.e., NH<sub>3</sub>, H<sub>2</sub>S and NO<sub>2</sub> from their resistance change tendency after exposure. While the NH<sub>3</sub> response matches with previous electron injection consideration of SnO<sub>2</sub> nanowire. The H<sub>2</sub>S response did not follow the sulfurization process proposed for the CuO particles in CuO@SnO<sub>2</sub> nanowires. This difference was ascribed to different property of these two kinds of CuO materials. More radical conclusion had to be made for the upward change of resistance to NO<sub>2</sub>. Surface adsorbed O species has to be included to explain the experimental responses in low concentration NO<sub>2</sub> tests.

DEP assembly has been proven to be a promising method to deposit MOX nanowires onto the  $\mu$ HP. Indeed, this approach will not be limited by the shape or electronic property of the material. For example, metallic nanowire could also be assembled with the DEP process. On the other hand, the relative selectivity of ZnO nanowires toward NH<sub>3</sub> from CO was ascribed to the ZnO's intrinsic surface/bulk properties. Finally, new features were found when the  $\mu$ HP sensors were operated in the temperature-pulsed mode. The enhanced sensitivity at the low temperature end was concluded to be the result of surface O/H<sub>2</sub>O/NO<sub>2</sub> modulation effects by the fast temperature transitions.

## 8.2 Future work

To achieve the ultimate modeling of MOX gas sensors, the modeling of surface processes by DFT has to be connected with the modeling of surface/bulk charge transport properties. What can be provided by DFT are not only the surface reaction routines, but also the charge difference, band changes, etc. Although many efforts have been done, the charge transport property modeling however relies on solid knowledge of semiconductor physics, which is in a different discipline from DFT. Therefore, finding a linking point between these two approaches is not only rewarding but also challenging.

Hybrid materials by doping or mixing are always topics of material engineering. Similar to the CuO@SnO<sub>2</sub> heterostructure presented here, NiO@SnO<sub>2</sub> heterostructures have been reported to show the same sensing character to H<sub>2</sub>S. This further proves the selective sulfurization reaction of H<sub>2</sub>S is a feature that can be utilized for designing sensitive and selective H<sub>2</sub>S sensors. Must be pointed out however is the concern about the stability of this type of materials for repetitive operation. For this, *in-situ* TEM might be the right technique to study it. More recently, using an organic molecule to sensitize the MOX to achieve high sensitivity and selectivity has been reported. It appears to be a new type of hybrid material with promising future.

The ZnO nanowires in the last chapter showed interesting NH<sub>3</sub> selectivity toward CO and deterioration of sensitivity after 500°C annealing. The exact cause still waits for further investigations. On the other hand, μHP sensor showed interesting features when working in the temperature-pulsed mode. These features however have not been thoroughly studied yet. Those parameters can be manipulated include: longer or shorter pulse period, different temperature combinations, etc. Working on those will consolidate our understanding about this technique.



# Short CV

Name: Feng Shao

Date of birth: 08-08-1984

Country: China

E-mail: fengshao@irec.cat

## **Education history:**

March 2010 - current

University of Barcelona, Spain

Doctor program in Engineering and Advanced Technologies

PhD fellowship at the Catalonia Institute of Energy Research

Jan 2009 - Aug 2009

Uppsala University, Sweden

Master thesis on dye sensitized solar cells

Aug 2007- Dec 2009

Royal Institute of Technology, Sweden

Msc in Nanotechnology

Aug 2006 - Aug 2007

Dalarna University College, Sweden

Master of Solar energy engineering

Sep 2002 - Jun 2006

Nanjing University of Aeronautics and Astronautics, China

BSc in Applied chemistry

**Lab skills:**

Frequent user: focused ion beam/electron beam system, SEM/EDS, sourcemeter, gas sensing system.

Former user: Electro-spinning deposition, ink-jet printing, AFM, XRD, XPS, UV-Vis, probe-station, impedance spectroscopy, dye sensitized solar cells fabrication and characterization.

DFT code: VASP

**Journal publication:**

[1] F. Shao, M.W.G. Hoffmann, J.D. Prades, J.R. Morante, N. López, F. Hernández-Ramírez, Interaction Mechanisms of Ammonia and Tin Oxide: A Combined Analysis Using Single Nanowire Devices and DFT Calculations, *The Journal of Physical Chemistry C*, 117 (2013) 3520-3526.

[2] F. Shao, M.W.G. Hoffmann, J.D. Prades, R. Zamani, J. Arbiol, J.R. Morante, E. Varechkina, M. Rumyantseva, A. Gaskov, I. Giebelhaus, T. Fischer, S. Mathur, F. Hernández-Ramírez, Heterostructured p-CuO (Nanoparticle)/n-SnO<sub>2</sub> (Nanowire) Devices for Selective H<sub>2</sub>S Detection, *Sensors and Actuators B: Chemical*, 181, (2013), 130-135.

[3] B. Bouxin, K. Maier, A. Hackner, G. Mueller, F. Shao, J.D. Prades, F. Hernandez-Ramirez, J.R. Morante, On-chip fabrication of surface ionisation gas sensors, *Sensors and Actuators B: Chemical*, 182 (2013) 25-30.

[4] Copper Oxide Nanowires for p-type Conductometric Gas Sensing. (submitted)

[5] Direct assembly of ZnO nanowires onto micro hot plate membrane and its NH<sub>3</sub> sensing in isothermal and temperature- pulsed mode. (in preparation)

**Conference contribution:**

[1] F. Shao, F. Hernandez-Ramirez, J.D. Prades, J.R. Morante, N. Lopez, Assessment and Modeling of NH<sub>3</sub>-SnO<sub>2</sub> Interactions using Individual Nanowires, *Procedia Engineering*, 47 (2012) 293-297.

- [2] A. Shaposhnik, S. Ryabtsev, F. Shao, F. Hernandez-Ramirez, J. Morante, A. Zviagin, N. Meshkova, D. Shaposhnik, A. Vasiliev, Comparison of Hydrogen Sulfide Sensing Characteristics of Individual SnO<sub>2</sub> Nanowire and SnO<sub>2</sub> Sol-Gel Nanocomposite, *Procedia Engineering*, 47 (2012) 1398-1401.
- [3] Shao, F.; López, N.; Hernández-Ramírez, F.; Prades, J.D.; Fischer, T.; Mathur, S.; Morante, J.R, Simultaneous NH<sub>3</sub> and Humidity Sensing Using Individual SnO<sub>2</sub> Nanowires: Study and Quantification of the Interfering Effects”, MRS Fall Meeting, Boston 2012. (poster)
- [4] F. Shao, F. Hernández-Ramírez, J.D.Prades, J.R.Morante, Fabrication and characterization of ammonia sensors based on individual metal oxide nanowires. Euromat 2011, Montpellier, France. (oral)
- [5] F. Shao, N. Lopez, F. Hernández-Ramírez, J.D.Prades, J.R.Morante, Theoretical Modeling of NH<sub>3</sub> adsorption on SnO<sub>2</sub>. 36th International Conference and Expo on Advanced Ceramics and Composites 2012. Daytona, USA. (poster)
- [6] F. Shao, M.W.G. Hoffmann, J.D. Prades, R. Zamani, J. Arbiol, J.R. Morante, E. Varechkina, M. Rummyantseva, A. Gaskov, I. Giebelhaus, T. Fischer, S. Mathur, F. Hernández-Ramírez, Heterostructured p-CuO (Nanoparticle) / n-SnO<sub>2</sub> (Nanowire) Devices for Selective H<sub>2</sub>S detection. MRS 2013 spring. (poster)
- [7] B. Bouxin, K. Maier, A. Hackner, G. Mueller, F. Shao, F. Hernandez-Ramirez, and J.R. Morante, Highly efficient surface ionization gas detectors using microfabricated platforms with integrated surface electrodes. Eurosensor 2013, Barcelona, Spain. (poster)